O. Y. Usikov Institute for RadioPhysics and Electronics
National Academy of Sciences of Ukraine

Qualifying research work
in the form of manuscript

DARIIA O. HERASYMOVA

UDC 537.86: 535.417.2

DISSERTATION

DIFFRACTION RADIATION FROM DIELECTRIC, SILVER AND GRAPHENE CIRCULAR NANOWIRE CONFIGURATIONS EXCITED BY MODULATED ELECTRON BEAM

104 – Physics and Astronomy
10 - Natural Sciences

submitted in partial fulfillment of the requirements
for the Doctor of Philosophy degree

The dissertation contains the results of original research of the author. The use of ideas, results and texts of other authors is accompanied with corresponding references.

_____ D.O. Herasymova

Supervisors: S. V. Dukhopelnykov, Candidate of Technical Sciences, Senior Researcher and M. T. Cherpak, Doctor of Physical and Mathematical Sciences, Professor

Kharkiv– 2023

ABSTRACT

Herasymova D.O. **Diffraction radiation from dielectric, silver and graphene circular nanowire configurations excited by modulated electron beam**. - Qualifying research work in the form of manuscript.

This thesis is submitted in fulfillment of requirements for obtaining the degree of Doctor of Philosophy in specialization #104 – Physics and Astronomy (10 - Natural Sciences). - O. Y. Usikov Institute for RadioPhysics and Electronics NAS of Ukraine, Kharkiv, 2023.

The thesis is devoted to the theoretical analysis of diffraction radiation (DR) from a time-harmonically modulated beam of charged particles passing near to single and multiple circular, in cross-section, nanowires, made of dielectrics, noble metals, and graphene-covered dielectric wires. We consider several promising configurations of such scatterers. Here, analysis of DR from single wires is important for understanding the physics of the associated phenomena. This analysis is relatively simple as it needs only the separation of variables and leads to explicit solutions. However, it has not been performed so far and hence had to be done. Further, we consider DR from the dimers of dielectric, metal and graphene-covered circular nanowires, i.e. the pairs of twin (identical) nanowires, which we view as beam position monitors. Finally, we consider the DR in the presence of finite-periodic gratings of such nanowires, as a model of the orotron vacuum tube or the dielectric laser accelerator. As usual in the analysis of the DR, we assume that the beam velocity is fixed and obtain, in each case, a classical time-harmonic scattering problem for the known incident wave, which is the modulated-beam field in the free space. This is a full-wave two-dimensional (2-D) boundary-value problem for the Helmholtz differential equation in partial derivatives, with exact boundary conditions, plus the condition of local power finiteness and the radiation condition at infinity. In the case of noble-metal wires, we use the well-established experimental data for the frequently – dependent dielectric permittivity of silver in the

visible and infrared ranges. In the case of graphene-covered wires, we use the Kubo formalism for the electron conductivity of graphene and the resistive-sheet boundary conditions on the wire contours. To cast each of the considered problems to a well-conditioned algebraic (i.e. matrix) equation, we use the separation of variables in local coordinates and the addition theorems for cylindrical functions. This allows us to invert analytically the single-wire part of the whole DR problem and to bring it to a Fredholm second-kind matrix equation of the block type. The latter equation can be solved numerically with controlled accuracy up to machine precision. Using such a trusted numerical instrument, we perform systematic computations of the radiation power, the absorption power, as function of the frequency. These quantities display the resonance behavior caused by the excitation of the natural modes of the considered wires and their arrays as open resonators. The modes are identified by visualizing the near and far field patterns. To obtain better understanding of the natural modes, we perform the analysis of associated eigenvalue problems. Additionally, we consider the lasing eigenvalue problem for the graphene-covered wire dimer where we assume that the inner material is active, i.e. has gain, and determine the threshold conditions for the natural modes of such a plasmonic nanolaser.

The goal of the work is to analyze the resonance effects in DR from the mentioned above nanowire configurations excited by the harmonically modulated beams of charged particles. In terms of applications, we study the dimer structures that are most sensitive to variations in the beam trajectory and velocity and hence can be exploited as beam monitors. Finite arrays of nanowires are analyzed as key components of vacuum tubes and dielectric laser accelerators. In all cases, the resonance effects in DR due to excitation of various natural modes play crucial role. Therefore, we focus our analysis at a detailed study of how the resonances on the modes of dielectric wires, plasmon modes of metal and graphene tubes, and lattice modes of periodic arrays manifest themselves in the total scattering and absorption cross-sections and the far and near field patterns.

To achieve these goals, the following **tasks are solved**:

- building adequate 2-D mathematical models of the scattering and absorption of the harmonically modulated beam field by arbitrary ensemble of circular nanowires or nanotubes,
- developing corresponding numerical algorithms for computation of the scattering and absorption characteristics, as well as the fields in the near and far zones of the studied structures,
- mastering the use of the commercial numerical codes, necessary to confirm the theoretical results.
- establishing a general relationship between the DR scattering and absorption characteristics that is the Optical Theorem, adapted to the DR of the modulated electron beam,
- investigating how the resonances on the natural modes of dielectric wires, plasmon modes of metal and graphene boundaries, and lattice modes of finite arrays influence DR of a modulated electron beam,
- exploring the potentialities of beam position monitors, built on dimers of resonance nanowires of different nature: high refractive-index dielectric wires, metal wires, metal nanotubes and graphene-covered dielectric wires,
- investigating the natural modes of the dimer nanowire configurations viewed as open resonators and determining the lasing threshold conditions for these modes in the case of the presence of active regions.

The following **new scientific results** (i.e. those not published earlier, to our best knowledge) have been obtained in the work:

- if the particle beam trajectory is shifted from the central (symmetric) position between the twin nanowires, then the DR scattering and absorption spectra display appearance of previously absent resonances, associated with the dimer supermodes whose fields are orthogonal, in symmetry, to the beam field; the intensities of new peaks are proportional of the beam displacement or its angular shift,
- the above-mentioned effect has been found for the high-Q supermodes of the dimers of high refractive-index dielectric wires, thin noble-metal nanotubes, and

graphene-covered wires at the high enough values of graphene's chemical potential,

- to observe the mentioned effect, the frequencies of the modes of different azimuthal orders in single circular resonator, used in the dimer, have to be well separated from each other; therefore, it is not observed for the plasmon modes of the dimers of solid circular noble-metal nanowires,
- in the analysis of DR from sparse finite periodic arrays of many graphene-covered nanowires, the dominant feature in the frequency spectra of DR powers are the resonances on the plasmon modes of each wire and the lattice modes of the whole array.; the latter resonance peak intensities strongly depend on the number of wires,
- The Optical Theorem (OT), known previously in the plane-wave scattering, has been adapted to the DR effect; This entails introduction of the complex-valued angles of incidence; the derived expression can be used for partial validation of numerical codes (in the thesis, OT is satisfied with machine precision),
- in the analysis of the lasing threshold conditions of the modes of single circular graphene-covered active wire, we have found that if the wire radius is larger than 10 μm, then the "parasitic" dielectric wire modes become competitive with the "working" plasmon modes both in the frequencies and in the threshold values of the gain in active region,
- if the separation between the wires in graphene-covered active circular nanowire dimer becomes larger than their radius, then all four plasmon supermodes of the lowest types come together in close quartets both in frequencies and thresholds; one of the supermodes can have a lower threshold than the similar mode of the stand-alone nanowire.

Keywords: nanowire, dielectric, graphene, nanolaser, electron beam, beam position monitor, resonance, plasmon mode, grating mode, grating mode, self-excitation threshold, active zone.

АНОТАЦІЯ

Герасимова Д. О. **Дифракційне випромінення на структурах з круглих діелектричних, металевих і графенових нанониток, що збуджуються модульованим потоком електронів**. – Кваліфікаційна наукова праця на правах рукопису.

Дисертація на здобуття наукового ступеня доктора філософії за спеціальністю 104 – Фізика та астрономія (10 – Природничі науки). - Інститут радіофізики та електроніки ім. О.Я. Усикова НАН України, Харків, 2023.

Дисертацію присвячено теоретичному аналізу дифракційного випромінення (ДВ) гармонічно модульованого в часі пучка заряджених частинок, що пролітає поблизу одиничних круглих у поперечному перерізі нанониток, виготовлених з діелектриків, благородних металів і вкритих графеном, а також структур з їхнього скінченного числа. Розглядаються кілька перспективних конфігурацій таких розсіювачів. Аналіз ДВ від окремих ниток важливий для розуміння фізики пов’язаних явищ. Цей аналіз відносно простий, оскільки потребує лише застосування методу розділення змінних і веде до явних рішень. Однак такий аналіз ще ніким не був виконаний, тому є необхідність це зробити. Далі розглянуто ДВ від даймерів з діелектрика, металу та вкритих графеном, тобто від пар однакових нанониток, які ми розглядаємо як моделі моніторів положення пучка. Нарешті, ми розглядаємо ДВ у присутності скінченно-періодичної решітки таких нанониток, яка може розглядатися як модель електронно-вакуумного джерела типу оротрона або діелектричного лазерного прискорювача. Як зазвичай при аналізі ДВ, ми вважаємо, що швидкість пучка є фіксованою, і в кожному випадку отримуємо класичну задачу гармонійного у часі розсіяння для заданої падаючої хвилі, яка є полем модульованого пучка у вільному просторі. Це двовимірна (2-D) крайова задача у строгій постановці для диференціального

рівняння Гельмгольца в частинних похідних із відповідними крайовими умовами, а також умовою локальної скінченності потужності та умовою випромінення на нескінченності. У випадку ниток із благородних металів ми використовуємо широко відомі експериментальні дані для частотно-залежної діелектричної проникності срібла у видимому та інфрачервоному діапазонах. У випадку ниток, покритих графеном, ми використовуємо формалізм Кубо для електронної провідності графену та граничні умови резистивного типу на контурах нанониток. Щоб привести кожну з розглянутих задач до добре обумовленого алгебраїчного (тобто матричного) рівняння, ми використовуємо розділення змінних у локальних координатах і теореми додавання для циліндричних функцій. Це дозволяє нам аналітично обернути таку частину всієї задачі ДВ, яка відповідає одній нанонитці, і привести її до матричного рівняння другого роду Фредгольма блочного типу. Останнє рівняння можна розв’язати чисельно з контрольованою точністю, яку може бути доведено до машинної точності. Використовуючи такий надійний чисельний інструмент, ми виконуємо систематичні обчислення потужності випромінення та потужності поглинання, як функцій частоти. Ці величини демонструють резонансну поведінку, спричинену збудженням власних мод розглянутих ниток та їхніх масивів як відкритих резонаторів. Моди ідентифікуються шляхом візуалізації ближнього та дальнього поля. Щоб краще зрозуміти властивості власних мод, ми виконуємо аналіз відповідних задач на власні значення. Крім того, ми окремо розглядаємо лазерну задачу на власні значення для одиничної нитки та даймеру, покритих графеном, де ми припускаємо, що внутрішній матеріал є активним, тобто має підсилення, і визначаємо порогові умови для власних мод такого плазмонного нанолазера.

Метою дисертаційної роботи є аналіз резонансних ефектів у ДВ у присутності конфігурацій з нанониток, що згадані вище, які збуджуються гармонічно модульованими пучками заряджених частинок. З точки зору застосувань, ми вивчаємо даймери з нанониток – це такі конфігурації, які є найбільш чутливими до змін траєкторії та швидкості пучка, і, отже, можуть

використовуватися як монітори положення пучка. Скінченні решітки з нанониток цікаві як ключові компоненти вакуумних джерел і діелектричних лазерних прискорювачів. У всіх випадках найбільш важливу роль відіграють резонансні ефекти в ДВ за рахунок збудження різних власних мод. Тому ми зосереджуємо наш аналіз на детальному вивченні того, як резонанси на модах діелектричних ниток, плазмонних модах металевих і графенових трубок, а також граткових модах періодичних решіток проявляються в повних перерізах розсіяння та поглинання, а також у далеких і ближніх полях.

Для досягнення поставлених цілей вирішуються такі **завдання**:

- побудова адекватних 2-D математичних моделей розсіяння та поглинання гармонічно модульованого поля пучка частинок довільним ансамблем кругових нанониток або нанотрубок;

- розробка відповідних чисельних алгоритмів для розрахунку характеристик розсіяння та поглинання, а також полів у ближній та дальній зонах;

- навчання застосуванню комерційних числових кодів, необхідних для підтвердження теоретичних результатів;

- встановлення загального зв'язку між характеристиками розсіяння та поглинання, який називається «оптичною теоремою», що адаптована до ДВ модульованого електронного пучка;

- дослідження того, як резонанси на власних модах діелектричних ниток, плазмонних модах металевих і графенових оболонок, а також граткових модах впливають на ДВ модульованого електронного пучка;

- вивчення можливостей моніторів положення пучка, побудованих на даймерах з резонансних нанониток різної природи: діелектричних ниток з високим показником заломлення, металевих ниток, металевих нанотрубок і діелектричних ниток, покритих графеном;

- дослідження власних мод даймерів з нанониток, які розглядаються як відкриті резонатори, та визначення порогових умов генерації цих мод у разі наявності активних областей.

У роботі отримано наступні **нові наукові результати**:

- якщо траєкторія пучка частинок зміщується з центрального (симетричного) положення між двома нанонитками даймеру, то в спектрах розсіяння та поглинання ДВ з'являються раніше відсутні резонанси, пов'язані з супермодами даймеру, поля яких ортогональні, в сенсі симетрії, до поля пучка; інтенсивності нових резонансних піків пропорційні зсуву пучка;

- вищевказаний ефект виявлено для високодобротних супермод даймерів з діелектричних ниток з великим показником заломлення, тонких нанотрубок з благородних металів і ниток з графеновим покриттям при досить високих значеннях хімічного потенціалу графену;

- для спостереження зазначеного ефекту, частоти мод різних азимутальних порядків в одному круговому резонаторі, використаних у даймері, повинні бути добре віддалені одна від одної; отже, це не спостерігається для плазмонних мод даймерів з суцільних круглих нанониток з благородних металів;

- при аналізі ДВ від скінченних решіток (періодичних структур) з багатьох нанониток, вкритих графеном, у частотних спектрах потужності ДВ домінують резонанси на плазмонних модах кожної нитки та на граткових модах всієї решітки; інтенсивність граткових резонансів суттєво залежить від кількості ниток;

- «оптичну теорему», відому з теорії розсіяння плоских хвиль, адаптовано до ефекту ДВ; це вимагає введення до розглядання комплексних кутів падіння для поля пучка електронів; вираз, що отримано, можна застосувати для часткової верифікації чисельних результатів, (у дисертації цей вираз задовольняється з машинною точністю);

- виявлено, що якщо радіус одиничної кругової активної нитки, покритої графеном, є меншим за 10 μм, то «робочі» плазмонні моди графенової оболонки мають значно нижчі частоти і порогові значення посилення в активній області, ніж «паразитні» діелектричні моди нитки; у більш товстих нитках всі вказані моди стають конкурентоспроможними;

- якщо відстань між нитками у даймері з двох покритих графеном активних

нанониток стає більшою за їхній радіус, тоді всі чотири плазмонних супермоди кожного типу утворюють тісні квартети з близькими частотами і порогами; одна з супермод може мати поріг, нижчий за поріг подібної моди для одиничної нанонитки.

Ключові слова: нанонитка, діелектрик, графен, нанолазер, пучок електронів, монітор положення пучка, резонанс, плазмонна мода, граткова мода, поріг самозбудження, активна зона.

LIST OF PUBLICATIONS RELATED TO THE THESIS

Papers in international journals

1. D. O. Herasymova, D.M. Natarov, S.V. Dukhopelnykov, T.L. Zinenko, M. Lucido, and A.I. Nosich, "Threshold conditions for transversal modes of tunable plasmonic nanolasers shaped as single and twin graphene-covered circular quantum wires," IOP Nanomaterials, vol. 33, no. 49, art. no 495001, 2022. **(Q-2)**
2. D. O. Herasymova, S. V. Dukhopelnykov and A. I. Nosich, “Infrared diffraction radiation from twin circular dielectric rods covered with graphene: plasmon resonances and beam position sensing,” Journal of the Optical Society of America B, vol. 38, no. 9, pp 183-190, 2021. **(Q-2)**
3. D. O. Herasymova, S. V. Dukhopelnykov, M. Lucido and A. I. Nosich, “Optical sensing of electron-beam position with twin silver nanotube antenna tuned to hybrid surface plasmon resonance,” IEEE Journal of Selected Topics in Quantum Electronics, vol. 27, no 1, art. no 3024114, 2020. **(Q-1)**
4. D. O. Yevtushenko and S. V. Dukhopelnykov, "Visible light from modulated electron beam moving between twin circular silver nanowires forming plasmonic photonic molecule," IOP Journal of Optics, vol. 22, no 2, art. no 025002, 2020. **(Q-1)**
5. D. O. Yevtushenko, S. V. Dukhopelnykov, and A. I. Nosich, “Electron-beam excitation of supermodes of a photonic molecule built on twin high refractive index dielectric nanowires,” J Journal of Applied Physics, vol. 125, no 22, art. no 223102, 2019. **(Q-2)**
6. D. O. Yevtushenko, S. V. Dukhopelnykov, and A. I. Nosich, "Optical diffraction radiation from a dielectric and a silver nanowire excited by a modulated electron beam," Optical and Quantum Electronics, vol. 51, no 1, art. no 29, 2019. **(Q-2)**

Papers in proceedings of international conferences, indexed in Scopus

7. D. O. Herasymova, "Diffraction radiation analysis of finite graphene-covered nanowire grating excited by electron beam," Proc. European Microwave Conference (EuMC-2023), Berlin, 2023, pp. 544-547.
8. D. O. Herasymova, "Near and far field characteristics of two in line graphene coated dielectric nanowires excited by modulated electron beam," Proc. 2023 IEEE/MTT-S International Microwave Symposium (IMS 2023), San Diego, 2023, pp. 482-485.
9. D. O. Herasymova, "Infrared diffraction radiation from two in-line dielectric rods covered with graphene," Proc. European Conference on Antennas and Propagation (EuCAP-2023), Florence, 2023, pp. 1-4.
10. D. O. Herasymova and S.V. Dukhopelnykov, "Lasing threshold conditions for transversal modes of twin graphene-covered circular quantum wires," Proc. European Microwave Conference (EuMC-2022), Milan, 2022, pp. 242-245.
11. D. O. Herasymova, " Infrared diffraction radiation from twin dielectric rods with graphene coatings as a tool for beam position sensing," Proc. Int. Conference on Electronics and Nanotechnologies (ELNANO-2022), Kyiv, 2022, pp. 164-67.
12. D. O. Herasymova, " Electromagnetic analysis of lasing eigenmodes of twin semiconductor nanorods with graphene covers," Proc. European Conference on Antennas and Propagation (EuCAP-2022), Madrid, 2022, art. no 1570770733.
13. D. O. Herasymova, "Sensing the charged-particle beam position using the terahertz range diffraction radiation from two dielectric rods covered with graphene," Proc. European Microwave Conference (EuMC-2021), London, 2021, pp. 249-253.
14. D.O. Herasymova, S.V. Dukhopelnykov, T.L. Zinenko, "Electromagnetic eigenvalue problem for twin dielectric rods covered with graphene: symmetry classes of the H-polarized supermodes," Proc. IEEE Ukraine Conference on Electrical and Computer Engineering (UKRCON-2021), Lviv, 2021, pp. 771-774.
15. D. O. Herasymova, "Evaluation of twin silver nanotubes as a possible sensor of

the charged particle beam position," Proc. European Microwave Conference (EuMC-2020), Utrecht, 2020, pp. 615-618.

16. D. O. Herasymova, "Near fields of twin circular silver nanotubes exited by electron beam moving between them", Proc. IEEE Ukrainian Microwave Week (UkrMW-2020), IEEE 6th Microwaves, Radar and Remote Sensing Symposium (MRRS), Kharkiv, 2020, pp. 937-941.

17. D. O. Herasymova and S. V. Dukhopelnykov, "Full-wave modeling of beam position monitors on silver nanowires and nanotubes: analysis of solution convergence," Proc. Int. Conference on Electronics and Nanotechnologies (ELNANO-2020), Kyiv, 2020, pp. 77-80.

18. D. O. Herasymova, "Electromagnetic design of beam position monitor based on diffraction radiation from twin dielectric nanowires," Proc. European Conference on Antennas and Propagation (EuCAP-2020), Copenhagen, 2020, art. no 9135642.

19. D. O. Yevtushenko, "Bright and dark supermodes of twin dielectric nanowire photonic molecule excited by a modulated electron beam," Proc. Int. Conference on Microwaves, Communications, Antennas, and Electronic Systems (COMCAS-2019), Tel Aviv, 2019, art. no 8958106.

20. D. O. Yevtushenko, "Optical range diffraction radiation of electron beam in the presence of twin circular dielectric nanowires," Proc. European Microwave Conference (EuMC-2019), Paris, 2019, pp. 97-100.

21. D. O. Yevtushenko, "Optical resonances of photonic molecule of twin high refractive index dielectric nanowires excited by modulated electron beam," Proc. IEEE Ukraine Conf. Electrical Computer Eng. (UKRCON-2019), Lviv, 2019, pp. 771-774.

22. D. O. Yevtushenko and S. V. Dukhopelnykov, "Total scattering cross-section of twin circular silver nanowires excited by electron beam moving between them," Proc. European Microwave Conference in Central Europe (EuMCE-2019), Prague, 2019, pp. 386-389.

23. D. O. Yevtushenko and S. V. Dukhopelnykov, "Near fields of twin circular silver nanowires excited by electron beam moving between them," Proc. Int. Conference on

Electronics and Nanotechnologies (ELNANO-2019), Kyiv, 2019, pp. 340-343.

24. D. O. Yevtushenko, "Optical diffraction radiation of a beam of particles flowing near a circular silver nanowire," Proc. Int. Seminar/Workshop on Direct and Inverse Problems of Electromagnetic and Acoustic Wave Theory (DIPED-2018), Tbilisi, 2018, pp. 43-46.

25. D. O. Yevtushenko, S. V. Dukhopelnykov, E. N. Odarenko, and A. I. Nosich, “Diffraction radiation of electron beam in the presence of dielectric optical nanowire resonator,” Proc. Int. Conference on Mathematical Methods in Electromagnetic Theory (MMET-2018), Kyiv, 2018, pp. 148-151.

Note: Dariia’s maiden name is Dariia Yevtushenko, therefore, in the articles published in 2018-2020, she is marked as D. O. Yevtushenko.

CONTENTS

LIST OF NOTATIONS

ACS – Absorption Cross Section

BPM – Beam Position Monitor

CS – Coordinate System

DDA – Discrete Dipole Approximation

DLA – Dielectric Laser Accelerator

DR – Diffraction Radiation

EM – Electromagnetic

ECS – Extinction Cross Section

FDTD – Finite-Difference Time-Domain

IE – Integral Equation

LEP – Lasing Eigenvalue Problem

LSP – Localized Surface Plasmon

OT – Optical Theorem

PEC – Perfect Electrically Conducting

PM – Photonic Molecule

PMC – Perfect Magnetically Conducting

QW – Quantum Wire

RA – Rayleigh Anomalies

SPE – Smith-Purcell Effect

SCS – Scattering Cross Section

TACS – Total Absorption Cross Section

TSCS – Total Scattering Cross Section

WG – Whispering Gallery

INTRODUCTION

Justification of the choice of research topic. As known, charged particles, such as electrons, radiate electromagnetic waves when moving through the boundary between material media or inside such a medium – this is called the transition or the Cherenkov radiation, respectively. The radiation of electrons moving in vacuum without crossing any material boundaries has also attracted the attention of researchers since 1950s. The most known example of such effect is the Smith-Purcell radiation [1-13]; it is associated with an electron beam flowing over a periodic grating, for instance, ruled on a metal surface, across the grooves. Still the *Smith-Purcell effect* (SPE) is only a particular case of more general phenomenon: the radiation of the surface and polarization currents induced on the metal and dielectric objects by the electron beams flowing in their vicinity however without touching them. This type of electromagnetic-wave radiation is commonly called the *diffraction radiation* (DR) [5-14].

Microwave-range DR is already used as a convenient method for non-invasive diagnostics of beams in accelerators, i.e. for remote sensing of the position and velocity of the particle beams [10-14]. Such devices are commonly referred to as *beam position monitors* (BPM). Today, the development of BPM can be extended to the optical range, because the emergence and rapid development of nanotechnology opens the way to create ensembles of nanosized optical scatterers with controlled shape and location [15-18]. Nanoscale components introduce very little perturbation to the beam, its velocity and trajectory, and therefore its field can be considered fixed. Therefore, the analysis of the DR effect can be performed within the classical theory of *electromagnetic* (EM) wave scattering, i.e. as the scattering of the given wave by the objects of known shape and material parameters.

Measuring the DR intensity in the near or far zone, one can monitor the electron-beam parameters [13, 14]. As BPM is a specific sensor, optimisation of its performance requires finding a favourable combination of its element shapes and materials. Here, the use the resonance effects is a promising approach. A resonance enhances the DR

intensity proportionally to the squared Q-factor of the resonating mode. In the microwave range, various coaxial metallic hollow cavities integrated with the drift tubes are common. This approach can be extended to the THz and IR ranges if suitable resonators shaped as sub-wavelength scatterers are found. One possible approach is the use of high-refractive-index materials; however, available today dielectric materials have refractive indices within several dozens, so that the resonances on their lowest modes entail only moderately sub-wavelength dimensions. The other approach uses the noble-metal scatterers, able to support the surface plasmon modes in the visible range [19, 20]; however, these modes have rather low Q-factors, due to high losses in noble metals. The way out can be seen in the exploitation of the plasmon modes on the patterned graphene or graphene-coated scatterers [21, 22]. Note that such configurations are already studied as the elements of promising IR and THz range sensors of the host-medium refractive index and tuneable filters, absorbers, scatterers and antennas [23-27]. The dielectric and silver scatterers were studied, in particular, in the many works.

Graphene is new material that consists of a monolayer or a few such layers of graphite, i.e. has sub-nanometre thickness. It has remarkable properties like transparency in the visible range, mechanic strength, and good electron conductivity in the THz and infrared (IR) ranges. The conductivity is a function of the temperature, electron relaxation time, frequency and chemical doping. Graphene can support the plasmon guided wave at the THz and IR frequencies that makes its electromagnetic properties similar to noble metal ones in the visible-light range, however, at much lower frequencies. What is principally new, graphene conductivity and hence plasmon effect can be tuned using the DC bias, which translates to the chemical potential [21,22]. Usually graphene is attached to flat dielectric substrates, however, now curved substrates attract an increasing attention [23,24]. Recently, graphene-covered nanowire fabrication and synchrotron nanospectroscopy measurements have been reported [25]. Note that circular-wire dimers coated with graphene have been studied with commercial codes in the context of field forces [26] and cloaking [27], and with in-house code based on the local Fourier expansions in the analysis of eigenfrequencies. However, all these

works considered the plane wave as the incident field.

Thus, the task of studying the DR effect in the visible, IR and THz ranges for nanoscale structures of circular wires of dielectric, metal and graphene materials is timely.

The object of research is the phenomena of the scattering and absorption of the modulated electron beam field by configurations of finite-number circular nanowires and nanotubes, as well as the eigenvalue problems for such circular open resonators with graphene cover.

The subject of the study is the resonance and spectral characteristics of the EM field scattering and absorption by finite configurations of circular nanowires and nanotubes, excited by the modulated beams of charged particles, as well as the eigenmodes of such nanowire configurations.

Research goals and tasks. The goal of this work is to analyze the DR effect for various structures of circular nanowires and nanotubes made of dielectric, metal, and graphene. Here, keeping in mind BPM applications, we look for the structures that are the most sensitive to variations in the trajectory of the beam and to the changes in its velocity. Since the sensitivity of BPM usually improves due to resonances, our analysis includes a detailed study of how the resonances on the modes of circular dielectric wires, plasmon modes of noble-metal and graphene wires and tubes, and lattice modes of finite arrays of wires manifest themselves in DR of modulated electron beam.

To achieve these goals, the following **tasks are set**:

• build a 2-D mathematical model for the scattering of the field of a beam of particles from arbitrary ensemble composed of a finite number of dielectric or silver wires or tubes of circular cross section;

• develop a numerical algorithm for calculating the characteristics of the DR-caused scattering and absorption, as well as fields in the near and far zones of the studied structures;

• investigate how the resonances on the modes of dielectric wires, plasmon modes of metal and graphene wires, and lattice modes of the grating made of graphene-covered

wires influence the DR of a modulated electron beam;

• establish a relationship between the DR-caused scattering and absorption characteristics and the far-field angular DR that accounts for the configuration of the scatterers and for the beam trajectory position (modified Optical theorem);

• develop recommendations for an optimal design of the optical BPM;

• calculate the DR problems with commercial codes to validate the theoretical results.

These tasks are accomplished in 5 chapters of the work.

The first chapter discusses (i) the main methods of analysis of wave scattering by circular dielectric cylinder configurations, (ii) representation of the incident field as the harmonically modulated charged particles beam field, (iii) complex permittivity of silver as a function of the frequency, (iv) description of the graphene conductivity via the Kubo formalism, (v) scattering and absorption characteristics and beam field adapted Optical Theorem, and (vi) Lasing Eigenvalue Problem statement. Here, the method review includes the Discrete Dipole Approximation method, Finite-Difference Time-Domain method, method of separation of variables and Method of Analytical Regularization.

The second chapter is dedicated to the statement of the scattering problem for a finite number of circular wires excited by the electron beam and numerical investigation of the DR-caused scattering and absorption characteristics in the visible range for a single dielectric nanowire and dimer of twin dielectric nanowires.

The third chapter includes analysis of the DR-caused scattering and absorption characteristics for a stand-alone circular silver nanowire and twin circular silver nanowires and nanotubes in the visible range.

In the fourth chapter, the DR-caused scattering and absorption characteristics in the THz range are numerically investigated for a stand-alone circular dielectric nanowire covered with graphene, twin graphene-coated nanowires configuration and finite array of circular graphene-covered dielectric nanowires.

The fifth chapter presents the implementation of the Lasing Eigenvalue Problem

(LEP) approach for study of the EM field in the presence of a single circular *quantum wire* (QW) made of a gain material and wrapped in graphene cover and a dimer of two identical graphene-covered QWs, at the threshold of stationary emission.

Research methods. The research methods include the theory of 2-D boundary-value problems of classical electromagnetics which consists of the following: the Helmholtz equation with corresponding wavenumber in each partial domain, the boundary conditions at the wire cross-sectional contours, the Sommerfeld radiation condition at infinity, and the condition of local power finiteness. These conditions guarantee the uniqueness of the boundary-value problem solution. As for the graphene covers, they are assumed to be zero-thickness conducting tubes. Here, the Kubo formalism is applied to characterize graphene's complex-valued surface impedance and the resistive-type boundary conditions are requested on the graphene. Further, we use the circular shape of the nanowires and apply the field expansions in the Fourier series in local polar coordinates of each wire, combined with the Graf addition theorem for the cylindrical functions. On substitution into the boundary conditions, this leads to the Fredholm second kind matrix equations for the field expansion coefficients. Therefore, such a technique belongs to the family of the *methods of analytical regularization* (MAR). The Fredholm nature guarantees that the solutions of the truncated matrix equations converge to the exact solutions if the truncation number gets larger. It is expected that such a code will outperform, in speed, the existing commercial codes in hundreds of times and enable easy control of the accuracy of computations. We carry out computations of DR-caused scattering and absorption characteristics, as well as near and far field patterns, especially at the resonance frequencies.

Scientific novelty of obtained results. The following new results have been personally obtained by the author:

- if the particle beam trajectory is shifted from the central (symmetric) position between the twin nanowires, then the DR scattering and absorption spectra display appearance of previously absent resonances, associated with the dimer supermodes whose fields are orthogonal, in symmetry, to the beam field; the intensities

of new peaks are proportional of the beam displacement or its angular shift,

- the above-mentioned effect has been found for the high-Q supermodes of the dimers of high refractive-index dielectric wires, thin noble-metal nanotubes, and graphene-covered wires at the high enough values of graphene's chemical potential,
- to observe the mentioned effect, the frequencies of the modes of different azimuthal orders in single circular resonator, used in the dimer, have to be well separated from each other; therefore, it is not observed for the plasmon modes of the dimers of solid circular noble-metal nanowires,
- in the analysis of DR from sparse finite periodic arrays of many graphene-covered nanowires, the dominant feature in the frequency spectra of DR power are the resonances on the plasmon modes of each wire and the lattice modes of the whole array; the latter resonance peak intensities strongly depend on the number of wires,
- the Optical Theorem (OT), known previously in the plane-wave scattering, has been adapted to the DR effect: that entails introduction of the complex-valued angles of incidence; the derived expression can be used for partial validation of numerical codes (in the thesis, OT is satisfied with machine precision)
- in the analysis of the lasing threshold conditions of the modes of single circular graphene-covered active wire, we have found that if the wire radius is larger than 10 μm, then the "parasitic" dielectric wire modes become competitive with the "working" plasmon modes both in the frequencies and in the threshold values of the gain; otherwise, the plasmon mode frequencies and thresholds are much lower.
- if separation between the wires in graphene-covered active circular nanowire dimer becomes larger than their radius, then all four plasmon supermodes of the lowest types form tight quartets; one of the supermodes can have a lower threshold than the similar mode of the stand-alone nanowire

Practical value of obtained results. The proposed method and the developed numerical algorithms have controlled accuracy and can be applied for the trusted and time-efficient computation of the DR-caused scattering and absorption by nanowire configurations made of dielectric, noble-metal and graphene, using the moderate

computer hardware.

The obtained results of numerical analysis of the DR-caused scattering and absorption characteristics versus the frequency and other parameters, the far and near field patterns of the wave emission from charged particle beam moving near various nanowire scatterers and gratings of them have fundamental significance. They have also a wide range of applications including the BPM and DLA designs. The analysis of thresholds conditions for the plasmon modes of the considered in the thesis nanolasers can help in the creation of new, more efficient sources of waves.

The developed computational codes of the main scattering and absorption characteristics permit using them as a core of the software for numerical optimization of optical configurations, key elements of which are circular nanowires.

Personal contribution of the author. The main results presented in the dissertation were obtained by the author. The contribution to the co-authored works in [A1-A25] consists in the derivation of the basic equations, the development of numerical algorithms, the writing of the corresponding codes, as well as in the systematic calculation of the DR scattering and absorption characteristics, the DR patterns in the near and far zones, and in the interpretation of the obtained results. All conference papers were presented by the author personally.

Dissemination of results. The results of the work were presented and discussed at the following scientific seminars: IRE NASU (Prof. P. M. Melezhyk), Institut d'Électronique et des technologies du numérique IETR, Universite de Rennes 1, France (Prof. R. Sauleau), Institute of Experimental Physics, University of Wroclaw, Poland (Prof. A. Szczepkowicz), and The Institute of Spintronics and Quantum Information (ISQI), Adam Mickiewicz University in Poznan, Poland (Prof. J. Klos). Besides, they were presented at the following international conferences, workshops and symposia:

- IEEE Conference on Mathematical Methods in Electromagnetic Theory (MMET), Kyiv (2018);
- IEEE International Workshop on Direct and Inverse Problems of Electromagnetic and Acoustic Wave Theory (DIPED), Tbilisi (2018);

- IEEE International Conferences on Electronics and Nanotechnologies (ELNANO), Kyiv (2019, 2020, 2022);
- European Microwave Conference in Central Europe (EuMCE), Prague (2019);
- IEEE Ukraine Conferences on Electrical and Computer Engineering (UKRCON), Lviv (2019, 2021);
- European Microwave Conferences (EuMC), Paris (2019), Utrecht (2020), London (2021), Milan (2022), Berlin (2023);
- IEEE International Conference on Microwaves, Communications, Antennas, and Electronic Systems (COMCAS), Tel Aviv (2019);
- European Conferences on Antennas and Propagation (EuCAP), Copenhagen (2020), Madrid (2022), Florence (2023);
- IEEE Ukrainian Microwave Week (UkrMW): IEEE Microwave, Radar and Remote Sensing Symposium (MRRS), Kharkiv (2020);
- IEEE/MTT-S International Microwave Symposium (IMS), San Diego (2023).

Publications. The results of research have been published in 25 refereed papers indexed in Scopus, including 6 papers in international journals [A1-6] and 19 papers in the proceedings of international conferences [A6-25].

Relation to scientific programs, projects and grants. The research within this thesis has been performed in the Laboratory of Micro and Nano Optics of the Quasioptics Department of IRE NASU, in the framework of the following projects:

1. Research project of NASU "Development and application of methods of optics and quasioptics for generation and transforming the electromagnetic waves of terahertz, infrared and visible ranges", code "Oreol-1", # 0117U004036 (2019-2022)
2. Research project of NASU "The research of interaction processes of electromagnetic radiation in terahertz, infrared and visible ranges with various natural or artificial materials, mediums and structures", code "Oreol-2", # 0122U001710 (2022-

2026)

3. Competitive project of NASU, "Radiophysical phenomena in nanoelectronic systems based on graphene, unconventional superconductors and magnetized semiconductors ", code "Nanograph", # 0122U200724 (2022)

4. Competitive project of the National Research Foundation of Ukraine (NRFU) "Electromagnetic modeling of micro and nano lasers", code "Sonata", #2020-02-0150 (2020-2022)

5. Joint research project with Universite de Rennes 1 – Programme of the Ministry of Education and Science, Ukraine and the Ministry of Eurapean and Foreign Affairs, France, "Terahertz graphene-based metasurfaces and transmitarrays", code "Dnipro", #0119U102172 and #0120U104419 (2019-2021)

6. Competitive project of Programme d'aide à l'Accueil en Urgence des Scientifiques en Exil (PAUSE), Universite de Rennes 1, Rennes, France, "Diffraction radiation nanoantennas for electron beam position sensing and terahertz source development" (2023)

It has been also partially supported by the following scholarships of the international professional societies:

- Project "Smith-Purcell terahertz radiation from a beam of particles moving above a grating of graphene-covered dielectric rods", IEEE Microwave Theory and Techniques Society Fellowship, 2023
- Project "Diffraction radiation antennas based on graphene covered dielectric wires for electron beam position sensing and terahertz source development", IEEE Antennas and Propagation Society Fellowship, 2022
- Project "Electromagnetic analysis of lasing eigenmodes of twin semiconductor nanorods with graphene covers", European Association on Antennas and Propagation - TICRA Grant, 2022
- Project "Infrared range diffraction radiation from two dielectric rods covered with graphene as a tool for sensing the charged-particle beam position", IEEE Photonics Society Graduate Student Scholarship, 2021

- Project "Electromagnetic design of beam position monitor based on diffraction radiation from twin dielectric nanowires", European Association on Antennas and Propagation - TICRA Grant, 2020
- Project "Diffraction radiation of electron beams from optical nanoresonators: antenna effects and beam diagnostics", IEEE Antennas and Propagation Society Pre-Doctoral Research Award, 2018
- Project "Electromagnetic engineering of plasmon-assisted optical nanowire sensors for electron beam diagnostics", IEEE Microwave Theory and Techniques Society Pre-Graduate Scholarship, 2018

Structure and volume of thesis. The dissertation consists of an abstract, an introduction, 5 chapters, general conclusions, 1 appendix, and list of used sources with 159 titles. The volume of the total text of the dissertation is 175 pages, of which the main text is 155 pages. The work is illustrated with 73 figures.

CHAPTER 1 LITERATURE REVIEW AND RESEARCH METHODS

1.1 Methods of analysis of wave scattering from circular dielectric cylinders

Since the topic of the dissertation is the theoretical study of the phenomenon of the modulated electron-beam field scattering from the structures made of circular wires of various materials, in this section we present a short overview of the main methods of the full-wave modeling of the 2-D scattering from such objects.

The problem of time-harmonic EM wave scattering and absorption by circular dielectric cylinders can be analyzed using several methods. Here are a few existing methods commonly employed,

- *Discrete Dipole Approximation* (DDA): The DDA is a numerical technique commonly used to analyze the light scattering from particles. It represents the particle as a cluster of polarizable dipoles and solves the scattering problem by calculating the re-radiation of these dipoles at the given incident light. The DDA can be used to investigate the scattering and absorption properties of circular dielectric cylinders and provides information about the scattered field, extinction, and absorption cross-sections.

Originally, the DDA was proposed by Purcell and Pennypacker, who substituted the scatterer with a collection of point dipoles [28]. The interaction between these dipoles and the incident field results in a system of linear equations, which is solved to determine the dipole polarization amplitudes [29]. All the necessary scattering quantities can be derived from these polarization amplitudes. Later on, DDA was developed and popularized by Draine and others, including developing the free-to-public computer code DDSCAT [30-33]. Then, Goedecke and O'Brien showed another way of deriving the DDA: they discretized the volume electric field integral equation by means of dividing their scatterer into fractional cubical sub-volumes [34]. It is worth noting that the final equations resulting from both approaches to derive the DDA are essentially identical [28]. There are DDA equivalent methods developed by others researchers in the same time. They were called the volume integral equation formulation

and the digitized Green's function [34, 35]. Additionally, there are various *methods of moments* (MoM) which are similar to DDA, due to the fact that they are also based on the volume integral equations for the EM fields [36, 37]. In contrast, DDA was simply explained by Yurkin and Hoekstra as substituting any scatterer with a set of dipoles that interact with each other [28].

All DDA methods have different nature of errors. In a number of works, the origin of errors in the DDA was examined in the attempt to separate and compare shape and discretization errors [38-42]; however, no definite conclusions were reached. The uncertainty was due to the indirect (empirical) methods used that have inherent interpretation problems.

We would like to emphasize that DDA convergence, with larger number of the dipoles, cannot be established mathematically. In the case of volume integral equations, this relates to their singular nature. Overall, this method has gained popularity in the field of light scattering and has been extensively developed by multiple authors; there is a large amount of reviews on both the theory and numerical aspects [43-45].

- *Finite-Difference Time-Domain* (FDTD) Method: The FDTD method is a numerical technique used to solve Maxwell's equations and simulate the propagation of light through various structures, including dielectric cylinders. This technique has proven to be a universal and relatively simple computational method for solving the scattering of EM waves from wide class of scatterers, especially those with complex geometries and non-uniform compositions [46]. It discretizes the space and time domains and numerically solves the Maxwell differential equations by replacing the derivatives with finite differences. That provides valuable insights into the diffraction patterns, scattering efficiencies, and field patterns.

The method was initially introduced by K. Yee and subsequently enhanced by other researchers in the early 1970s [47]. The uniqueness of Yee's concept lies in the spatial allocation of electric and magnetic field components and the time-stepping approach for the procedure evolution. The method was not wildly recognized until the 1980s, when the absorbing boundary conditions of high quality were derived. Then

Taflove, Kunz, Holland and other engineers and scientists worked on FDTD and demonstrated a number of its advantages, which provided the popularity of FDTD [48-50]. By default, it is considered that FDTD accuracy is improved (i.e. its error is reduced) by a denser meshing. However, the spatial and temporal steps (cell sizes) in FDTD cannot be arbitrarily small. This is because denser meshing quickly leads to prohibitively large-size matrices and, hence, huge computation time.

Over the past years, the FDTD technique has found application in solving interactions between obstacles and EM waves in various problems, including antenna scattering, microstrip structures numerical modeling, and the study of EM absorption by human body tissues [51-55].

Still, FDTD needs placing a time-dependent (pulse) source at one point of computational domain and computing the time-dependent EM field at another point. Therefore, the results depend on the “goodness” of choice of these points.

Besides, FDTD simulations have limitations on the maximum allowable temporal step. If the step size is too large, the algorithm yields unstable results, rendering the obtained values meaningless and prone to rapidly approaching infinity. Additionally, FDTD algorithms often impose significant demands on computational resources, particularly when dealing with open-domain or resonant problems [56]. This limits technique integration with optimization routines. However, these requirements are considerably diminished when using 2-D versions of FDTD [57].

Further, FDTD codes suffer from another inherent drawback: in both 2-D and 3-D, the accuracy of the analysis can suffer near high-Q natural resonances [58,59]. This issue is crucial for dielectric scatterers, which we consider in this dissertation. If it is necessary to obtain not a time but a frequency dependence of the field, then the Fourier transform has to be used. This implies truncation of the integration domain, in time, at certain finite value. The choice of that value is important, however, it cannot be too large to make the computations limited by, at least, minutes and small hours. This makes correct computing of resonances with $Q > 10^5$ extremely time-consuming. Recently, the numerical results comparison verified the satisfactory accuracy of FDTD

when used outside the high-Q resonances, while also demonstrating a significant increase in computational error near these resonances [60]. Note that complete elimination of these errors is not achieved even with denser meshing and, mathematically, the convergence of FDTD codes cannot be guaranteed.

There is big amount of investigations on improving the performance of FDTD and its agreement with the experiments [61-64]. Currently, owing to its versatility, the method serves as the foundation for commercial and open-source software packages used for analyzing, solving, and simulating a wide range of physical and engineering problems.

- *Separation of variables for single wire* (sometimes called Mie theory): the concept of separating the variables was initially introduced by Lord Rayleigh (J. Strutt) in 1881 in the analysis of waveguides [65]. This is a classical approach, which provides a rigorous mathematical framework for calculating the scattering and absorption properties of dielectric cylinders and other simple-shape objects. It takes into account the size parameter (the ratio of the wavelength of light to the particle size) and yields detailed information about the angular distribution of scattered light, extinction, and absorption efficiencies. Note that Rayleigh used this method in the case of 2-D domains with circular boundaries.

As known, EM waves obey the Maxwell equations [66]. The separation of variables solution to the canonical Maxwellian problem of the scattering of tome-harmonic EM waves by a spherical object in the frequency domain was presented by Mie in 1908 [67]. The paper [68] contains a generalization of Mie theory to the time domain. However, almost at the same time as Mie's work, Lorentz and Debye developed their own analytical solutions for the spherical scatterers [69,70]. Moreover, Logan in 1965 found and wrote a review of all "lost" pieces of knowledge of contributed authors in this theory [71]. The limited knowledge about these alternative works and complete oblivion of Rayleigh role by the 20th century have led to the commonly used terms "Mie series," "Mie approach," or "Lorentz-Debye-Mie theory" being attributed to all separation of variables solutions. In contrast to the classical

Lorentz-Mie-Debye theory (LMDT), which primarily examined the scattering of plane waves by stand-alone objects, recent research has centered around the Generalized Lorentz-Mie theory (GLMT), which studies the time-harmonic wave scattering by multiple spheres and spheroids [72-75].

Mathematically, the method of separation of variables is a commonly employed approach for solving the partial differential equations. It assumes that the solution can be expressed as a product of several functions, each dependent on a single independent variable. Following this assumption, it is possible to derive precise analytic solutions for problems concerning the scattering of EM waves by objects whose surfaces align with coordinate surfaces in certain curvilinear orthogonal systems. The exact solutions for the scattering from circular cylinders can be obtained by implementing this method, where the terms are products of cylindrical functions of the radial coordinate and trigonometric function of the azimuth coordinate, although they take the form of infinite series [77-80]. However, these series are always convergent and simple rules for the choice of their truncation order can be established.

The separation of variables method is not applicable to more complex than canonical shapes, such as circular cylinders and spheres, including layered ones. In fact, this is the only disadvantage of the method.

- *Method of Analytical Regularization* (MAR) based on single-wire part inversion. The numerical methods based on reducing the EM wave scattering problem associated with multiple circular cylinders to an infinite matrix equation, which is an equation of the second kind, have been known since long ago [77-79, 81-85]. However, the associated algorithms diverge as the order of matrix truncation increases. Sologub was apparently the first who concluded the need to cast the equations of the second kind to the Fredholm form [86]. Later and independently, Bogdanov came to the same conclusion in [87]. Fredholm's theory can be used for operator (integral or infinite-matrix) equations where the operator is a sum of a continuously invertible operator and a completely continuous operator [88]. This entails that for such operator equations, the existence of the exact solution and the convergence of the numerical code can be

mathematically established [89].

As formulated in [90], MAR is a collective name for the methods, which involve transformation of a first-kind or strongly-singular second-kind operator equation, usually derived in the wave-scattering theory, into a Fredholm second-kind operator equation – say, integral equation with a smooth (square-integrable) kernel. This ensures the point-wise convergence of typical discretization schemes. As this is achieved by analytically inverting the singular component of the original equation, MAR is also sometimes called the semi-inversion method. The term MAR was firstly introduced by Muskhelishvili in [91]. It also should be acknowledged that the concept of MAR was developed by the 19^{th} century mathematicians: Hilbert, Poincare, and Noether, in the theory of singular integral equations.

Furthermore, other functional methods such as Titchmarsh, Wiener-Hopf, Cauchy, Abel, and Riemann-Hilbert Problem techniques can be employed to achieve the analytical inversion of the static or high-frequency component of the integral operator. In certain problems, both the analytical regularization and discretization of the integral equation are carried out concurrently, resulting in methods known as analytical preconditioning [92].

If the convergence is ensured (by the Fredholm theory), the accuracy of computations can be effectively controlled by adjusting the truncation order of the matrix. In theory, the error can be minimized to the machine precision, a level of accuracy that is beyond what is achievable with commercial codes currently available.

The MAR methods, along with others, offer powerful tools for analyzing EM wave scattering from circular cylinders, enabling researchers to investigate scattering phenomena, optimize device designs, and understand the emission of waves from nanoscale structures. In this dissertation, the author applies the method of separation of variables to the analysis of the scattering from simple single-cylinder configurations. The MAR is applied to more complicated, multiple-cylinder structures, based on the analytical inversion of the single-cylinder part of the full problem.

1.2 Field of a harmonically modulated beam of charged particles

In all problems studied in this work, the incident wave is the field of the time harmonically modulated electron beam, therefore, this section is devoted to the explanation of its presentation.

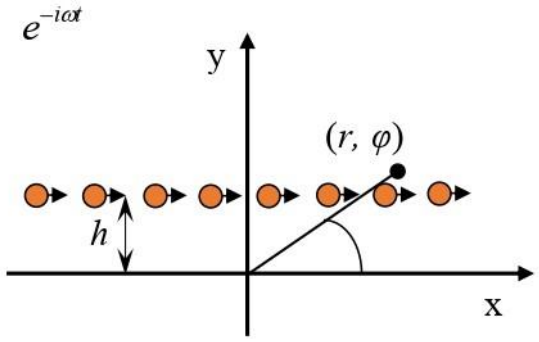

Fig. 1.1 Cross-section sketch of time-harmonically modulated beam of charged particles

Consider an unbounded two-dimensional (2D) flat electron beam moving along the straight trajectory, with a fixed velocity $v = \beta c$ (β < 1), see Fig. 1.1. The charge density function, if modulated in time in a harmonic manner, can be presented as

$$\rho = \rho_0 \delta(y - h) \exp[i(kx / \beta - \omega t)], \tag{1.1}$$

where $\delta(\cdot)$ is the Dirac delta function, ω and ρ_0 are the frequency and the amplitude of beam modulation, $k = \omega / c$ is the free-space wavenumber, $\beta = \upsilon / c \leq 1$ is the relative beam velocity, *c* is the light velocity, and *h* is the beam distance from x-axis.

We will consider the DR electromagnetic-field problems in the given-current approximation. In this case the incident wave is the field of the sheet current beam (1.1) moving in the free space. As it was shown in [3, 4], this field has the form of a slow

inhomogeneous plane wave, the only nonzero component of the magnetic field of which is

$$H_z(x,y) = A\beta \operatorname{sign}(y-h) e^{-q|y-h|} e^{ikx/\beta} \tag{1.2}$$

where $q = k\gamma/\beta, \gamma = (1-\beta^2)^{1/2}$, function $\operatorname{sign}(y-h) = \pm 1$ is the sign of the expression in the brackets, the time dependence is omitted, and *A* is a constant, which equals to $\rho_0 c/2$ in SI units. This is a surface wave running along the beam trajectory in the positive direction of the *x*-axis and decaying exponentially in the normal direction. It has a finite jump corresponding to the current at the beam trajectory. Note that field (1.2) is antisymmetric function of the coordinate y with respect to the beam trajectory that is a drastic difference from more conventional in optics plane-wave field, which is symmetric with respect to the propagation direction. To justify the considered approach, it is worth noting that, in the real life, the modulation of the electron beam can be achieved by its preliminary bunching in a periodic waveguide or through direct modulation by a laser emission [11,17].

1.3 Complex permittivity of silver as a function of frequency

As an alternative to classical high-refractive-index materials, truly nanoscale resonance effects are related to the *localized surface plasmon* (LSP) modes of deeply sub-wavelength noble-metal (gold, silver, copper) particles and wires. Here, two noble metals are especially attractive: the gold, because of its chemical stability, and the silver, due to the smallest optical losses. Noble metals can be characterized with complex relative permittivity $\varepsilon(\lambda)$ in the visible range, which has negative real part, $\operatorname{Re}\varepsilon(\lambda) < 0$, due to the dominant contribution of the plasma of the free electron gas. To showcase plasmonic effects on nanowires, silver is a preferable material due to its lower losses ($\operatorname{Im}\varepsilon(\lambda) > 0$) compared to gold or copper. In this thesis, a part of research is

dedicated to DR of the modulated beam of charged particles in the presence of silver nanowires and nanotubes. That is why, in this section it is important to explain the complex permittivity of silver material in detail.

According to the Drude theory, the complex-valued relative dielectric permittivity can be characterized analytically simple quadratic function of the frequency. This formula involves the static permittivity and the plasma frequency of the material. Accuracy of Drude theory gets worse if the frequency increases.

As an alternative, the Johnson and Christy experimental data are widely adopted to incorporate the wavelength-dependence optical response of bulk silver [93]. The spectra of the real and imaginary parts of $\varepsilon(\lambda)$ are shown in the whole visible-light range on panel (a) of Fig. 1.2 and in the ultra-violet range - on panel (b). It is worth noting that the Drude formula, being a reasonable approximation at longer waves, fails to provide accurate characterization in the ultra-violet, see [95].

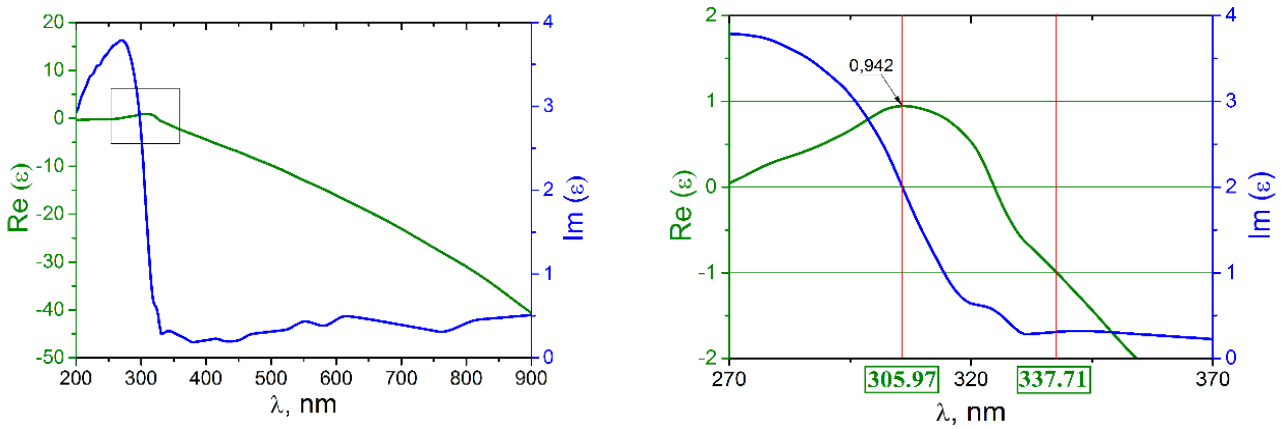

(a) (b)

Fig. 1.2 Complex relative permittivity function of bulk silver versus the wavelength in the optical range (a), and its zoom in a grey-boundary ultra-violet domain (b)

As one can see, there are two remarkable wavelengths, both laying in the ultra-violet. One is around 306 nm where $\mathrm{Re}\,\varepsilon = 0.942$ that is quite close to +1. This means that silver is optically well-transparent at this wavelength although the losses remain

significant as $\mathrm{Im}\varepsilon = 1.97$. We stress that this effect of "quasi-invisibility" cannot be reproduced with the Drude formula for the dielectric function of silver. This justifies our choice of experimental data in the analysis of silver scatterers of the visible light.

The other important wavelength value is around 337.7 nm, where $\mathrm{Re}\varepsilon = -1$. This is the approximate quasi-static "textbook" value for the collective resonance on the LSP modes of a single circular metal wire in the free space [15,17,19]. It is valid if the losses can be neglected, $\mathrm{Im}\varepsilon = 0$. Although for silver $\mathrm{Im}\varepsilon = 0.3$ at that wavelength, it predicts the LSP-caused peak of absorbance and scattering within the 5% accuracy if the silver wire is thinner than 10 nm in radius.

Note also, that the bulk permittivity is applicable if the metal sample size is significantly larger than the free-of-collisions electron path (a few nanometers).

The data of Johnson and Christy are widely acknowledged as reliable [94], however, are known only at discrete values of wavelength. To obtain the permittivity of silver at arbitrary wavelength, we employ the Akima spline interpolation algorithm. This cubic-spline technique generates smooth curves that precisely match the tabulated values, ensuring continuity and differentiability with respect to wavelength [95].

1.4 Graphene and its characteristics via the Kubo formalism

In this thesis, a part of research involves DR from circular wires, covered with one more type of plasmonic material - graphene. Therefore, here we summarize the information about graphene needed in our computations.

Graphene is new material that consists of a monolayer or a few such layers of graphite, i.e. has sub-nanometer thickness [21,96]. It has remarkable properties like transparency in the visible range, mechanic strength, and good electron conductivity in the THz and infrared (IR) ranges. The conductivity is a function of the temperature, frequency and graphene parameters. Graphene can support the plasmon guided wave at the THz and IR frequencies that makes its electromagnetic properties similar to noble metal ones in the visible-light range, however, at much lower frequencies. What is

principally new, graphene conductivity and hence plasmon effect can be tuned using the DC bias, which translates to the chemical potential [22]. Usually graphene is attached to flat dielectric substrates, however, now curved substrates attract an increasing attention [23,24]. The initial production of graphene occurred in 2004 through the mechanical exfoliation of highly oriented pyrolytic graphite [97]. Recently, graphene-covered nanowire fabrication and synchrotron nanospectroscopy measurements have been reported in [25]. More recently, a "green", safe, and fast method to prepare graphene oxide nanosheets for functional applications as an adsorbent has been developed [98]. Note that circular-wire dimers coated with graphene have been studied with commercial codes in the context of field forces [26] and cloaking [27], and with in-house code based on the local Fourier expansions in the analysis of eigenfrequencies [99].

Measuring the DR intensity in the near or far zone, one can monitor the electron-beam parameters. The resonance effects are promising for the sensor devices, such as BPM. A resonance enhances the DR intensity proportionally to associated Q-factor of the resonating mode. This approach can be extended to the THz and IR ranges if suitable resonators shaped as sub-wavelength scatterers are found. As it is described in this dissertation, one possible approach is the use of high-refractive-index materials; however, available today dielectric materials have refractive indices within several dozens, so that the resonances on their lowest modes entail only moderately sub-wavelength dimensions. The other promising approach uses the noble-metal scatterers, able to support the surface plasmon modes in the visible range; however, these modes have rather low Q-factors (5-20). The more advantageous direction way can be seen in the exploitation of the plasmon modes on the patterned graphene or graphene-coated scatterers. Note that such configurations are already studied as the elements of promising IR and THz range sensors of the host-medium refractive index [100] and tuneable filers [101,102], absorbers [103], scatterers [104] and antennas [105]. The Q-factors of the graphene plasmon modes in THz and IR ranges have moderate values (20-100) that is higher than those of a solid metal wire in the visible-light range. This makes graphene-coated dielectric micro- and nanowires attractive as resonance scatterers in

many applications including DR-based BPMs. To investigate the EM wave scattering by a graphene object, it is essential to blend the Maxwell boundary value problem with a quantum model that represents the conductivity of graphene [106].

The most widely adopted today model of the electron mobility in the graphene monolayer is the Kubo formalism [107], applied in numerous publications [108-110]. Here, the graphene thickness is considered zero, and its surface conductivity, $\sigma(\omega,\mu_c,\tau,T)$ depends on the cyclic frequency ω, chemical potential μ_c, electron relaxation time τ and temperature T. This value consists of two contributions, $\sigma=\sigma_{\text{intra}}+\sigma_{\text{inter}}$, which are the intraband and interband conductivities. Namely,

$$\sigma_{\text{intra}}=\frac{q_e^2 k_B T}{\pi\hbar^2\left(1/\tau-i\omega\right)}\left\{\frac{\mu_c}{k_B T}+2\ln\left[1+\exp\left(-\frac{\mu_c}{k_B T}\right)\right]\right\}, \tag{1.3}$$

and σ_{inter} is expressed as an integral of known functions (see [107]). If $\mu_c >> k_B T$, that integral can be reduced to simple expression,

$$\sigma_{\text{inter}}=\frac{iq_e^2}{4\pi\hbar}\ln\frac{2\mu_c-\left(\omega+i\tau^{-1}\right)\hbar}{2\mu_c+\left(\omega+i\tau^{-1}\right)\hbar} \tag{1.4}$$

Then, the normalized surface impedance (or resistivity) of graphene is

$$Z(\omega)=\frac{1}{Z_0\left(\sigma_{\text{intra}}+\sigma_{\text{inter}}\right)} \tag{1.5}$$

where $Z_0=\sqrt{\mu_0/\varepsilon_0}$ is the impedance of the free space. Note that the hexagonal fine structure of graphene has the cell size around 10 nm. Therefore, scalar infinite-sheet expressions for graphene's conductivity are applicable (have good accuracy), if the size of the patterned graphene is around 100 nm or larger. The relative contribution of two

terms into (1.5) depends on the frequency and chemical potential. This can be understood from the curves in Fig. 1.3 (a) and the color map in Fig. 1.3 (b).

The interband conductivity, in absolute value, is smaller than the intraband one, which is called the Drude model term, in a wide range from the statics to a certain high frequency, f_d [107]. The upper bound here scales with the chemical potential, due to the dominance of the term containing the factor $\mu_c\left(k_B T\right)^{-1}$ in the Kubo formulas. For instance, if $\tau = 0.5$ ps, $T = 300$ K and $\mu_c = 0.25$ eV, then $\left|\sigma_{\text{inter}}\right| \le 0.1\left|\sigma_{\text{intra}}\right|$ at the frequencies below $f_d = 40$ THz, while if $\mu_c = 0.5$ eV, then the same is valid at the frequencies below $f_d = 80$ THz. Therefore, at $f < f_d$ we can safely neglect the interband conductivity.

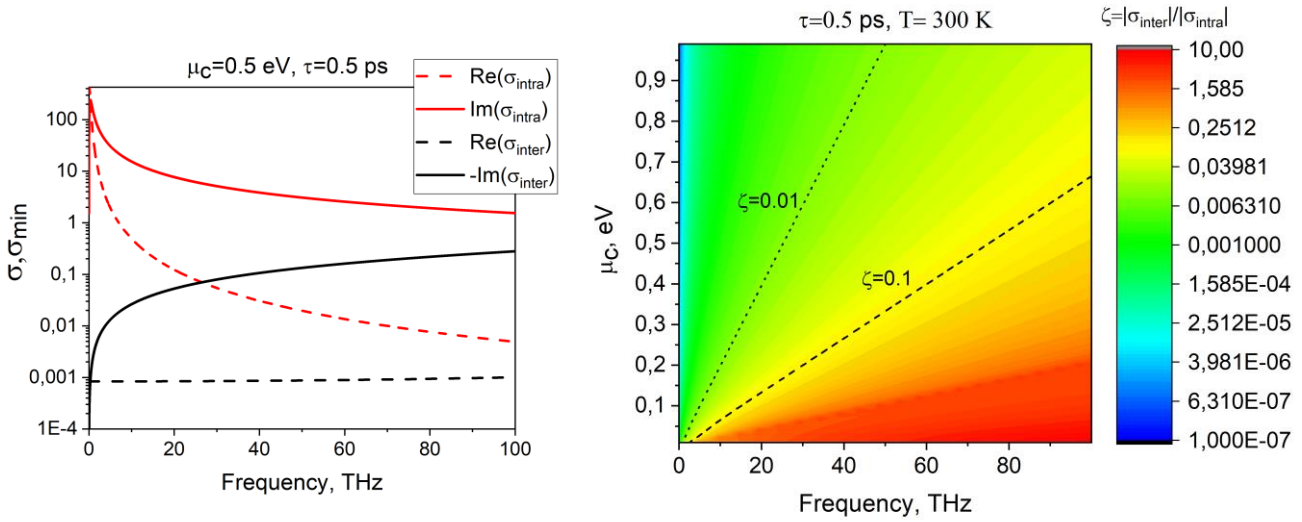

(a) (b)

Fig. 1.3 The frequency dependences of the intraband and interband surface conductivities of the monolayer graphene sheet according to the Kubo formalism (a) and the ratio of these two values as a function of the frequency and the chemical potential (b). Electron relaxation time is $\tau = 0.5$ ps, temperature is $T = 300$ K

Still, above the mentioned frequency, which lays in the near infrared or visible light range, the description of graphene should take into account both types of

conductivity. Below, we will use the full expression (1.5) in the numerical analysis and the simplified description using only the intraband term - in the analytical characterization of the plasmon mode frequencies and thresholds.

1.5 Scattering and absorption cross-sections, optical theorem

This section provides an overview of the scattering and absorption characteristics used in our studies, as well as the *Optical Theorem* (OT) that establishes their relationship.

When a particle is exposed to a time-harmonic EM plane wave with specific attributes, the power and angular dispersion of the scattered light, as well as the absorbed power, are intricately dependent on the particle's inherent properties such as shape, size, orientation, and composition materials. Still, these powers obey the power conservation law. Similar to the plane-wave case, the scattering of electron beam field from individual scatterers or their finite ensembles follows specific regularities that stem from the same law of power conservation. Consider at first the plane-wave, $H_z^{\text{int}} = e^{ikx}$, scattering – see Fig.1.4 (a).

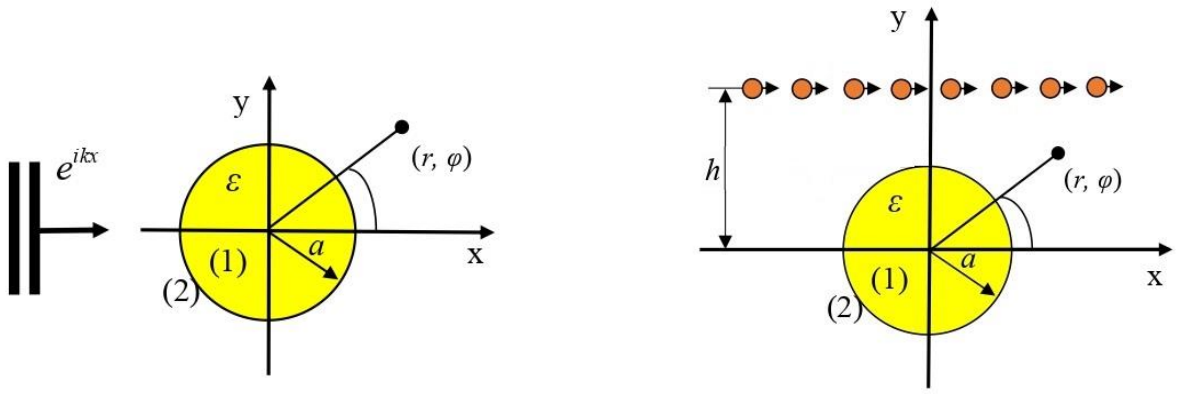

(a) (b)

Fig. 1.4 Cross-sectional geometry of a plane wave incident on a circular dielectric wire (a) and an electron beam moving near the same wire (b)

The *total scattering cross section* (TSCS) serves as a convenient characteristic of the scattering efficiency. It is introduced as an integral over all possible directions in space from the radial component of the averaged over the period Poynting vector (power transfer vector) of the scattered field.

$$\sigma_{sc} = \frac{1}{\mathrm{Re}\,\Pi^{in}} \lim_{r\to\infty} \oint_{S_r} \mathrm{Re}\,\Pi_r^{(2)} ds = \frac{1}{\mathrm{Re}\,\Pi^{in}} \lim_{r\to\infty} \int_0^{2\pi} \mathrm{Re}\,\Pi_r^{(2)} r dr d\varphi, \tag{1.6}$$

where in the case of the H-polarization $\Pi_r^{(2)} = \frac{1}{2} E_\varphi H_z^*$, and Π^{in} is the amplitude of the Poynting vector of the incident plane wave. If an incident plane wave is H-polarized and has a unit amplitude, then $\Pi^{in} = Z_0 / 2$.

Taking into account that E_φ is expressed through H_z by means of

$$E_\varphi = \frac{1}{ik\varepsilon} Z_0 \frac{\partial H_z}{\partial r}, \tag{1.7}$$

and H_z has the form $H^{(2)}(r,\varphi) \sim \sqrt{2/(i\pi k_2 r)} e^{ik_2 r} \Phi(\varphi)$ in the far zone (this is the Sommerfeld radiation condition), we get that

$$\sigma_{sc} = \frac{2}{\pi k} \int_0^{2\pi} |\Phi(\varphi)|^2 d\varphi, \tag{1.8}$$

The absorption cross-section (ACS) serves for characterizing the averaged over the period power, which is absorbed by lossy material. For instance, for graphene-covered lossless circular dielectric wire it is given as

$$\sigma_{abs} = \frac{\mathrm{Re}\,Z}{Z_0} \mathrm{Re} \int_0^{2\pi} E_\varphi H_z^* d\varphi, \tag{1.9}$$

where Z is the normalized surface impedance of graphene, see section 1.4.

This quantity can be also reduced to the following form:

$$\sigma_{abs} = \pi R \operatorname{Re} Z \int_0^{2\pi} |w(\varphi)|^2 \, d\varphi, \tag{1.10}$$

where $w^{(i)}(a,\varphi) = H_z^{ext}(a,\varphi) + H_z^0(a,\varphi) - H_z^{\text{int}(i)}(a,\varphi)$ is the surface current induced on the graphene cover.

The sum of SCS and ACS is known as the extinction cross-section (ECS), $\sigma_{ext} = \sigma_{sc} + \sigma_{abs}$. In the plane wave scattering, this quantity is linked to the far-field scattering pattern magnitude in the forward direction by the expression known as Optical Theorem [19],

$$\sigma_{ext} = -\frac{4}{k} \operatorname{Re} \Phi(0), \tag{1.11}$$

As follows from (1.11), ACS can be also found from only the far-field quantities,

$$\sigma_{abs} = -\frac{4}{k} \operatorname{Re} \Phi(0) - \sigma_{sc}, \tag{1.12}$$

OT has the physical meaning of the law of conservation of the electromagnetic field power when a plane time-harmonic wave is scattered by a certain body located in the fire space. To derive (1.11), one has to take the real part of the Poynting Complex Theorem, applied to two functions: the total field and its complex conjugate, in a finite region, which is bounded by two non-intersecting surfaces, inner and outer, and the scattering body is inside the inner surface. After contracting the inner surface to the origin of coordinates, and stretching the external one to the sphere of large radius, one uses the boundary and the radiation condition, respectively, to arrive at the final result.

Therefore, OT is a convenient and powerful tool for partially checking the

calculations correctness. However, one should keep in mind that this is only a necessary condition of the correctness, and not a sufficient one.

Turning now to the DR of a modulated electron beam (see Fig. 1.4 (b)), we have not a plane wave incident on a scatterer, but the field (1.2) of section 1.2.

Nevertheless, if we take into account that the scatterer on panel (b) is located *below* the beam trajectory and introduce the complex incidence angle ψ , such that

$$\cos\psi = 1/\beta, \quad \sin\psi = i\gamma/\beta, \tag{1.13}$$

then we can present the incident field (1.2) as generalized plane wave,

$$H_z(x, y < h) = -A\beta e^{-iqh} e^{ikx\cos\psi + iky\sin\psi}, \tag{1.14}$$

Now, we can repeat all steps of the plane-wave case, normalize the scattered power by the maximum value of the (1.14) Poynting vector $Z_0(A\beta)^2/2$, and obtain

$$\sigma_{sc} = \frac{2}{\pi k}\int_0^{2\pi} |\Phi(\varphi)|^2 d\varphi, \tag{1.15}$$

Similarly, we derive the OT, adapted to the DR of the modulated electron beam,

$$\sigma_{ext} = -\frac{4}{k}\mathrm{Re}\,\Phi(\psi) \tag{1.16}$$

1.6 Lasing Eigenvalue Problem

In the scope of the dissertation research, the author has also studied the natural modes of circular nanowire configurations, using the lasing eigenvalue problem (LEP). Thus, the LEP statement is introduced in this subsection in detail.

From the viewpoint of the Maxwell theory of time-harmonic EM waves, the lasing can be conveniently viewed as the existence of the real-valued eigenfrequency (natural mode frequency) of an open resonator.

As follows from the Poynting theorem, arbitrary passive open resonator eigenfrequencies can be only complex, with non-zero imaginary parts that corresponds to finite radiation losses. Therefore, in order to emit electromagnetic wave, which does not attenuate in time, an open resonator must contain an active zone filled in with the gain material. In practice, such “quantum” materials can be various semiconductors, dye-doped polymers, or crystalline materials doped with ions of erbium or some other rare-earth elements. All of them are able to demonstrate, under pumping, the inverse population of electronic levels and the stimulated emission of light. Within macroscopic electromagnetics, these properties are translated to the "negative losses" that is expressed, for non-magnetic materials, by the corresponding sign of the imaginary part of the dielectric permittivity, $\mathrm{Im}\,\varepsilon$, and refractive index $\mathrm{Im}\sqrt{\varepsilon}$. If the time dependence is chosen as $e^{-i\omega t}$, then the gain material has $\mathrm{Im}\,\varepsilon < 0$ and $\mathrm{Im}\sqrt{\varepsilon} < 0$.

Therefore, for a generic cavity under the pumping (Fig.1.5), the LEP assumes that at least a part of the cavity domain is filled in with a gain material that is nonmagnetic and has a complex refractive index with nonzero negative imaginary part, $\nu = \alpha - i\gamma$, where α is known refractive index and $\gamma > 0$ is unknown threshold gain index. The surrounding media is assumed nonmagnetic as well and lossless [111]. Passive dielectric cavities are known to possess an infinite number of discrete complex-valued natural frequencies or wavenumbers k_s, each associated with certain natural mode or non-zero EM field, $\{\mathbf{E}_s, \mathbf{H}_s\}$ (s = 1,2, …). The active region, thanks to the gain

material, allows for the compensation of radiation losses associated with any specific mode, resulting in the real-valued natural wavenumber ($k_s = \mathrm{Re}\, k_s$) for that mode. The related threshold gain value $\gamma_s > 0$ is mode-specific, i.e. is different for different modes. From the mathematical point of view, the search for the real values of k_s and γ_s, and the associated modal fields in the near and far zones can be formulated as an electromagnetic eigenvalue problem, i.e. similar to the scattering problem but without the incident field [112].

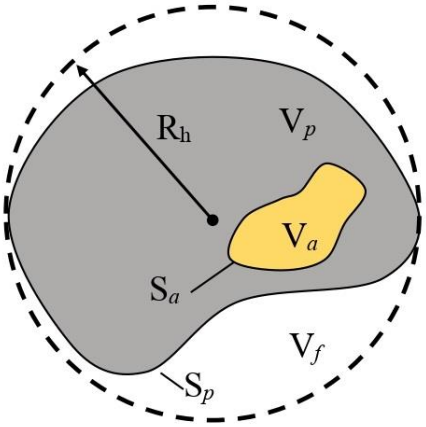

Fig. 1.5. Cross-sectional geometry of a generic open resonator, equipped with an active region, V_a. Here, V_p and V_f are the passive and free-space parts of the resonator. R_h is the radius of the open resonator volume - see [149] for details

Thus, within the LEP, one has to look for such pairs of real numbers (k_s, γ_s) that generate non-zero functions $\mathbf{E}_s, \mathbf{H}_s$, which solve the full-wave boundary-value problem for the Maxwell equations with exact boundary conditions and radiation condition at infinity. The linear nature of a boundary-value problem for the LEP is justified by the zero field amplitude of any real laser as dynamic source at the threshold.

Note that, after discretization, the LEP is always reduced to a complex-valued

transcendental or determinantal equation. This yields two equations, for the vanishing of the real and imaginary parts, i.e. exactly what is needed to find the pair (k_s,γ_s). It is also important to emphasize that a real value for k_s indicates that the natural mode at the lasing threshold does not experience time decay and its field follows typical spatial decay pattern of either cylindrical wave, $O(\mathrm{R}^{1/2})$ in 2-D, or spherical wave, $O(\mathrm{R}^{-1})$ in 3-D. Therefore, the condition at infinity can be taken as conventional Sommerfeld or Silver-Muller condition of radiation, respectively.

Since 2004, the LEP-based analyses have been performed and published for the modes of various 2-D cavities with active regions: stand-alone circular ones [112], dimers [122] and cyclic photonic molecules [121] of circular active cavities, kite-shaped [111], elliptic [151], and other ones. One of the most impressive results was the explanation, using LEP, of the fact that the lowest-thresholds modes of elliptic cavity with centered circular active region are not the whispering-gallery (WG) modes but the so-called bow-tie modes. The reason is that the latter modes have much larger overlap between the mode electric field and the active region, than the former.

More recently, LEP approach has been successfully applied to quantify the threshold conditions of 2-D noble-metal nanolasers shaped as silver strip [152] and silver tube [153] inside the active circular wire.

It is worth to note that the other LEP-like formulations exist, see [113-117], where the threshold gain is characterized with the aid of $\mathrm{Im}\,\varepsilon<0$ instead of γ or with the product, $g=k\gamma$, which is the gain per wavelength.

Note that, in reality, the gain index of active material depends on the frequency, usually as a bell-like function reaching maximum at a certain central frequency, say, ω_c, which is material-specific. To reflect the frequency dispersion of the gain index, one can introduce the latter function into the LEP as, say, $\gamma=\bar{\gamma}\exp[-\omega_c^2(\omega-\omega_c)^2]$, and then look for the mode-specific eigenvalue pairs $(k_s,\bar{\gamma}_s)$. Still, even without this modification, LEP enables one to compare various modes by their thresholds.

Conclusions to Chapter 1

- In this Chapter, several methods of analysis of EM diffraction from circular dielectric cylinders have been presented briefly and their advantages and disadvantages have been discussed. The convergence of MAR is emphasized.
- The time-harmonically modulated electron beam field has been presented and described. It is emphasized that this field (i) is H-polarized, (ii) is a slow surface wave, compressed to the beam trajectory, (iii) is anti-symmetric with respect to the trajectory, (iv) its jump across the trajectory equals the beam current.
- The complex permittivity of a noble metal such as silver has been explained. The experimental data by Johnson and Christy has been discussed as providing important advantages before the Drude description.
- Important for the research graphene characteristics, such as conductivity and surface impedance have been presented, based on the Kubo formalism.
- The Optical Theorem has been derived, adapted to the DR effect, i.e. for the incidence of the field of beam of charged particles. It establishes a relationship between the total scattering and absorption cross-sections, and the far-field angular pattern in certain complex-valued direction.
- The Lasing Eigenvalue Problem statement for the open resonators equipped with active regions filled in with a gain material, has been explained.

The presented reference data are used below and in publications [A1-A25].

CHAPTER 2 DIFFRACTION RADIATION OF A BEAM OF PARTICLES MOVING NEAR DIELECTRIC NANOWIRES

In this section, the DR-caused scattering and absorption characteristics in the visible range are investigated for a single circular dielectric nanowire and dimer of twin circular dielectric nanowires, excited by a modulated electron beam. Research method is based on use of semi-analytical technique, which exploits the Fourier expansions in the local coordinates of each wire and the addition theorems for the cylindrical functions. As a result, single dielectric wire's resonance DR fields are investigated and identified as linear combinations of two degenerate modes of a circular cavity. For the dimer, the modes are the supermodes, built on the natural modes of each of the twin dielectric cavities combined together according to the two-fold symmetry. The results of chapter 2 have been published in works [A5, A6, A18-21, A25].

2.1 Scattering problem formulation for finite number of circular wires

As far as all considered problems involve the incident field in the form of the modulated electron beam field and the circular cylinder scatterers, this section is devoted to the introduction of the generic DR problem formulation for the finite number of circular dielectric nanowires.

We investigate the problem of the electron beam field scattering from M circular identical dielectric nanowires with radius a, located in the free space (i.e., in vacuum or air) as it is shown in Fig. 2.1. Let us denote the internal region of the p-th wire as region (1.p), and the external region to all wires or the enclosing medium as region (2). It should be noted that the wires located under the beam trajectory are numbered as $p = 1,...,M_1$, meanwhile the wires located above the beam trajectory are numbered as $p = M_1 + 1,...,M$. We introduce Cartesian and polar coordinates: global one with the origin on the first wire axis, $\vec{r} = (x, y)$ and $\vec{r} = (r, \varphi)$, that as $x = r\cos\varphi, y = r\sin\varphi$ and

$r = \sqrt{x^2 + y^2}$, $\varphi = \arctan(x / y)$, and M local ones with origins at each wire axis. Besides, we assume that the time dependence of the field has the form $e^{-i\omega t}$, where ω is the cyclic frequency. The dielectric constant of the nanowires is equal to $\varepsilon = \varepsilon' + i\varepsilon''$, and all materials are non-magnetic. Then the refractive index of the wire material is equal to $\alpha = \sqrt{\varepsilon}$. We consider the diffraction radiation accompanying the uniform motion of a flat 2-D electron beam in the approximation of the given current, as it has been introduced in section 1.2.

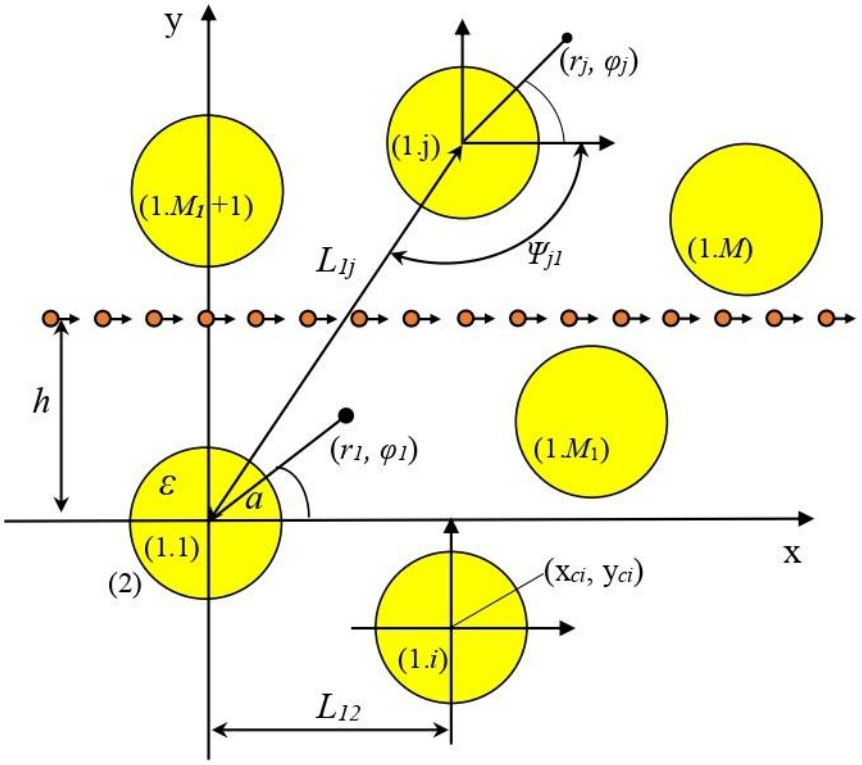

Fig. 2.1 Cross-sectional geometry of a flat zero-thickness electron beam moving near M identical circular dielectric nanowires

As mentioned before, if we assume the electron beam velocity to be constant, then the DR problem can be viewed as a classical wave-scattering boundary value problem, where the incident field is the function (1.2). Then, the DR field has to satisfy

the following conditions:

1. The Helmholtz equation with coefficient $k_{\text{int}} = \alpha k$ in internal domain, (1.p), where p=1,…M, and $k_{ext} = k = \omega / c$ in the external domain (2),

$$(\Delta + k_{\text{int},ext}^2) H^{(\text{int},ext)}(r,\varphi) = 0, \tag{2.1}$$

2. The boundary conditions on the surface (on the contour) of each wire, which are the continuity conditions for the tangential components of the EM field at $r = a$ and $0 \le \varphi < 2\pi$,

$$H_z^{\text{int}}(a,\varphi) = H_z^0(a,\varphi_p) + H_z^{ext}(a,\varphi_p), \tag{2.2a}$$

$$E_\varphi^{\text{int}}(a,\varphi) = E_\varphi^0(a,\varphi) + E_\varphi^{ext}(a,\varphi) \text{ or } \left.\frac{\partial H_z^{\text{int}}(r,\varphi)}{\varepsilon\, \partial r}\right|_{r=a} = \left.\frac{\partial H_z^0(r,\varphi)}{\partial r}\right|_{r=a} + \left.\frac{\partial H_z^{ext}(r,\varphi)}{\partial r}\right|_{r=a}, \tag{2.2b}$$

Note that from Maxwell's equations it follows that the electric and magnetic field components are connected as in (1.7)

3. The condition for the local power finiteness,

$$\int_{S \subset R^2} \left(\varepsilon' \left|\vec{E}\right|^2 + Z_0^{-2} \left|\vec{H}\right|^2 \right) r dr d\varphi < \infty, \tag{2.3}$$

where $Z_0 = \sqrt{\mu_0 / \varepsilon_0}$ is the free-space impedance.

4. The Sommerfeld radiation condition at infinity (outgoing wave behavior),

$$H_z^{ext}(r,\varphi) \sim \sqrt{\frac{2}{i\pi kr}} e^{ikr} \Phi(\varphi) \text{ at } r \to \infty. \tag{2.4}$$

where the function $\Phi(\varphi)$ of one variable (the azimuth coordinate φ) is called the

angular scattering pattern in the far zone.

It can be proved that conditions (2.2) - (2.4) guarantee the uniqueness of the solution, if only $\varepsilon'' \geq 0$, that is, the wire consists of a lossy $(\varepsilon'' > 0)$ or passive $(\varepsilon'' = 0)$ material. This follows from the Poynting Complex Theorem: if we assume the opposite (that there are two different $H^{sc}(\vec{r})$ for the same $H^{0}(\vec{r})$, then this theorem leads to an expression with incompatible signs on the right and left hand sides.

2.2 Casting the problem to the Fredholm 2-nd kind matrix equation

To reduce the DR problem to a well-conditioned algebraic equation, we represent the total magnetic field as follows (here and further, the index *z* is omitted):

$$H^{tot} = \begin{cases} H^{int(p)},\ r \in \{1.p\} :\ r_p < a_p, \quad p = 1...M \\ H^{0} + H^{ext},\ r \in \{2\} : \mathbb{R}^2 \setminus \bigcup_{p=1}^{M} \{1.p\} \end{cases}, \tag{2.5}$$

The magnetic field in domains $(1.p)$ and (2) is represented as ($p = 1...M$)

$$H^{int(p)}(r,\varphi) = \sum_{n=-\infty}^{\infty} y_n^{(p)} J_n(k\alpha r_p) e^{in\varphi_p},\ (r,\varphi) \in \{1.p\}, \quad \text{Internal} \tag{2.6}$$

$$H^{ext}(r,\varphi) = \sum_{p=1...M} \sum_{n=-\infty}^{\infty} z_n^{(p)} H_n^{(1)}(kr_p) e^{in\varphi_p},\ (r,\varphi) \in \{2\}, \quad \text{External} \tag{2.7}$$

where $y_n^{(p)}$, $z_n^{(p)}$ are unknown coefficients, $H_n^{(1)}(\cdot)$ and $J_n(\cdot)$ are the first-kind Hankel and the Bessel functions, respectively. Note that the series (2.6) and (2.7) satisfy the Helmholtz equations (2.1), the condition of the local power finiteness (2.3), and the radiation condition (2.4). To determine the unknown expansion coefficients, these series are substituted into the boundary conditions (2.2) at the contours of the wires, and the

addition theorems for the Bessel and Hankel functions are used [159].

For several nanowires, we use the Graf's theorem (Fig. 2.2) as follows:

$$Z_v(kr_p)e^{iv\psi} = \sum_{n=-\infty}^{\infty} J_n(kr_j)Z_{v+n}(kL_{pj})e^{in\theta}, r_j < L_{pj}, \quad (2.8)$$

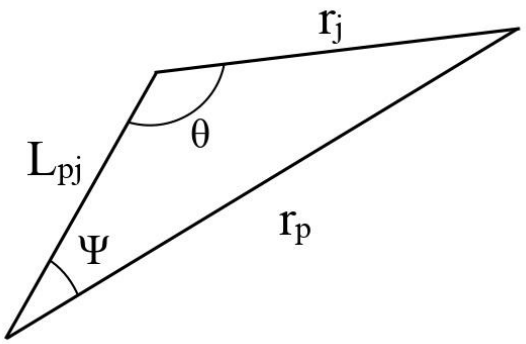

Fig. 2.2 Graf's theorem explanation geometry

Here, Z_v is arbitrary cylindrical function. In our case, as it shown in Fig. 2.1, taking into consideration the correspondent angles, $\psi_{pj} = \pi - \psi_{jp}$, $\theta = \varphi_j + \pi - \psi_{pj}$, and $\varphi = \psi_{pj} - \varphi_p$, equation (2.8) takes the following form:

$$H_m^{(1)}(kr_j)e^{im\varphi_j} = \sum_{n=-\infty}^{\infty} H_{n-m}^{(1)}(kL_{pj})J_n(kr_p)e^{i(m-n)\psi_{pj}}e^{in\varphi_p},\ r_p < L_{pj},\ j \neq p = 1,2...M, \quad (2.9)$$

In the near and far field zone, respectively, this yields

$$H_m^{(1)}(kr_j(P))e^{im\varphi_j(P)} = \sum_{n=-\infty}^{\infty} H_{n-m}^{(1)}(kr_{pj})J_n(kr_p(P))e^{i(m-n)\psi_{pj}}e^{in\varphi_p(P)},\ r_p(P) < L_{pj}, \quad (2.10)$$

$$H_m^{(1)}(kr_j(P))e^{im\varphi_j(P)} = \sum_{n=-\infty}^{\infty} J_{n-m}(kr_{pj})H_n^{(1)}(kr_p(P))e^{i(m-n)\psi_{pj}}e^{in\varphi_p(P)},\ r_p(P) > L_{pj}, \quad (2.11)$$

Further, we expand the incident field, i.e. the field of the modulated electron beam (1.2) in the Fourier series in each of the local polar coordinates,

$$H^0(r_p,\varphi_p)=-A\beta e^{q(y_{cp}-h)}e^{ikx_{cp}/\beta}\sum_{m=-\infty}^{+\infty} i^m J_m(kr_p)\left(\frac{1-\gamma}{\beta}\right)^m e^{im\varphi_p},\ p=1,...,M_1, \quad (2.12)$$

$$H^0(r_p,\varphi_p)=A\beta e^{-q(y_{cp}-h)}e^{ikx_{cp}/\beta}\sum_{m=-\infty}^{+\infty} i^m J_m(kr_p)\left(\frac{1+\gamma}{\beta}\right)^m e^{im\varphi_p},\ p=M_1+1,...,M, \quad (2.13)$$

Using the boundary conditions (2.2a) and (2.2b) with the Graf theorem (2.9), and after the exclusion of all coefficients $y_n^{(p)}$, we obtain a block type (M x M) infinite-matrix equations for the remaining coefficients. Omitting the superscript of the Hankel function and using the prime to mark the differentiation in argument, we get

$$x_m^{(p)}+\frac{V_m}{w_m D_m}\sum_{\substack{j=1\\ j\neq p}}^{M}\sum_{n=-\infty}^{+\infty} x_n^{(j)} w_n H_{m-n}(kL_{pj})e^{i(n-m)\psi_{pj}}=\frac{F_m^{(p)}}{w_m D_m}, \quad (2.14)$$

where $x_n^{(p)}=z_n^{(p)}w_n$, $w_{n<0}=(-1)^n w_{n>0}$, $w_{n>0}=n!(2/ka)^n$,

$$V_m=\alpha^{-1}J_m(ka)J_m'(k\alpha a)-J_m'(ka)J_m(k\alpha a), \quad (2.15)$$

$$D_m=\alpha^{-1}H_m(ka)J_m'(k\alpha a)-H_m'(ka)J_m(k\alpha a), \quad (2.16)$$

$$F_m^{(p)}=\beta\left[f_m^{(p)}(ka)J_m'(k\alpha a)\alpha^{-1}-J_m(k\alpha a)f_m'^{(p)}(ka)\right], \quad (2.17)$$

where, according to (2.12), the following expressions are established:

$$f_m^{(p)}=\begin{cases}-Ae^{q(y_p-h)}e^{ikx_p/\beta}i^m J_m(ka)(1-\gamma)^m\beta^{-m},\ p=1,...,M_1\\ Ae^{-q(y_p-h)}e^{ikx_p/\beta}i^m J_m(ka)(1+\gamma)^m\beta^{-m},\ p=M_1+1,...,M\end{cases}, \quad (2.18)$$

$$f_m'^{(p)} = \begin{cases} -Ae^{q(y_p+h)}e^{ikx_p/\beta}i^m kJ_m'(ka)(1-\gamma)^m\beta^{-m}, \ p=1,...,M_1 \\ Ae^{-q(y_p-h)}e^{ikx_p/\beta}i^m kJ_m'(ka)(1+\gamma)^m\beta^{-m}, \ p=M_1+1,...,M \end{cases}. \quad (2.19)$$

As can be verified, the obtained equation (2.14) is of the Fredholm second kind.

2.3 Single dielectric nanowire: resonances on whispering gallery modes

In this section, the DR from the modulated beam of electrons flowing near a single circular dielectric wire is considered. It can be expected that a high refractive index nanowire behaves as an open resonator, thanks to which the radiated power can be enhanced near the natural-mode wavelengths.

2.3.1 Basic equations

The cross-sectional geometry and notations of the studied single-wire DR problem is shown in Fig. 1.4 (b). The circular shape of the wire boundary suggests the use of the method of separation of variables. This means we expand the field functions in each domain in the Fourier series in the angular coordinate φ. In particular, if $y<h$, then the beam field (1.2) can be presented in the form of generalized plane wave (1.14),

$$H_z^{\,in}(\vec{r}) = -A\beta e^{-qh}e^{ikr\cos(\varphi-\psi)}, \quad (2.20)$$

where $A=c\rho_0/2$ and the complex incidence angle ψ is defined via (1.13). Then, taking into account the stand-alone wire configuration (M_1=1), we simplify (2.12) as

$$H_z^{\,0}(\vec{r}) = -A\beta e^{-qh}\sum_{m=-\infty}^{+\infty} i^m J_m(kr)(1-\gamma)^m\beta^{-m}e^{im\varphi}, \quad (2.21)$$

The scattered field is expanded as

$$H_z^{sc}(\vec{r}) = \sum_{m=-\infty}^{+\infty} \begin{Bmatrix} a_m J_m(k_1 r), & r < a \\ b_m H_m^{(1)}(kr), & r > a \end{Bmatrix} e^{im\varphi}, \tag{2.22}$$

where a_m, b_m are unknown coefficients, which are found using the conditions (2.1)-(2.4). Note that, if $M = M_1 = 1$, then the general matrix equation (2.14), turns into direct formulas, because the second term in the left-hand part vanishes. Thus, we obtain

$$a_m = \left[f_m(ka) H'_m(ka) - H_m(ka) f'_m(ka) \right] \left(D_m \right)^{-1}, \tag{2.23}$$

$$b_m = \left[f_m(ka) \alpha^{-1} J'_m(k\alpha a) - J_m(k\alpha a) f'_m(ka) \right] \left(D_m \right)^{-1}, \tag{2.24}$$

$$f_m = -A\beta e^{-qh} i^m J_m(ka)(1-\gamma)^m \beta^{-m}, \quad f'_m = -A\beta e^{-qh} i^m J'_m(ka)(1-\gamma)^m \beta^{-m}, \tag{2.25}$$

$$D_m = J_m(k\alpha a) H'_m(ka) - \alpha^{-1} J'_m(k\alpha a) H_m(ka), \tag{2.26}$$

Here, characteristic equations of the circular dielectric wire natural modes are

$$D_m(k) = 0, \quad m = 0, \pm 1, \pm 2, \ldots, \tag{2.27}$$

As known, they may have complex solutions, k_{mn}, which form a discrete set with negative imaginary parts. These are complex wavenumbers of the natural modes, usually denoted as $H_{m,n}$, where $m = 0,1,\ldots$ and $n = 1,2,\ldots$.

2.3.2 Numerical results: resonances on the nanowire modes

Using the analytical expressions (2.21) – (2.24), we have studied the DR characteristics for the scatterer shaped as a circular dielectric wire. Note that the series

in (2.21) and (2.22) should be truncated to finite order, N_{tr} [41]. It can be shown that D correct digits in the series are provided by the value of $N_{tr} = ka\sqrt{\varepsilon}/\beta + D + 1$ or larger. The plots in Fig. 2.3 demonstrate the dependences of the DR-caused normalized TSCS on the modulation wavelength in the visible range, for the wire with the radius 50 nm, relative dielectric constant $\varepsilon = 12$ (silicon), the separation distance h = 10 nm, and several values of the relative beam velocity β. As one can see, due to rather high optical contrast of silicon, even such a tiny wire behaves as an open nanocavity.

Indeed, for all values of the relative beam velocity β the spectra of TSCS display three distinctive peaks in the visible and ultra-violet ranges. Their wavelengths positions at 464 nm, 306 nm, and 225 nm do not depend on the relative beam velocity β.

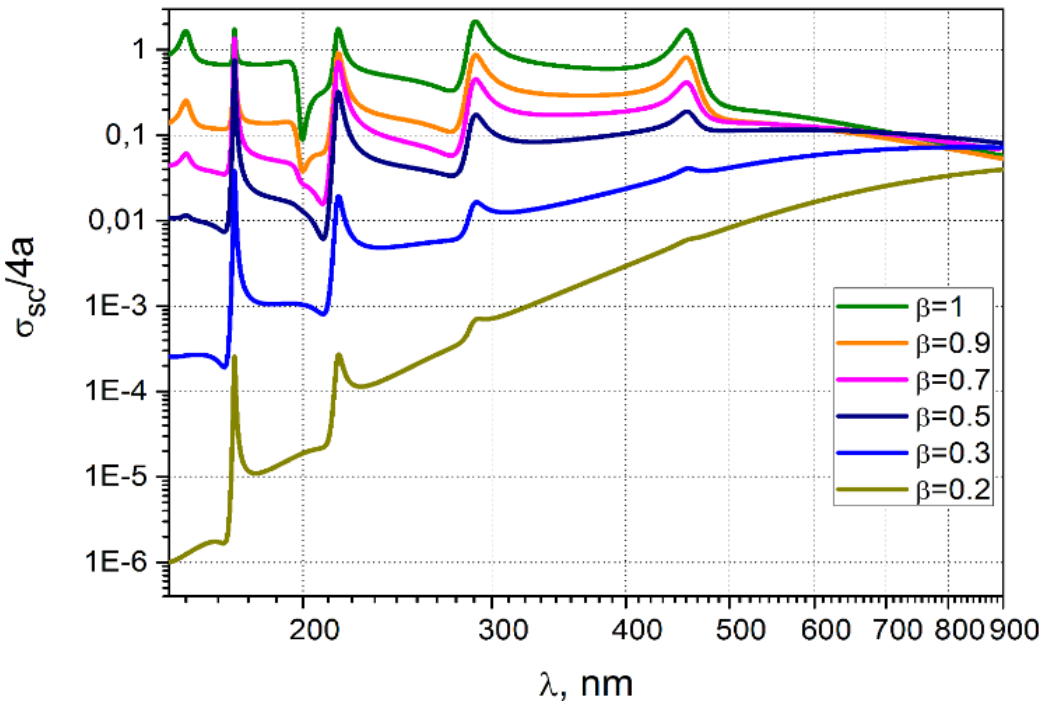

Fig. 2.3 Normalized TSCS of the 50-nm in radius lossless silicon nanowire ($\varepsilon = 12$) versus the wavelength in the visible range, for several values of the electrons' relative velocity β. Note the resonances on the wire modes

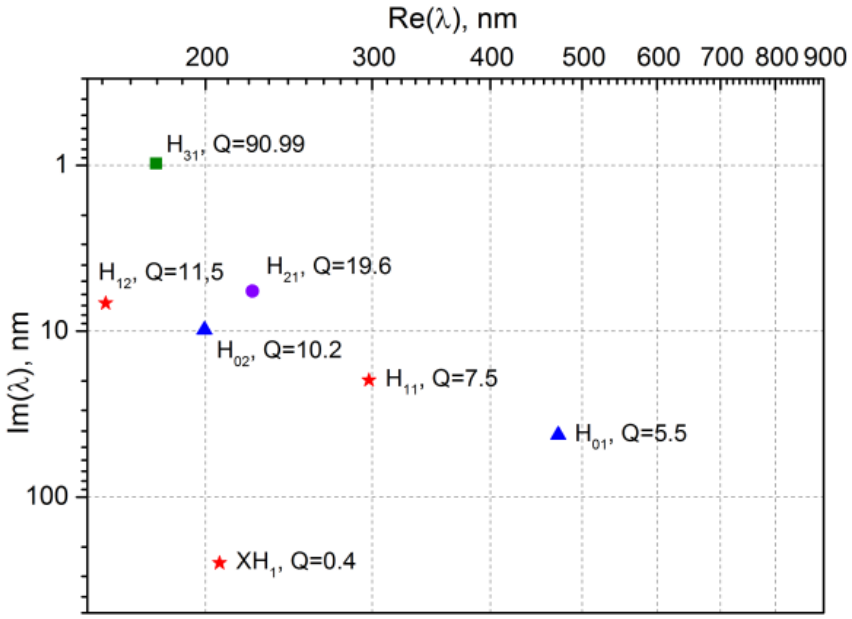

Fig. 2.4 Complex eigenvalues of the lossless circular silicon nanowire in the visible range

To clarify the nature of these peaks of TSCS, we have calculated the complex eigenvalues of the dielectric nanowire, as the roots of characteristic equation (2.26). They are presented in Fig. 2.4. There are four modes which have their wavelengths between 150 nm and 900 nm. The most "blue" of them, H_{21}, has the largest Q-factor. The mode denoted XH_1 corresponds to the so-called external mode of a circular dielectric cylinder, the existence of which was revealed, for instance, in Dettmann et al. [118]. They have very low Q-factors and do not produce any distinctive peaks in the spectra of TSCS and ACS. Other internal modes with high Q-factors are found in the deep ultraviolet range below 200 nm. The near field patterns of the internal modes with complex eigenvalues are presented in Fig. 2.5.

The panels of Figs. 2.6 show the in-resonance near field patterns for the same dielectric nanowire as in Fig. 1.4(b) and two values of β. One can clearly see the straight trajectory of the beam at the distance h = 10 nm above the wire. The lowest resonating mode, in frequency, is the H_{01} mode at 464 nm that is certified by the single bright spot near to wire's center.

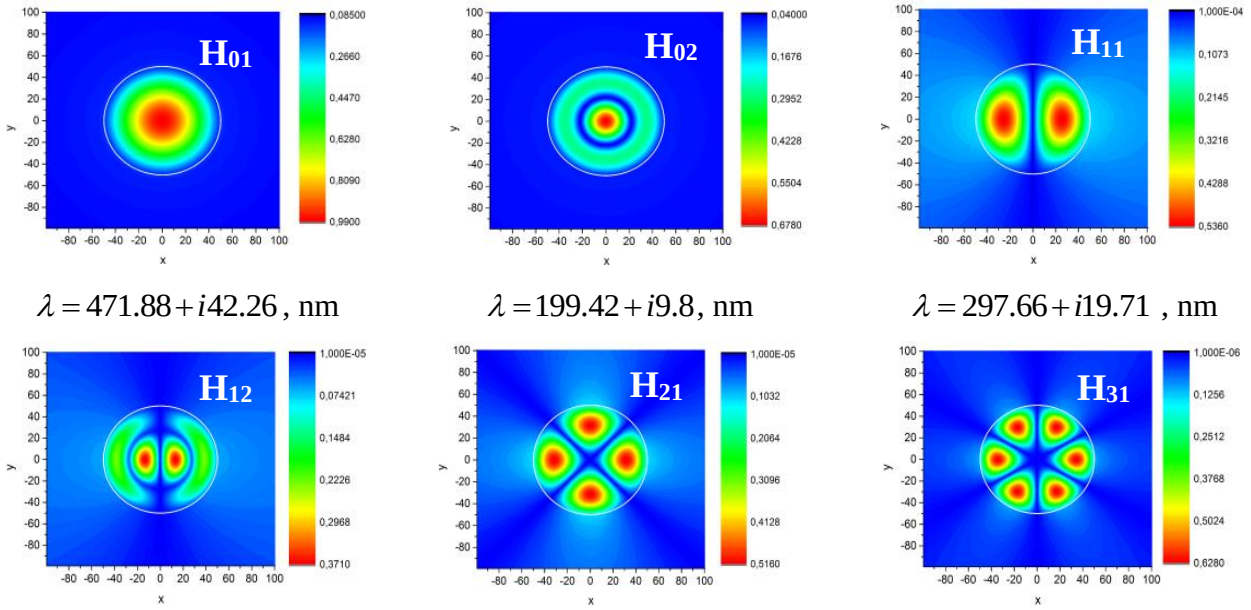

$\lambda = 471.88 + i42.26$, nm $\quad \lambda = 199.42 + i9.8$, nm $\quad \lambda = 297.66 + i19.71$, nm

$\lambda = 156.84 + i6.78$, nm $\quad \lambda = 224.21 + i5.73$, nm $\quad \lambda = 177.37 + i0.97$, nm

Fig. 2.5 Near field patterns of the lowest-order internal eigenmodes of 50-nm in radius silicon nanowire with the wavelengths between 150 nm and 900 nm

The next, in frequency, is the dipole mode H_{11} at 306 nm showing two bright spots. The most high-frequency peak at 225 nm is on the quadrupole mode H_{21}. This field pattern is well visible for the relativistic beam DR, as at $1-\beta << 1$ the beam field (1.2) is very close to a plane wave, albeit with a jump at the beam trajectory.

Here, it is necessary to remind that if $\beta \neq 0$ the incident field (1.2) is not symmetric with respect to the wire section by the *x*-axis.

Indeed, for instance, the field (2.22) inside the wire can be rewritten as

$$H_z^{sc}(\vec{r}) = -\frac{2A\beta e^{-qh}}{\pi ka}\sum_{m=0}^{\infty} i^m J_m(k_1 r) D_m^{-1}\left[B_m^{+}\cos m\varphi + iB_m^{-}\sin m\varphi\right], \qquad (2.28)$$

where

$$B_m^{\pm}(\beta) = \left[(1-\gamma)^m \pm (1-\gamma)^m\right]\beta^{-m}. \qquad (2.29)$$

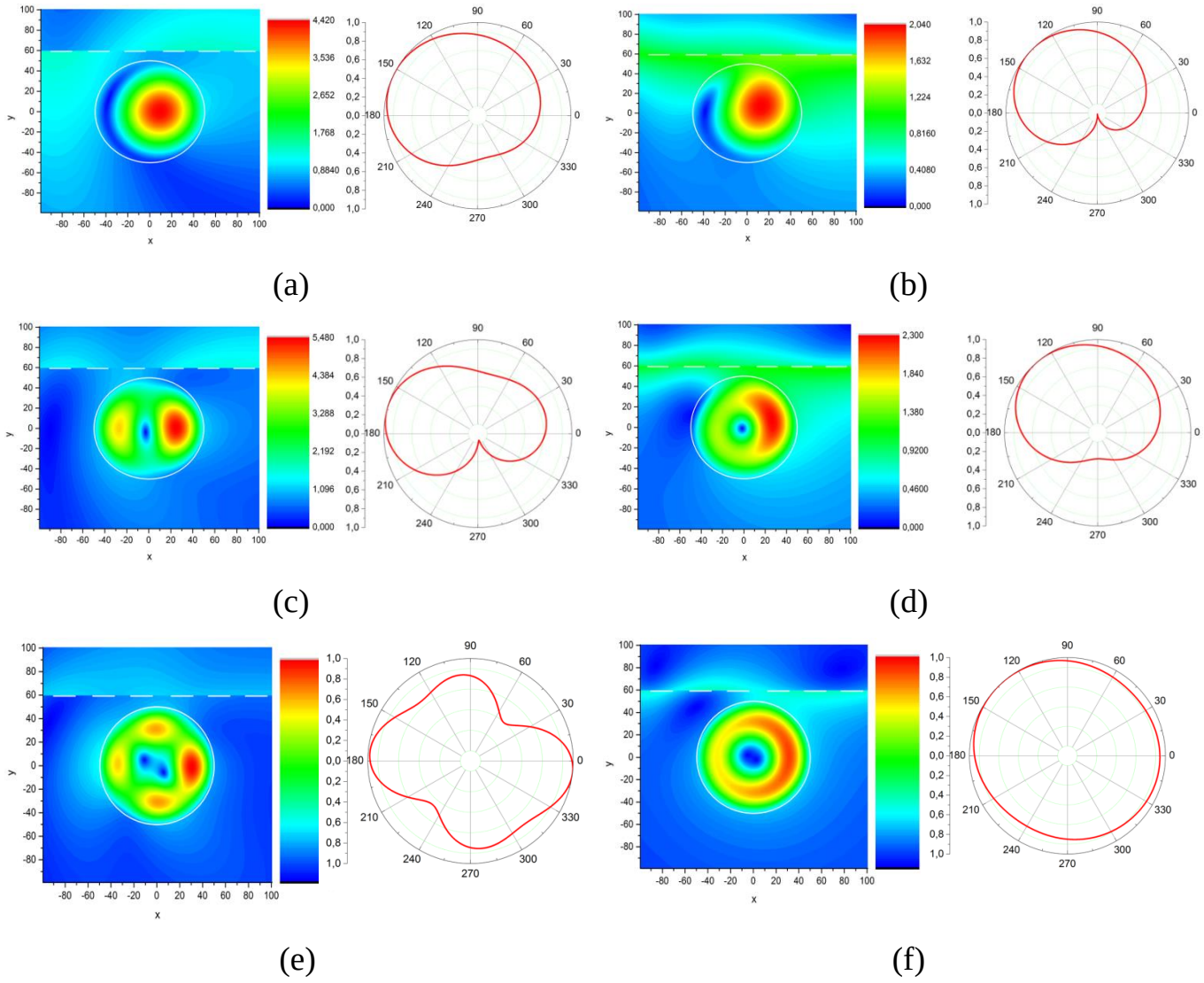

Fig. 2.6 Total near magnetic field patterns (left panels) and normalized far-field scattering patterns (right panels) of the lossless silicon nanowire of the radius a = 50 nm and $\beta = 0.9$ (a,c,e), $\beta = 0.5$ (b,d,f) in the resonances on the modes H_{01} for $\lambda = 464$ nm (a,b), H_{11} at $\lambda = 306$ nm (c,d) and H_{21} at $\lambda = 225$ nm (e,f)

Therefore, at the resonance wavelengths, the beam field excites not a single one of two degenerate modes $H_{m,n}$ ($m > 0$) but the both, and the contribution of the anti-symmetric with respect to $y = 0$ component gets larger with smaller β. This leads to the overlap of two modal patterns so that the resulting field portrait (in absolute value)

resembles a continuous ring. The reason is that if $\beta << 1$ (non-relativistic beam) then $B_m^{\pm}(\beta) = \pm(2/\beta)^m \left[1 + O(\beta^2)\right]$. Hence the inner field pattern takes the form of the rotating wave, $J_m(k\alpha r)(\cos m\varphi - i \sin m\varphi) + O(\beta)$, instead of the standing-wave $J_m(k\alpha r)\cos m\varphi$, observed in the plane wave scattering. Note that this is not true for the resonance on the H_{01} mode (Fig. 2.6 a, b) because in this case the contribution of anti-symmetric field component is zero.

This feature is also well visible in the far zone, where the normalized by the maximum value angular scattering patterns are shown in Figs. 2.6 at the same wavelengths. If $\beta << 1$, then the in-resonance radiation becomes omnidirectional.

2.4 Two dielectric nanowires as a model of beam position sensor

This section explores the opportunity of using the *Photonic Molecule* (PM) configuration and its DR characteristics for obtaining the information on the beam position shift *h*. Nanoscale size of such sensor antennas introduces negligible distortion to the beam energy characteristics, which can be considered as fixed. This makes possible the analysis of the beam position effect on DR in the same way as within the traditional electromagnetic theory, i.e. as the scattering of the given electromagnetic-wave field of the moving beam by the scatterers of given shapes and material properties. The latter parameters can be manipulated to optimize the BPM performance.

PMs are attracting the attention of researchers since the late 1990s as configurations occupying intermediate place between “photonic crystals” and “photonic atoms,” or stand-alone dielectric particles [119-124]. PMs are configured as finite number of similar or identical elements, usually having certain symmetry, say, a linear “chain” of them or a cyclic “necklace.” They confine light and enable its efficient manipulation at the micrometer length scale due to the strong optical coupling. This is an alternative to the manipulation of light in the photonic crystals which are the media with periodic variation of refractive index.

The simplest PM contains two identical spherical or circular-wire (Fig. 2.7) elements and hence it has two-fold symmetry. This circumstance leads to the appearance of four orthogonal families of natural modes of such a twin PM [121]. Here, each mode of PM is built on a certain mode of individual dielectric cavity, the cavities being optically coupled together in one of the four possible ways. Therefore, the coupled-cavity modes are called “supermodes.” Each family’s supermodes possess either symmetry or anti-symmetry of each field component with respect to each symmetry plane. This is usually expressed via the terms “bonding” and “anti-bonding” or “even” and “odd,” respectively.

Besides, the symmetry and anti-symmetry can be understood via the placement of the virtual perfect electrically conducting (PEC) or perfect magnetically conducting (PMC) wall along the corresponding symmetry plane. Under an external illumination, say, with a plane wave, PM supermodes can be either “bright” ones, that is, display resonances in the scattering and absorption, or remain “dark.” The latter happens if the incident field symmetry is different from the symmetry of the supermode natural field.

2.4.1 Problem formulation and basic equations

Consider a PM formed by two identical circular dielectric nanowires (#1 and #2) separated by the distance L between their axes, with the same radius a and refractive index $\alpha = \sqrt{\varepsilon}$ (ε being the relative dielectric permittivity). We assume that electron beam (1.1) moves between the wires in parallel to the x-axis at the distance h from it. Hence, the beam separation from the lower (upper) wire axis is $d = L/2 \pm h$. The Cartesian and the local and global polar coordinates are shown in Fig. 2.7.

The formulation of the 2-D boundary-value problem for the unknown scattered field involves the Helmholtz equation off the wire contours of cross-section, the penetrable-boundary conditions at these contours, the Sommerfeld radiation condition at infinity, and the condition of the local power finiteness. These conditions, which were detailed discussed in section 2.2, guarantee the solution uniqueness.

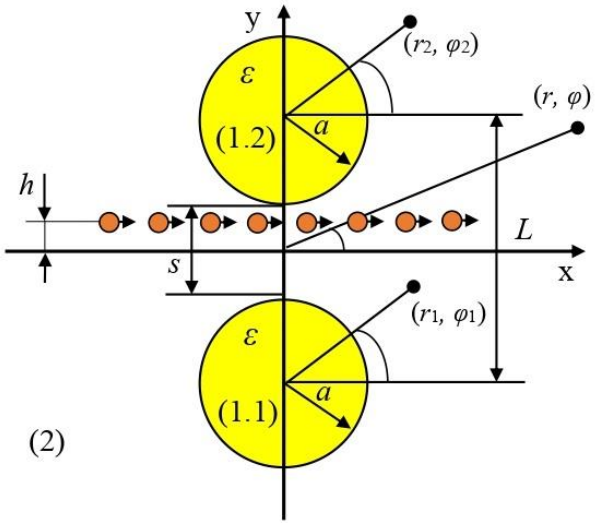

Fig. 2.7 Cross-sectional geometry of an electron beam moving between a pair of identical circular nanowires, which form a photonic molecule

The considered PM configuration has been studied in a number of publications, however, to the best of our knowledge, not with the electron-beam field (1.2) as a given excitation field. Here, the approximate numerical techniques like [125] and commercial FDTD-based codes [126] are important for engineering applications however not enough accurate if studying the fundamental wave effects such as sharp resonances. Therefore, we follow the semi-analytical technique first introduced by Twersky [78-81] and further improved in [121, 127, 128]. This technique exploits the circular shape of the boundaries of the wire cross-sections and combines the expansion of the field function in the azimuth Fourier series (in the local polar coordinates of each wire) with the addition theorems for the Bessel functions. It enables one to reduce the scattering problem to the infinite-matrix equation for the expansion coefficients. The important correction, introduced in [121, 127, 128], is the rescaling of that matrix equation to cast it to the Fredholm second-kind form. This correction guarantees the convergence of the numerical solution, in the mathematical sense.

Guided by these considerations, we expand the field in terms of the azimuth-

coordinate Fourier series inside each wire, $\vec{r} \in (1.p),\ p = 1,2$

$$H^{\text{int}(p)}(r_p, \varphi_p) = \sum_{m=-\infty}^{\infty} y_m^{(p)} J_m(k\alpha r_p) \exp(im\varphi_p),\ r_p < a,\ p = 1,2 \tag{2.31}$$

In the presence of the twin scatterers, the total field in the external domain, $\vec{r} \in (2)$, has the form of the sum,

$$H^{ext} = H^0 + H^{sc}, \tag{2.32}$$

$$H^{sc}(r, \varphi) = \sum_{p=1,2} \sum_{m=-\infty}^{+\infty} z_m^{(p)} H_m(kr_p) \exp(im\varphi_p),\ r_p > a, \tag{2.33}$$

where $J_m(\cdot)$ and $H_m(\cdot)$ are the Bessel and Hankel first-kind functions, and $(r_p, \varphi_p),\ p = 1,2$ are the local polar coordinates of the wires.

One of the boundary conditions requests the total field function H^{tot} to be continuous across each wire boundaries, $r_{1,2} = a$. On introducing the complex angles of incidence of the wave (1.2) below and above the beam trajectory, $\psi_{1,2}$, such that

$$\cos\psi_{1,2} = 1/\beta,\quad \sin\psi_{1,2} = \pm i\gamma/\beta, \tag{2.34}$$

and using the Jacobi-Anger formula in the complex domain, we can expand the incident field in terms of the azimuth series in the local coordinates of each wire as in [5],

$$H^0(r_{1,2}, \varphi_{1,2}) = \mp A\beta e^{-q(L/2 \pm h)} e^{ikr_{1,2}\cos(\varphi_1 - \psi_1)} = \mp A\beta e^{-q(L/2 \pm h)} \sum_{m=-\infty}^{+\infty} i^m J_m(kr_{1,2}) \left(\frac{1 \mp \gamma}{\beta} \right)^m e^{im\varphi_{1,2}}, \tag{2.35}$$

The expressions (2.31) and (2.33) satisfy the Helmholtz equation, the local power

finiteness condition, and the radiation condition.

For the twin PM configuration, the matrix equation (2.14) can be simplified to two coupled infinite-matrix equations as presented below,

$$x_m^{(1,2)} + \frac{V_m}{w_m D_m} \sum_{n=-\infty}^{+\infty} x_n^{(2,1)} w_n (\pm i)^{n-m} H_{m-n}(kL) = -\frac{F_m^{(1,2)}}{w_m D_m}, \tag{2.36}$$

where all notations correspond to Fig.2.7 and can be found in section 2.2.

Inspection of (2.36) shows that the diagonal matrix elements of its first (second) block characterize the scattering by, respectively, the first (second) wire in the free space, and the off-diagonal elements characterize the optical interaction. Note that the off-diagonal elements are not zero and hence the interaction is always present and decays rather slowly, as $O[1/(kL)^{1/2}]$ if $kL \to \infty$.

The obtained set (2.36) is a Fredholm second kind infinite-matrix equation (see [121, 127, 128]) due to the fact that $\sum_{m,n=-\infty}^{+\infty} \left| A_{mn}^{(1,2)} \right|^2 < \infty$ and $\sum_{m=-\infty}^{+\infty} \left| B_m^{(1,2)} \right|^2 < \infty$, where the matrix elements, $A_{mn}^{(1,2)}$, and the right-hand part elements, $B_m^{(1,2)}$, follow from (2.36). Then the Fredholm theorems guarantee that its numerical solution (after truncation to finite order *N*) converges to the exact solution. To obtain 5 correct digits in the near field, one has to take $N_{tr} \geq k\alpha a / \beta + 5$ (however, more if the airgap $L - 2a$ gets much smaller than *a*).

2.4.2 Scattering and absorption cross-sections

On using the large-argument asymptotic expressions for the Hankel functions, the scattered field in the far zone $(r \to \infty)$ takes the form of cylindrical wave, $H^{sc}(r, \varphi) = (2/i\pi kr)^{1/2} \Phi(\varphi) \exp(ikr)$, where the far-field angular scattering pattern depends on the coefficients $x_n^{(p)} = z_n^{(p)} w_n$, and $w_{n<0} = (-1)^n w_{n>0}$, $w_{n>0} = n!(2/ka)^n$,

$$\Phi(\varphi)=\Phi_1(\varphi)+\Phi_2(\varphi),\quad \Phi_{1,2}(\varphi)=\exp(\mp\tfrac{1}{2}ikL\sin\varphi)\sum_{m=-\infty}^{+\infty}(-i)^m w_n z_m^{(1,2)}\exp(im\varphi), \qquad (2.37)$$

Then the total scattering cross-section is found as (1.8). If the dielectric wires are lossy, then, besides the scattering, a part of the power of the incident field is absorbed in PM. This is characterized by the absorption cross-section (ACS), which is found from the integration of the normal component of the time-averaged Poynting vector over the contours of the wires. This leads to the following equation:

$$\sigma_{abs}=\frac{2\pi a}{|\alpha|^2 A^2\beta^2}\sum_{m=-\infty}^{\infty}\left(|y_m^{(1)}|^2+|y_m^{(2)}|^2\right)\mathrm{Im}\left[\alpha J_m(k\alpha a)J_m'(k\alpha^* a)\right], \qquad (2.38)$$

where * means the complex conjugation. The unknowns $y_m^{(1,2)}$ are as follows

$$y_m^{(1,2)}J_n(k\alpha a)=z_m^{(1,2)}H_m(ka)+\sum_{n=-\infty}^{+\infty}(\mp i)^{(n-m)}z_n^{(2,1)}J_n(ka)H_{m-n}(kL)+f_m^{(1,2)} \qquad (2.39)$$

Thus, on solving the matrix equation (2.36) truncated to finite order N_{tr}, one can calculate the scattering and absorption cross-sections and the near and far field patterns. Note that the accuracy of the calculation of the near field and hence the ACS is the same as accuracy of solving (2.36). However, the accuracy of calculation of the far-field angular pattern (2.37) and the TSCS (1.8) is approximately by an order of magnitude better because of the presence of the Bessel functions, which decay exponentially with *n* if $n > ka$.

2.4.3 Modified Optical Theorem

The sum of SCS and ACS is called the extinction cross-section [19]. Thanks to

the Complex Poynting Theorem applied to the total field function and its complex conjugate, the extinction of the considered PM scatterer can be connected to the far-field values in certain complex directions.

Here, unlike the single-wire configuration of section 2.3, we have the scatterers both above and below the beam trajectory. Therefore, it is necessary to introduce two complex-valued angles of incidence of the wave (1.2) in the upper and lower half-spaces, $\psi_{1,2}$, respectively - see (2.34).

Then, the real part of the expression, which follows from the Complex Poynting Theorem reduces (see section 1.4) modifies to

$$\sigma_{sc} + \sigma_{abs} = -\frac{4}{kA\beta}\,\mathrm{Re}\left[\Phi_1(\psi_1) + \Phi_2(\psi_2)\right], \tag{2.40}$$

or, with account of (2.37),

$$\sigma_{sc} + \sigma_{abs} = -\frac{4}{kA\beta} e^{-qL/2}\,\mathrm{Re}\sum_{m=-\infty}^{+\infty}(-i^m) w_n \left[z_m^{(1)} e^{-qh}\left(\frac{1-\gamma}{\beta}\right)^m + z_m^{(2)} e^{qh}\left(\frac{1+\gamma}{\beta}\right)^m \right]. \tag{2.41}$$

The obtained expression plays the role of the Optical Theorem (OT) for the diffraction radiation excited by the electron beam (1.1) flowing between the wires of a twin-wire PM. If the TSCS value has been found, then the ACS value can be determined from (2.41) instead of (2.38). Comparison of two values of ACS, found from (2.38) and (2.41), can be viewed as a partial validation of the solution correctness. Still, their coincidence is only a necessary condition of correctness however not a sufficient one. The sufficient test is provided by the verification of the fulfillment of the boundary conditions.

In our work, the Optical Theorem (OT) has been satisfied at the level of machine precision and the boundary conditions have been satisfied with the same accuracy as the

solution of the matrix equation (2.36), controlled by the truncation order N_{tr}. Additional validation has been provided by the fact that if the relative dielectric permittivity of the wire #2 is set to be 1, then the computed TSCS and ACS are the same as for a single dielectric wire excited by the beam (1.1), where the full-wave analytical solution is available [8], see also section 2.2.

2.4.4 Numerical results: resonances on the dimer supermodes

In computations, we have been looking for the features of the DR associated with twin-cavity PM configuration that can be used for the detection of the shift of the beam trajectory from central position between the dielectric wires. We are also interested in seeing the effect of the relative beam velocity, β, on the DR.

Here, we remind that the modes of twin-wire PM (Fig. 2.6) are "supermodes" built on the natural modes of each separate circular wire and optically coupled in four possible ways because of the two-fold symmetry. Therefore, they are classified usually as "*x*-even, *y*-even" (EE), "*x*-even, *y*-odd" (EO), "*x*-odd, *y*-even" (OE), and "*x*-odd, *y*-odd" (OO). If the electron beam flows along the *x*-axis, i.e. exactly in the middle between the dielectric wires, so that $h = 0$, then its field (1.2) is anti-symmetric function of *y* with respect to $y = 0$. Such incident field is able to excite only the resonances on the modes of the (EO) and (OO) families, while the supermodes of the other two families, (EE) and (OE), remain "dark." The latter-mode resonances can be expected to start shining if the beam trajectory shifts from the central position, i.e. if $h \neq 0$. This effect can potentially serve as a marker for the beam position monitoring.

We start our numerical experiments from the PM made of two sub-wavelength wires with a = 50 nm, and $\varepsilon = 12$ ($\alpha = 3.4641$). Such a material is similar to silicon or GaAs that have very small losses in the visible range, so that, at first, we neglect them. The airgap between the wires is 20 nm. Fig. 2.8 demonstrates the dependences of the normalized total scattering cross-section (TSCS) on the beam modulation wavelength,

for one and two thin sub-wavelength nanowires with the beam shift $h = 0$ nm and several values of the beam velocity β. As already mentioned, stand-alone circular dielectric nanowire is a convenient reference scatterer, for which the DR problem can be solved analytically similarly to the plane-wave scattering - see section 2.3 for details.

For all β, the plots of TSCS show three distinctive peaks at λ = 225 nm, 306 nm, and 464 nm with smooth shapes. Intensity of DR decays if β gets smaller, i.e. for a non-relativistic beam, because its field (1.2) becomes compressed to the beam trajectory. The resonance peaks are broad that tells that the corresponding natural modes have small Q-factors. This is apparently the reason that no splitting into doublets of the (EO) and (OO) supermodes is visible, so that each peak is a collective resonance on both of them.

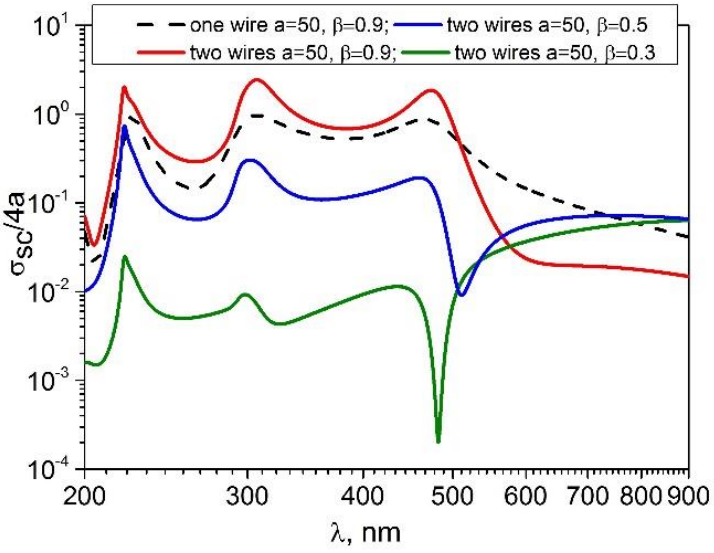

Fig. 2.8 Normalized TSCS of the 50-nm in radius one (dashed curve) and two silicon nanowires versus the wavelength in the visible range, for several values of the electron relative velocity β. The beam flows along the *x*-axis ($h = 0$)

Moreover, if the beam trajectory is shifted from the *x*-axis, these peaks do not split further, again because of the low Q-factors of the (EE) and (OE) supermodes, which are “dark” if $h = 0$ but should become “bright” if $h \neq 0$. This gives an idea that

too thin dielectric wires, even if made from nigh refractive index material, are not a promising configuration for the beam-diagnostics applications.

Therefore, in Fig. 2.9 (a) we demonstrate the wavelength scans of TSCS for much thicker silicon nanowire PM with a = 200 nm and the same airgap of 20 nm. As one can see, in this case there are multiple resonances within the visible range (i.e. for λ from 300 nm to 800 nm). A zoom of the part of the spectrum near to 360 nm is shown in Fig. 2.9 (b) for the beam velocity $\beta = 0.5$ and two beam shifts, and $h = 5$ nm. Now, the splitting of the resonance peaks is clearly visible.

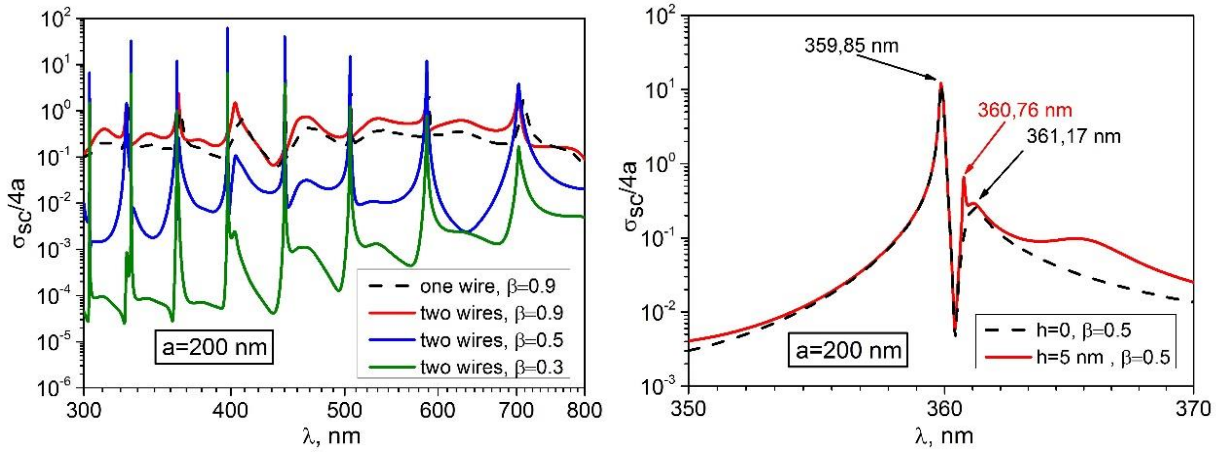

(a) (b)

Fig. 2.9 The same as in Fig. 2.8 however for one (dashed curves) and two (solid curves) silicon nanowires of the 200-nm radius (a) and a zoom of the TSCS spectra for in the wavelengths range from 350 nm to 370 nm (b)

According to [121], the quartets of WG supermodes actually form two tight doublets: one of the (OO) and (EO) families of modes and another of the (EO) and (EE) families. Close inspection shows that the complex poles underlying the higher-Q peak of TSCS for $h = 0$ at the wavelengths of 359.85 nm in Fig. 2.9 (b), correspond to the supermode $H_{8,1}^{OO}$ and apparently not resolved sister-mode $H_{8,1}^{EO}$. Similarly to that, a broader peak at 361.17 nm corresponds to the lower-Q supermode $H_{7,2}^{OO}$ and its not

resolved sister-mode $H_{7,2}^{EO}$. This interpretation is fully supported by the in-resonance normalized far-field angular patterns and the near-field patterns shown in Figs. 2.10 and 2.11, respectively, for the symmetric excitation of twin-wire PM ($h=0$). The beam trajectory is indicated by the dashed line. In each peak, the supermodes of the (OO) family dominate in the total field.

(a) 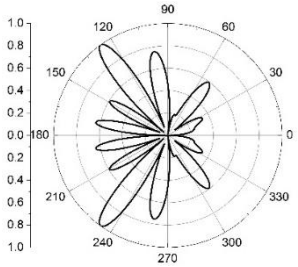 (b) 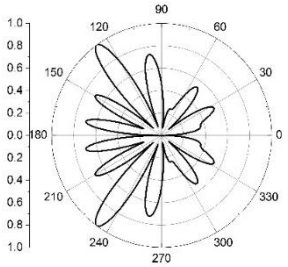

Fig. 2.10 Symmetric beam excitation. In-resonances normalized far-field scattering patterns of twin silicon nanowires of the radius a = 200 nm, L = 120 nm, $h=0$ and β=0.5 at λ = 359.85 nm (a) and 361.17 nm (b).

(a) $H_{8,1}^{OO}$ 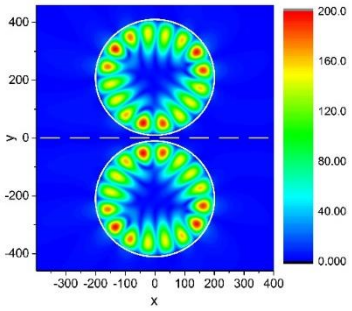 (b) $H_{7,2}^{OO}$ 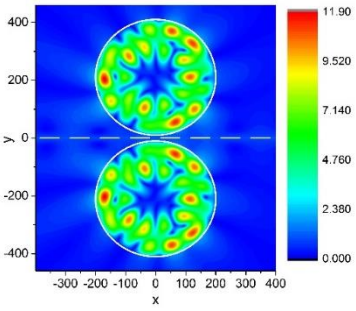

Fig. 2.11 Symmetric beam excitation. In-resonances near field patterns of twin silicon nanowires of the same parameters as in Fig.2.10

What is most important from the viewpoint of applications in BPM design, if the beam trajectory is shifted from the *x*-axis, then new additional peaks of TSCS appear. This is visible on the zoomed spectrum shown in Fig. 2.9 (b) for h = 5 nm: an additional sharper peak starts shining at 360.76 nm and a broad peak appears at 365.5 nm. The

corresponding in-resonance far-field angular patterns and the total near-field patterns are depicted in Fig. 2.12 and Fig. 2.13, respectively.

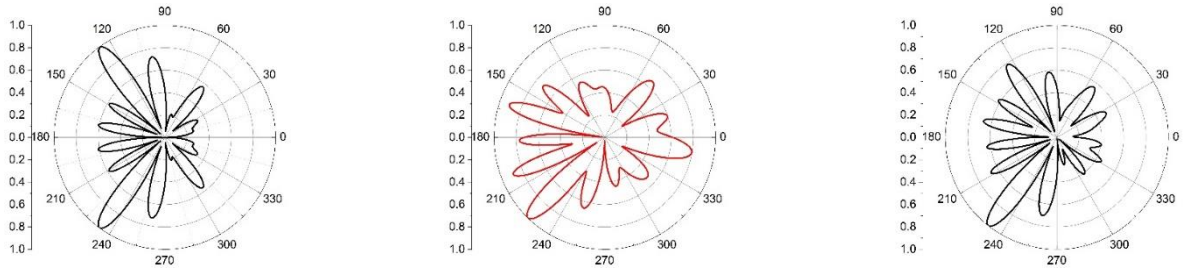

(a) (b) (c)

Fig. 2.12 Non-symmetric beam excitation. The same as in Fig. 2.10 for a = 200 nm, L = 420 nm, h = 5 nm, β= 0.5 at λ = 359.85 nm (a), 360.76 nm (b), and 361.17 nm (c)

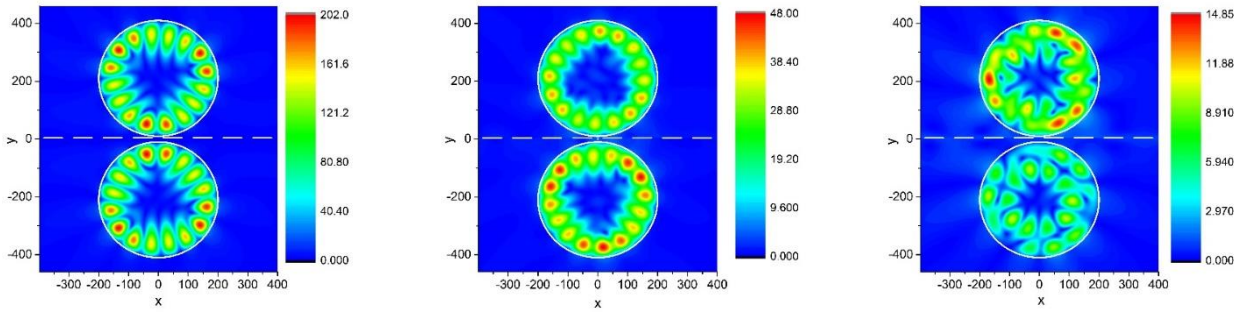

(a) (b) (c)

Fig. 2.13 Non-symmetric beam excitation. In-resonances near field patterns of twin silicon nanowires of the same parameters as in Fig.2.12

Note that the pattern in Fig. 2.12 (a) is very close to the pattern in Fig. 2.10 (a) and that in Fig. 2.13 (a) – to the one in Fig. 2.11 (a). The same is visible for the patterns shown on the panels (c) of Fig. 2.12 and Fig. 2.13 and panels (b) of Fig. 2.10 and Fig. 2.11, respectively. This leads to the conclusion that the supermodes with the fields, anti-symmetric with respect to y, are weakly sensitive to the shift h of the beam trajectory. The explanation of this property can be seen in the fact that these modes have zero

values of their H-fields on the *x*-axis and hence it is much better compatible with the incident field (1.2) than of the *y*–even mode families.

In contrast, the patterns shown in Fig. 2.12 (b) and Fig. 2.13 (b) correspond to the new resonance at 360.76 nm, which is absent if $h = 0$. They demonstrate that this is the resonance on the WG supermode $H_{8,1}^{EO}$, with some admixture of its not resolved sister-mode $H_{8,1}^{EE}$, which has smaller contribution. Similar conclusions can be reached for the broad peak at 365.5 nm, not existent at $h = 0$.

To strengthen these conclusions, we have computed the TSCS spectra for the symmetric and shifted beam excitation of the twin-wire PM with even larger however still nanoscale silicon resonators, of the 400-nm radius. The corresponding plots are presented in Fig. 2.14 (a) for $\beta = 0.5$ and the shift values h = 0 and h = 5 nm in the range of wavelengths between 400 nm and 500 nm, and a zoom around 423 nm is shown in Fig. 2.14 (b). Like in the previous example, the TSCS of the PM excited by symmetrically flowing beam demonstrates two resonance peaks, while the non-symmetrically excited PM – four resonance peaks.

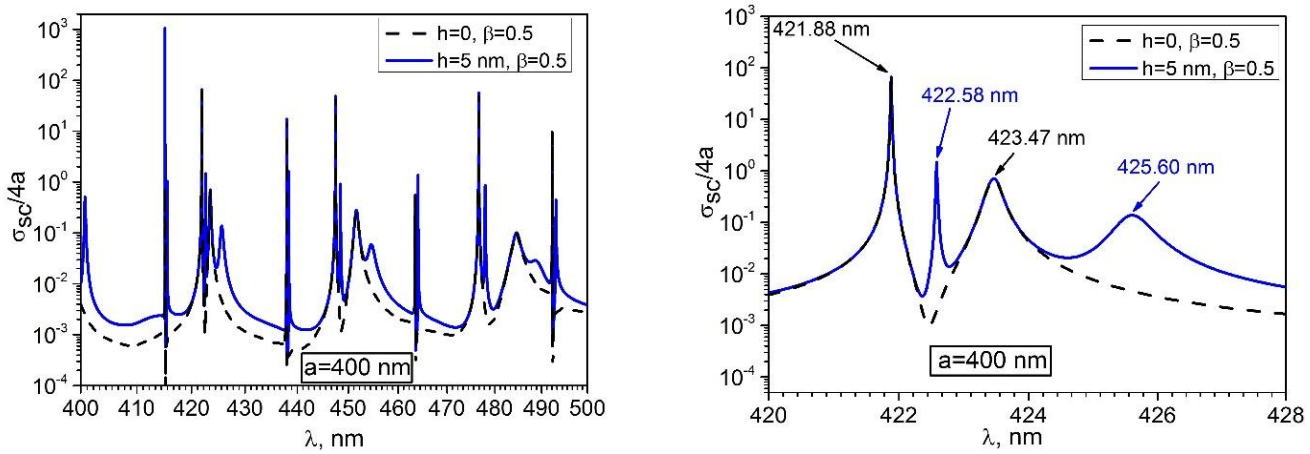

(a) (b)

Fig. 2.14 Normalized TSCS of PM on twin silicon nanowires of 400-nm radius with 20-nm airgap versus the wavelength, for the electron relative velocity β = 0.5 and two values of the shift distance h (a) and its zoom (b)

As we could already see, reliable interpretation of the resonances is best achieved via visualizing the near-field patterns. The four in-resonance field patterns corresponding to the four peaks of TSCS in Fig. 2.14 (b) for the beam shifted by h = 5 nm are presented in Fig. 2.15.

They demonstrate convincingly the fields dominated by the higher-Q supermodes $H_{12,2}^{OO}$ at 421.9 nm and $H_{12,2}^{OE}$ at 422.6 nm in the sharp peaks of TSCS, and the lower-Q supermodes $H_{9,3}^{OO}$ at 423.5 nm and $H_{9,3}^{OE}$ at 425.6 nm - in the broader peaks of TSCS. In each case, the pattern is slightly distorted by the presence of not fully resolved sister-supermode of the x–even family. Here, similarly to the previous example with 200-nm in radius twin-wire PM, the appearance of the peaks on the y-even modes $H_{12,2}^{OE}$ and $H_{9,3}^{OE}$ can serve as a marker of the beam deviation from the center of the 20-nm airgap.

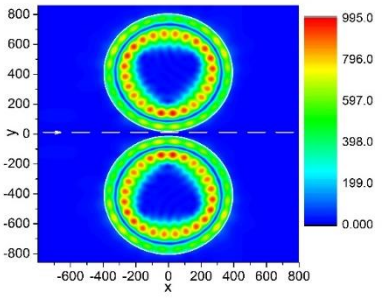

(a) $H_{12,2}^{OO}$

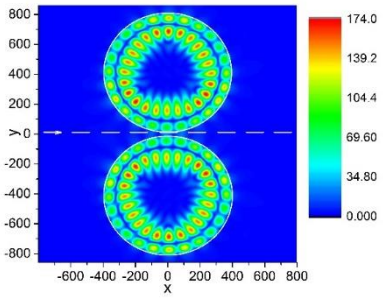

(b) $H_{12,2}^{OE}$

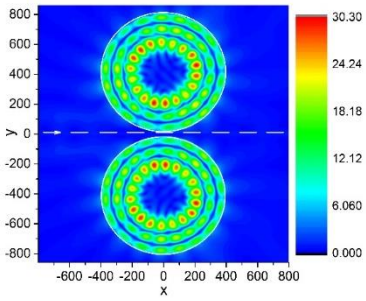

(c) $H_{9,3}^{OO}$

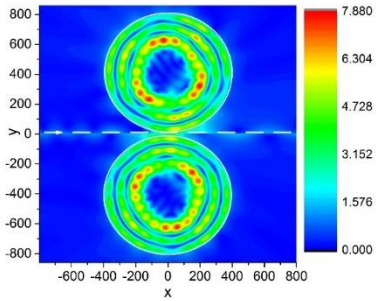

(d) $H_{9,3}^{OE}$

Fig. 2.15 Non-symmetric excitation. In-resonances near field patterns of twin silicon nanowires of the radius a = 400 nm, L = 820 nm, s= 20 nm, h = 5 nm and β= 0.5 at λ = 421.88 (a), 422.58 (b), 423.47 (c) and 425.60 nm (d)

Next, we analyze in greater details the sharper peaks of TSCS in Fig. 2.14 (a), near to the wavelength of 415 nm. The corresponding zoom is shown in Fig. 2.16 for the shifted by 5 nm and not shifted trajectories of the electron beam with β = 0.5. Similarly to the previous analysis, the sharper peak on the $H_{16,1}^{OO}$ WG supermode at λ = 415.1219 nm is present in both cases and keeps the same shape, and the other peak on the $H_{16,1}^{OE}$ supermode at 415.489 nm appears only if the beam trajectory is shifted.

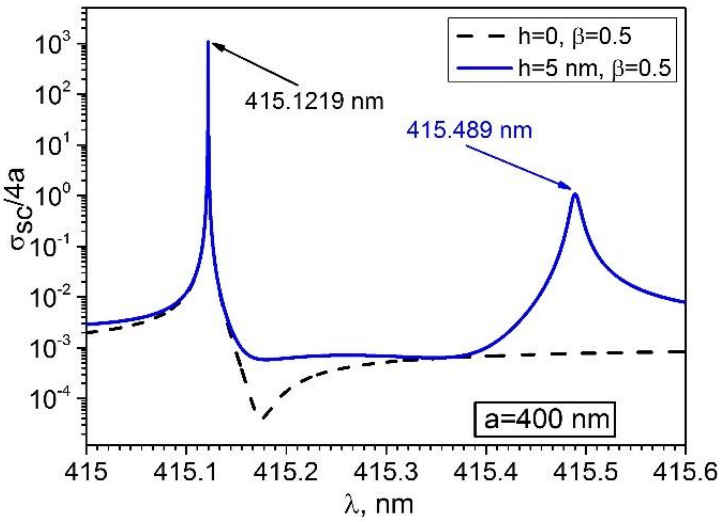

Fig. 2.16 Zoom of TSCS curves from Fig. 2.14(b) between λ = 415 - 415.6 nm

(a) $H_{16,1}^{OO}$ (b) $H_{16,1}^{OE}$

Fig. 2.17 Non-symmetric excitation. In-resonances near field patterns of twin silicon nanowires of the radius a = 400 nm, L = 820 nm, s= 20 nm, h = 5 nm and β= 0.5 at λ = 415.1219 nm (a), 415.489 nm (b)

The WG supermode type identification is based on the visualization of the near field patterns in these two resonances, presented in Fig. 2.17. Thus, the resonances on the supermodes, which have only one field variation in radius, serve as even better marker of the beam trajectory deviation from the central (symmetrical) position, because of the higher Q-factors.

So far, we have been discussing the numerical results computed with the lossless dielectric cavities. In order to obtain a vision of the role played by the losses, now we introduce small bulk material losses, $\mathrm{Im}\,\varepsilon$, in the 400-nm in radius wires and compute the ACS as a function of the wavelength – see Fig. 2.18. The PM and the electron-beam parameters are taken the same as in Fig. 2.14 (b).

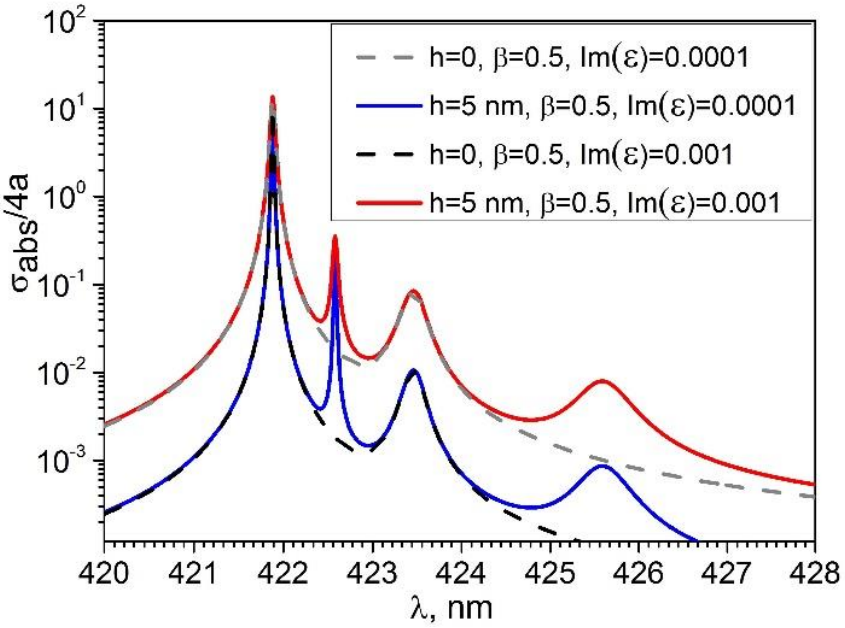

Fig. 2.18 Normalized ACS of PM on twin silicon nanowires of 400-nm radius with 20-nm airgap versus the wavelength, for the electron relative velocity β = 0.5 and two values of the shift distance *h*

As one can see, the ACS spectra show the resonance peaks at the same wavelengths as on the plots of TSCS, which are not shown here because for so small bulk losses they overlap with the curves in Fig. 2.14 (b). The maximum value of the

absorption is achieved in the resonance on the most high-Q mode, $H_{12,2}^{oo}$, however it is still by the order of magnitude lower than the resonance scattering (compare with Fig. 2.14 (b)). Similarly to the scattering, two additional peaks of absorption appear if the beam trajectory deviates from the airgap center, on the *y*-even modes $H_{12,2}^{oe}$ and $H_{9,3}^{oe}$. If the bulk losses in the dielectric material are taken 10 times greater, 10^{-3} instead of 10^{-4}, then the ACS curves also rise by approximately an order, except of the high-Q resonances where this rise is cancelled by the Q-factor, which in this case is inverse proportional to the bulk losses.

Conclusions to Chapter 2

In this section, the DR-caused scattering and absorption characteristics of a modulated beam of particles in the visible range have been considered. For one wire we have used analytical solution obtained by the separation of variables. For twin wires configuration (also known as photonic molecule or dimer), a numerical-analytical method with guaranteed convergence has been developed and used. Implementing these reliable computational tools, resonances in the DR characteristics, such as scattering and absorption cross sections, have been investigated and discussed. According to the results of the performed research, it is possible to draw the following conclusions:

- If one can neglect the action of the field on the electrons, then the EM field of a modulated 2-D beam takes form of a surface slow wave propagating along the beam trajectory. This wave induces the polarization and surface currents on the local obstacles and hence a radiation occurs even if the beam does not touch the obstacle. In fact, the wire plays the role of optical nanoantenna, which makes the beam of particles visible. As we have shown, a nanowire behaves as an open resonator, thanks to which the radiated power is enhanced near the natural-mode wavelengths.
- For the single dielectric nanowire, unlike the more conventional plane-wave scattering, the in-resonance fields (except of the H_{01} mode) are shaped as rotating

cylindrical waves. This happens because of three circumstances: (I) the beam field depends on *y*, and hence there are no “dark modes” of the wire that remain not excited because of orthogonal symmetry with respect to the incident wave, (II) the symmetric and the anti-symmetric natural modes of the wire remain degenerate, and (III) if $\beta \to 0$, then the phase shift between these mode contributions approaches $\pi / 2$.

- A PM formed by a pair of identical nanowires made of high refractive index dielectric material behaves as a composite optical open resonator, which supports quartets of supermodes built on the natural modes of each cavity, combined together according to the two-fold symmetry of this configuration. If the electron beam flows between the wires, the emerging DR is resonantly enhanced near each natural WG supermode wavelength. As we have found, if the beam trajectory shifts away from the central (i.e. symmetrical) position, then new peaks in the spectra of the scattering become visible. They appear due to the resonances on the formerly “dark” WG supermodes, which are absent in the symmetric beam excitation. This effect can be important for applications related to the design of novel optical-range BPMs. It is interesting to question the feasibility of experimental verification of the presented effects. Today the size of controllably manufactured subwavelength dielectric microcavities is measured in hundreds and dozens of nanometers. So, in principle, experimental verification is realistic. Besides, the DR a dielectric resonator with a fixed relative permittivity can be scaled up to larger sizes and wavelengths. For example, the curves presented in Figs. 2.13 to 2.16 for the wire radius 400 nm and the wavelengths of 400 nm to 500 nm are equally valid for the wire radius 4 mm and the wavelengths of 4 mm to 5 mm.

CHAPTER 3 DIFFRACTION RADIATION OF A BEAM OF PARTICLES MOVING NEAR SILVER NANOWIRES

In this chapter, the DR-caused scattering and absorption characteristics in the visible range are numerically investigated for a stand-alone circular silver nanowire and twin circular silver nanowires and nanotubes. These configurations are investigated keeping in mind the BPM applications. The wavelength-dependent permittivity of silver is taken from the experimental data and shows negative real-part values. Thanks to this, sub-wavelength in radius silver nanowires are famous as nanoresonators due to the *localized surface-plasmon* (LSP) modes. Similar to Chapter 2, we use the field expansions in the azimuthal Fourier series and the addition theorems for the cylindrical functions. This enables us to solve one-wire problem analytically and reduce it to a Fredholm second kind infinite-matrix equation for silver-wire and silver-tube dimers. Here the Fredholm theorems guarantee convergence of numerical solutions. Truncating this matrix, we compute the near and far field patterns of the wires as optically coupled plasmonic resonators and analyze dependence of the near and far-field spectral characteristics on the wavelength and electron beam parameters. The materials of Chapter 3 are published in works [A3, A4, A6, A15-17, A22-24].

3.1 Single silver circular nanowire: resonances on the plasmon modes

We study the DR characteristics of the charged particles beam (1.1) moving near a circular metal (silver) nanowire. All basic equations are similar to the dielectric single wire case presented in section 2.3, the difference being in the complex permittivity of the silver material. The complex-valued bulk dielectric permittivity of silver has been taken from the experimental paper of Johnson and Christy [93] and combined with a cubic spline interpolation as it was explained in section 1.3. Note that the plane-wave scattering from stand-alone and twin-wire plasmonic scatterers was extensively studied in the past [134-136], however, the DR effect has not been studied. In computations, the

associated series or matrix equations have been truncated at the number ±10 that well exceeds the maximum value of $ka|\alpha|\beta^{-1}$ in the whole optical range and provides 4 and more correct digits.

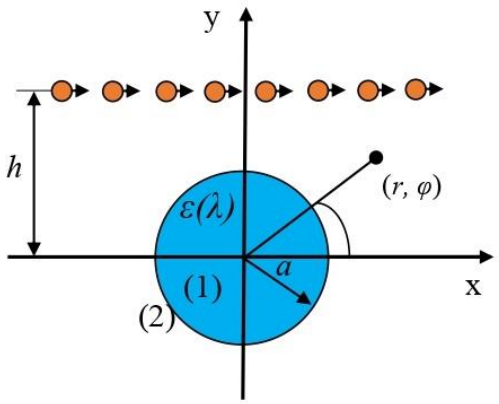

Fig. 3.1 Cross-sectional geometry of an electron beam moving near a stand-alone circular silver nanowire

Note that the silver nanowire's dielectric function varies between 0.93 (at λ = 306 nm) and -40 in the visible range and that the losses are quite considerable, between 0.2 and 3.9 – see Fig.1.2.

The plots in Fig. 3.2 demonstrate the dependences of the normalized TSCS and ACS on the modulation wavelength in the visible range, for the wire with the radius 50 nm, the impact parameter h = 60 nm, and several values of the relative beam velocity β. For all β, the plots of TSCS show the maximum at λ = 347 nm preceded by the minimum at λ = 318 nm and the plots of ACS – the peak at λ = 343 nm. Note that ACS is quite comparable with TSCS, especially in the blue and violet parts of the spectrum.

As expected, the wavelengths of the peak scattering and peak absorption are very close to the root of the "textbook" quasi-static equation, $\mathrm{Re}\,\varepsilon(\lambda) = -1$ [19,95], found at λ = 338 nm [93]. This is a collective resonance caused by the infinite number (m = 1,2,…) of the transverse LSP modes of a circular wire with negative dielectric

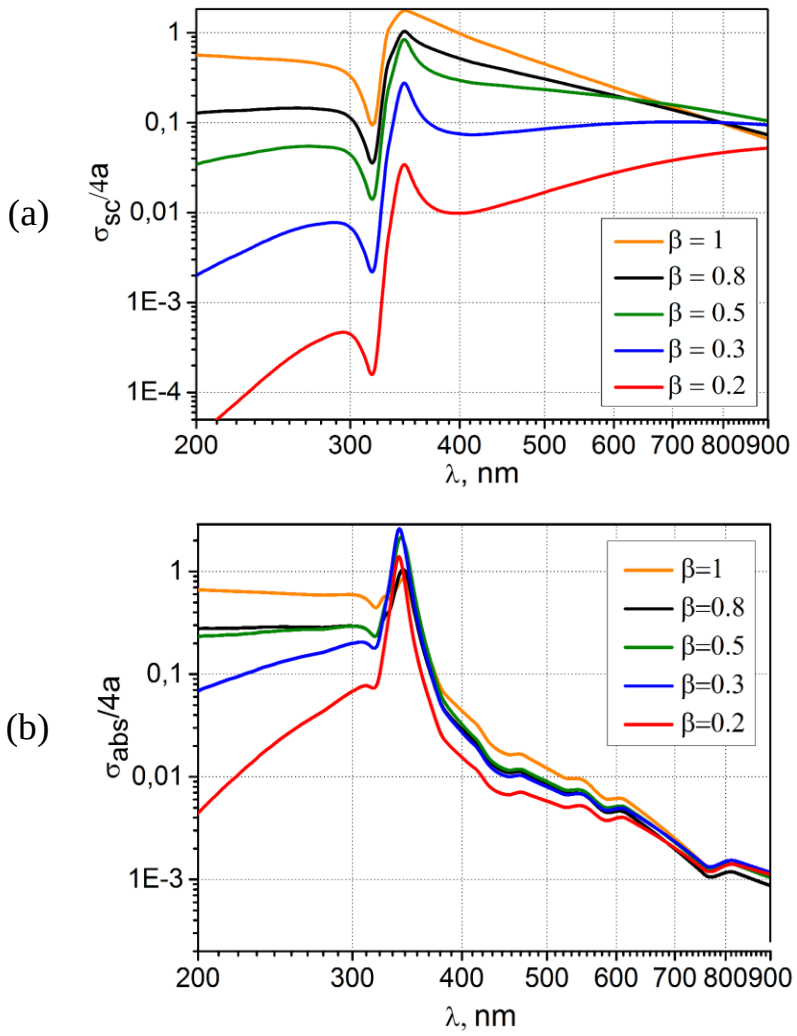

Fig. 3.2 Normalized TSCS (a) and ACS (b) of the 50-nm silver nanowire versus the wavelength in the visible range, for several values of the electron relative velocity β

function. This happens because, if $a/\lambda \to 0$, then the corresponding characteristic equation (2.27) takes form as $D_m(\lambda) \approx \varepsilon(\lambda) + 1 + O(m^{-1}a^2\lambda^{-2})$ [95], which is asymptotically independent of the azimuth index m. The peaks of separate LSP resonances merge together because of the losses in silver.

The minimum of TSCS (and to lesser extent of ACS) is typical for the plasmonic scatterers, see [27, 99, 129]. Its location in wavelength corresponds to the value, at which the dielectric function of silver, $\mathrm{Re}\,\varepsilon(\lambda) = 1$, comes near to 1. Here, the metal placed in the vacuum becomes optically transparent although still not invisible due to

non-zero absorption. According to experimental measurements [93], that happens at λ = 308 nm, and the red shift of the minimum in Fig. 3.2 is the effect of the finite wire radius. As can be found after inspection of the works [127, 128, 130, 131], this "invisibility" effect is equally well observable in the scattering of light by finite and infinite arrays of circular silver nanowires. Potentially such optical transparency can be also useful in the design of beam velocity sensors, because the depth of the minimum depends of that velocity.

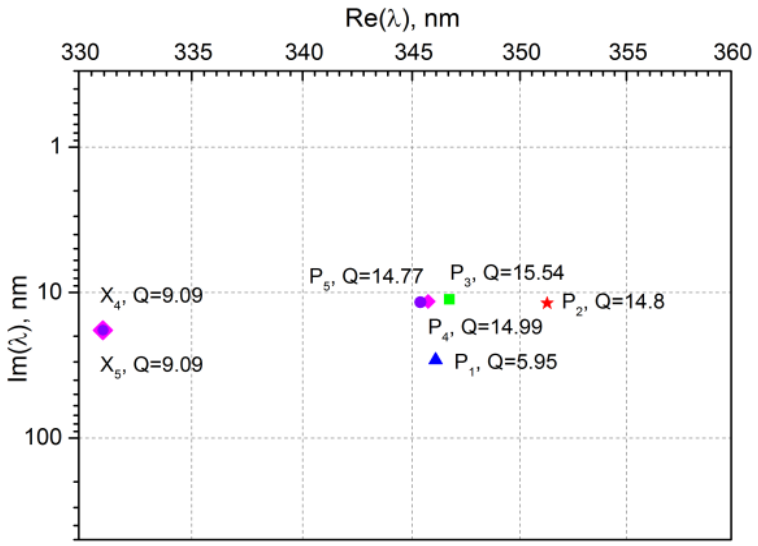

Fig. 3.3 Complex eigenvalues of the silver nanowire in the visible range

To clarify the nature of the peak of TSCS, we have calculated the complex eigenvalues of the silver nanowire using the rigorous characteristic equations (2.26). Here, Johnson and Christy data for $\varepsilon(\lambda)$ cannot be used directly because they were measured for the real frequencies. To overcome this difficulty, we have used the modified "Drude + two Lorentzians" formula presented in [132] that provides reasonably good approximation of the measured data in the range between 200 nm and 400 nm, and continued it to the complex frequencies.

The results are presented in Fig. 3.3. As expected, for all m the complex eigen-wavelengths are located close to each other between 330 nm and 360 nm and have

comparable imaginary parts of λ. Their Q-factors are between 5 and 15. They correspond to the LSP modes of the metal wire from P_1 to P_5. The notations X_4 and X_5 correspond to the so-called secondary plasmon modes, the existence of which was apparently mentioned first time in [95]. They have comparable Q-factors however produce no separate peaks in the spectra of TSCS and ACS. The near field patterns of the plasmon modes P_1 to P_5 are presented in Fig. 3.4.

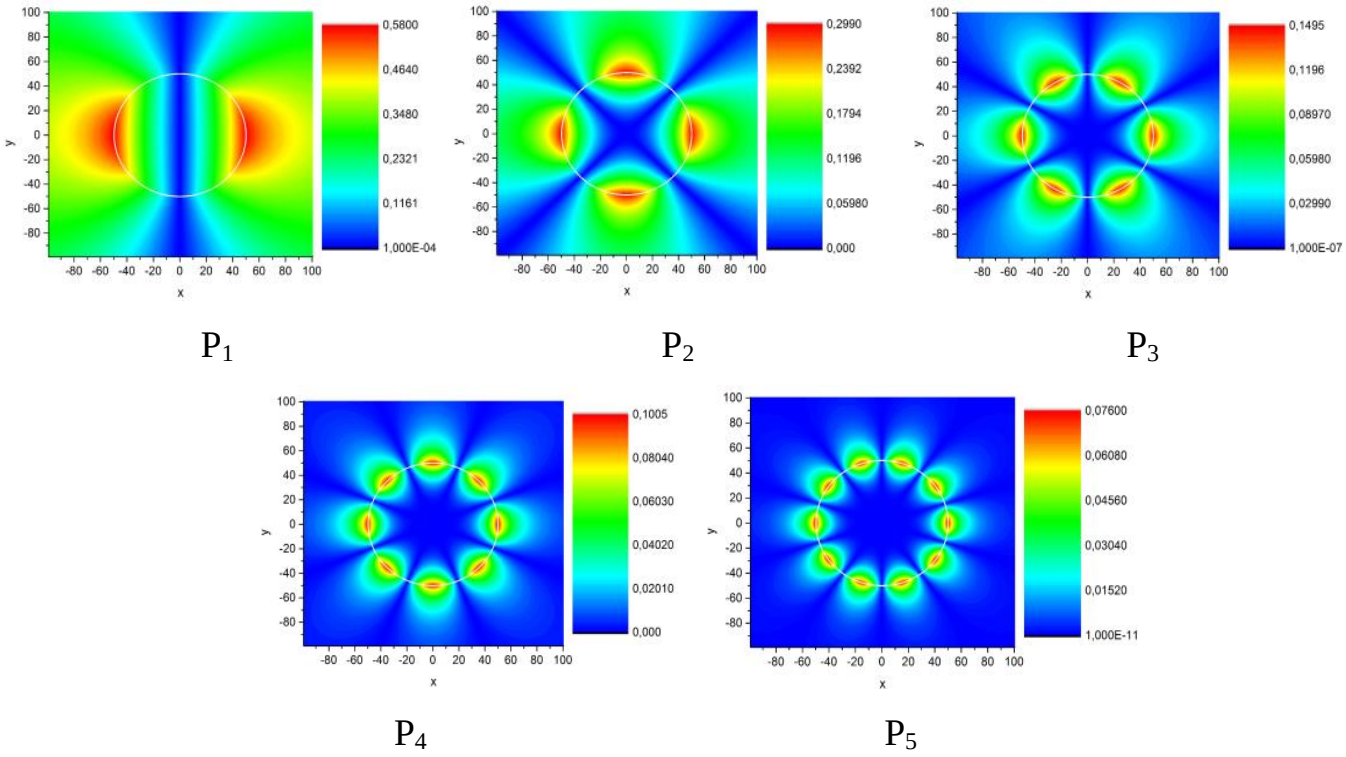

Fig. 3.4 Near field patterns of the lowest-order plasmon modes of silver nanowire with the wavelengths between 330 nm and 350 nm

We have also computed the total near magnetic field patterns and the normalized DR far-field angular scattering patterns of the same silver nanowire excited by the beam of particles (1.1), at the fixed values of β and λ. As one can see in Fig. 3.5, at the resonance wavelengths the total field is dominated by the mentioned composition of many plasmon modes. Its bright spots are located near the surface of the nanowire and do not penetrate into it. This is explained by the surface nature of the plasmon modes.

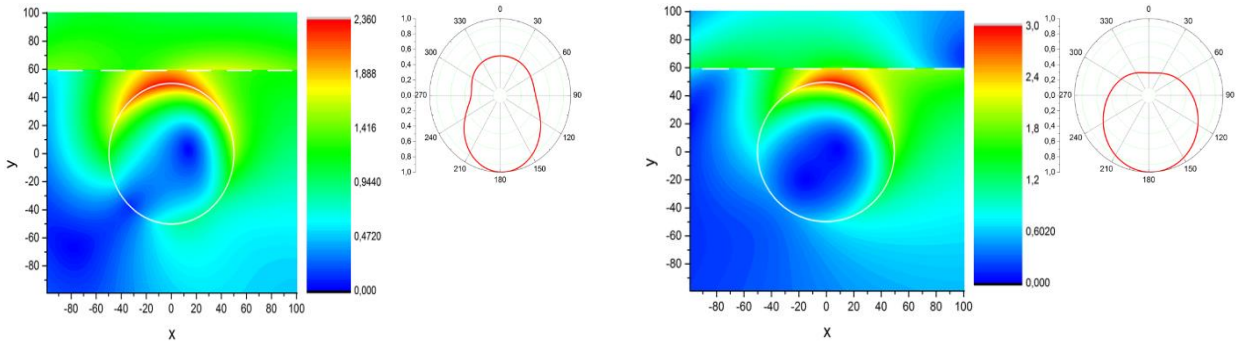

(a) (b)

Fig. 3.5 Near magnetic field patterns (left) and normalized far-field scattering pattern (right) of the silver nanowire of the radius a = 50 nm for and β =0.8 (a), β =0.5 (b) in the collective LSP resonance at λ = 347 nm

At the “invisibility wavelength” of λ = 318 nm, the total field in the near zone shows the beam field (1.2) only slightly perturbed by the wire – see Fig. 3.6

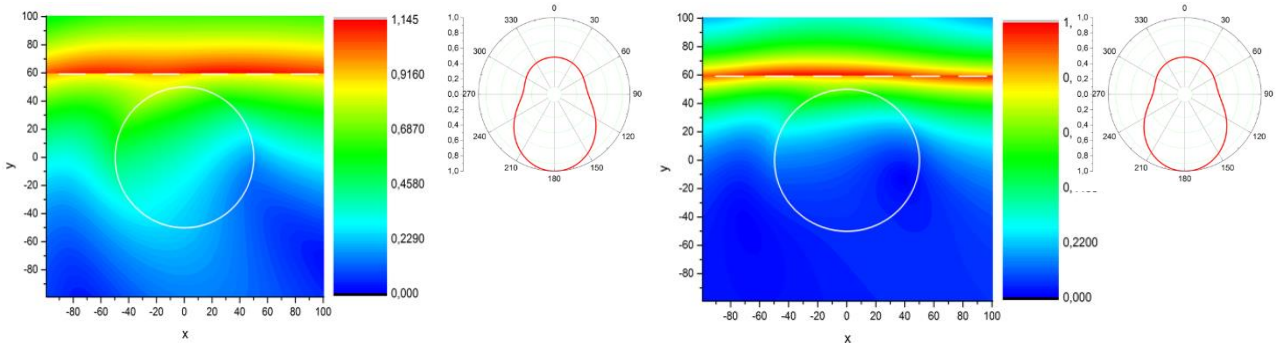

(a) (b)

Fig. 3.6 The same as in Fig. 3.5 however for the λ = 318 nm in the TSCS minimum

The almost omnidirectional shape of the far-field DR patterns can be explained by the comparable contribution of the symmetric and anti-symmetric along the *y*-axis field parts. Its maximum is always oriented in the normal direction to the beam trajectory.

3.2 Twin silver nanowires: resonances on the plasmon supermodes

In this section, the DR from a modulated beam of electrons moving between the twin circular silver nanowires is considered.

Consider two identical circular silver nanowires (marked #1 and #2 in Fig. 3.7) separated by the distance L between their axes, with the same radius a and complex refractive index $\alpha(\lambda)=\sqrt{\varepsilon}$. The gap between the wires is $s=L-2a$ and the Cartesian and the local, $(r_{1,2},\varphi_{1,2})$, and the global, (r,φ), polar coordinates are chosen as shown in Fig. 3.7.

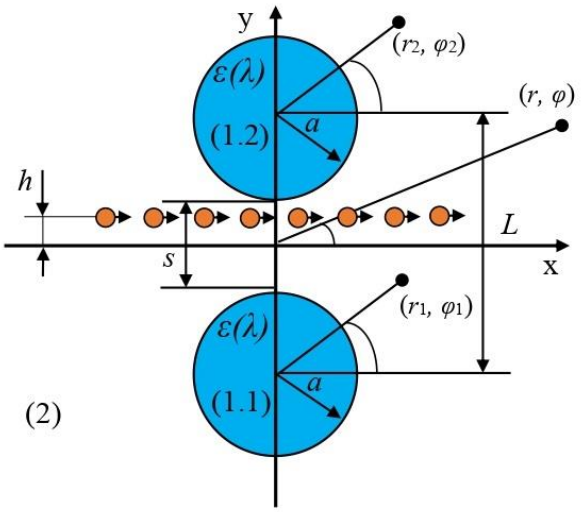

Fig. 3.7. Cross-sectional geometry of a plasmonic PM made of two identical circular silver nanowires excited by a modulated electron beam moving between them

Consider now a one-dimensional electron beam moving along a straight trajectory at the distance $h < s/2$ from the x-axis. The charge density function and the EM field of the beam are represented as in section 1.2. Its magnetic field in free space is given by (1.2) and has finite jump at the trajectory.

In the presence of silver wires, the total magnetic field is different from (1.2). Neglecting the particles deceleration because of the loss of energy (this is called the given-current model), we can assume that the field (1.2) is fixed and consider it as the incident field. Then, to find the total field, we have to solve a 2-D boundary-value wave-scattering problem as explained in chapter 2.

The silver dimer configuration coupled infinite-matrix equations are similar to the dielectric dimer ones (2.33), however, imply the use of the wavelength-dependent complex dielectric permittivity of silver, presented in section 1.3.

The scattering, absorption and extinction cross-sections are calculated similar to section 2.4, where the modified Optical Theorem was also presented.

As we have verified, the error in the Optical Theorem oscillates at the level of machine precision and the error in the boundary conditions is the same level as for the solution of (2.35), controlled by the matrix truncation order M. Additionally, if we set the material of the wire #2 to be the free space, then the computed cross-sections coincide with their values for a stand-alone silver wire, found in analytical form in chapter 2 [17].

Fig. 3.8 demonstrates the dependences of the normalized by $4a$ TSCS and TACS on the electron-beam modulation wavelength in the visible range, for twin silver nanowires with sub-wavelength radii a = 10 nm, 50 nm, and 200 nm, separated by the gap of s = 20 nm. Here, the beam flows along the x-axis (i.e. symmetrically, so that the shift is h = 0) and the beam velocity is β = 0.9 that corresponds to so-called relativistic beam.

The plots of TSCS show one, if a = 10 nm, or a few overlapping peaks, if a is lager. This peak is known as collective resonance on the LSP modes of one thin silver nanowire. In section 3.1, it was already demonstrated that the collective plasmon resonance on a stand-alone metal wire can be excited not only by an H-polarized plane wave as in [80, 128, 131, 95] but also by a modulated electron beam.

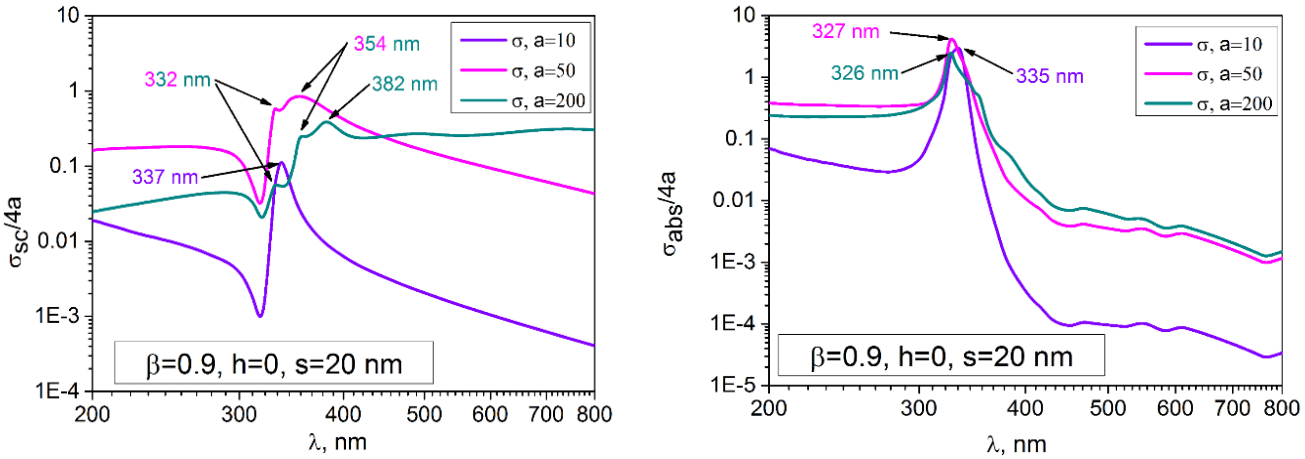

(a) (b)

Fig. 3.8 Normalized TSCS (a) and TACS (b) of two identical silver nanowires versus the wavelength, for the electron beam with the relative velocity β = 0.9 flowing along the x-axis (h = 0)

The plasmonic PM built of twin circular metal nanowires is a more complicated open plasmonic resonator. Its natural modes have much in common with the modes of PM built of two circular dielectric wires, studied in section 2.2 (see also [122]). They form so-called “plasmonic supermodes” built on optically coupled LSP modes of each wire. In the case of twin wires these supermodes make quartets where each of them belongs to one of four independent classes of symmetry of the pair [122]. They can be, therefore, denoted as P_m^{EE}, P_m^{OE}, P_m^{EO}, P_m^{OO}, where $E(O)$ corresponds to the even (odd) dependence on x and y.

Note that similarly to the plane-wave scattering from a single circular silver wire [95], for the thicker wires the LSP peak in the scattering cross-section splits to several ones, where the most red-shifted peak corresponds to the supermode built on the P_1 mode of each wire, and others correspond to the supermodes on the higher-order LSP modes. In view of the symmetry, partial SCS are each equal to one-half of TSCS.

In contrast, the plots of TACS of a deeply sub-wavelength silver wire demonstrate only one common peak, slightly blue-shifted for the thicker wires from the

quasi-static value of 337 nm. The higher-order LSP resonances show up as gentle "shoulders" on the red side of that peak.

The effect of "quasi-invisibility" is present on the plots of TSCS for both thin and thick silver wires (note that this phenomenon has no relation to "Fano-shape" resonances in the other scattering analyses). The associated minimum is especially deep for a deeply sub-wavelength wire. On the plots of TACS, there is no similar minimum due to considerable losses in the bulk silver.

In Fig. 3.9, we present the normalized far-field scattering patterns at the wavelengths of the peaks on the TSCS plots of Fig. 3.8 (a). As the beam flows strictly in the middle between the wires, the angular patterns have zeros along the *x*-axis. The number of lobes in the far zone corresponds to the mode index *m*.

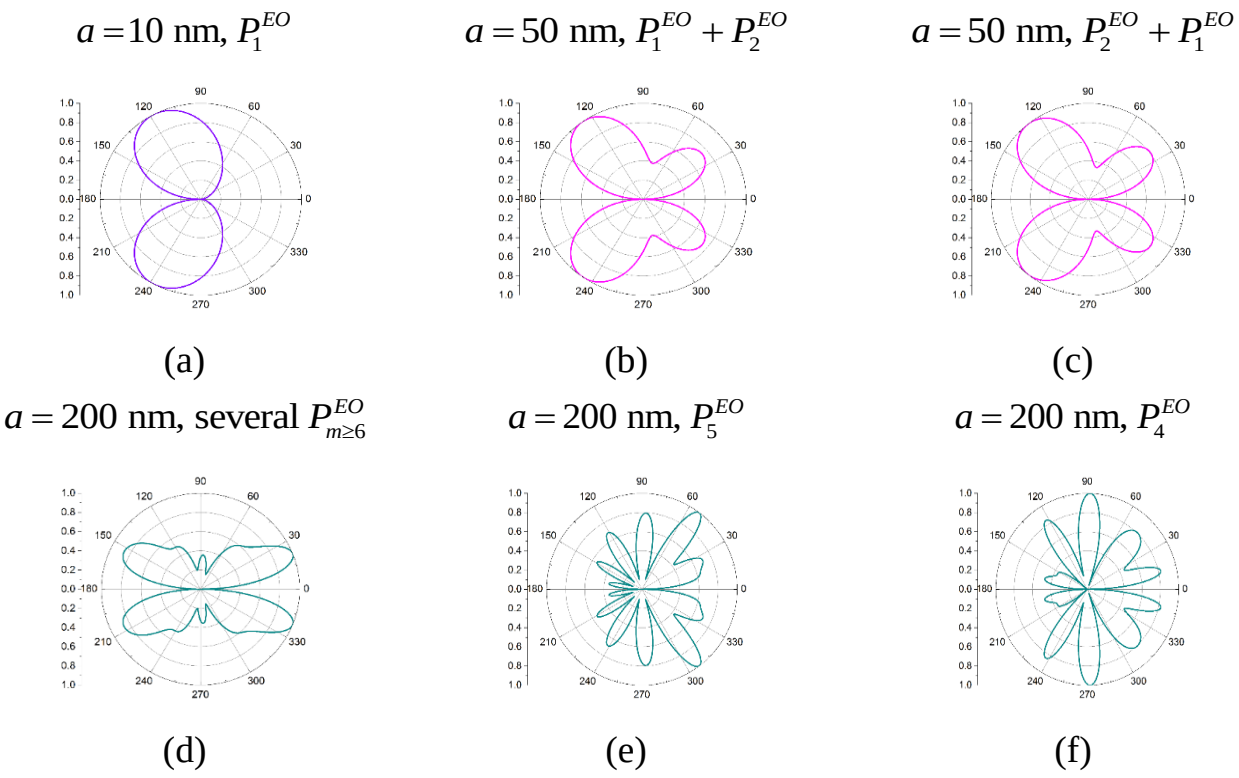

Fig. 3.9 Normalized far-field scattering patterns of the twin silver nanowires for the beam flowing along the *x*-axis (h = 0) with the relative velocity β= 0.9. The wire radius is as indicated, and the wavelength is λ = 337 nm (a), 332 nm (b), 354 nm (c), 332 nm (d), 354 nm (e), and 382 nm (f)

Now, to clarify the effect of the shift of the beam trajectory on the scattering and absorption, we show the visible-range spectra of the partial SCS and ACS for several values of the silver wire radius a and the gap of 20 nm however assuming that h = 5 nm. To see what changes if the beam velocity β varies, we select it as 0.3, 0.5 and 0.9

The plots in Fig. 3.10(a) demonstrate the dependences of the normalized by $4a$ partial SCS on the modulation wavelength in the visible range, for nanowires with deeply sub-wavelength radius of a = 10 nm. As one can see, for all values of β, the plots of partial SCS, $\sigma_{sc}^{(1)}(\lambda)$ and $\sigma_{sc}^{(2)}(\lambda)$, are very close to each other. They show one distinctive peak at λ = 337 nm that does not change its place noticeably if the beam shift h gets larger. Effect of the "quasi-invisibility" is also well visible as a deep minimum, slightly red-shifted from the value of 306 nm where the bulk silver dielectric function is the closest to +1.

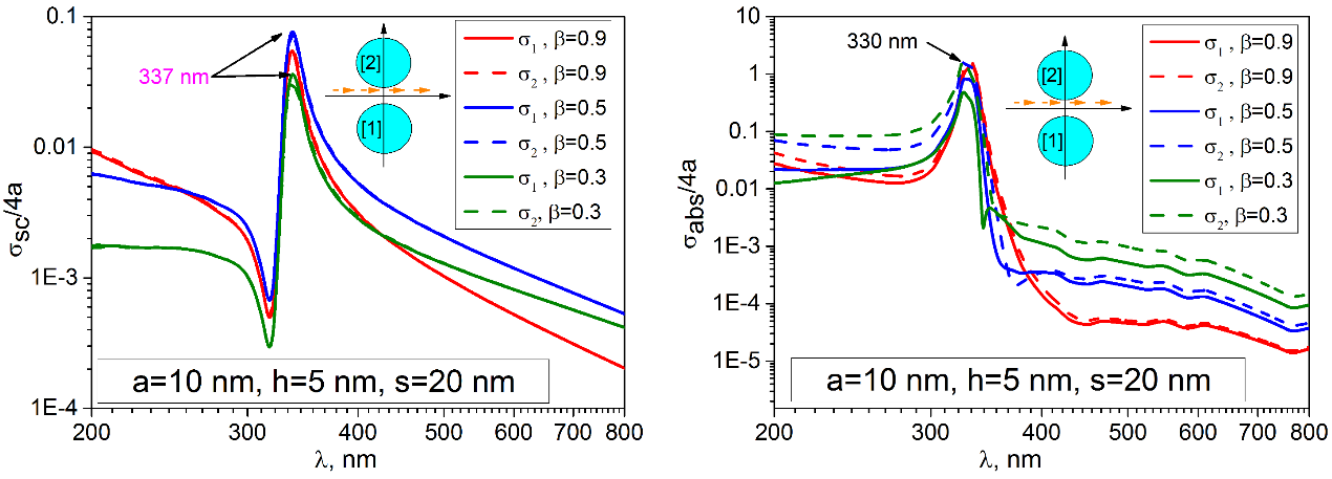

(a) (b)

Fig. 3.10 Normalized partial SCS and ACS of twin silver nanowires with radius 10 nm versus the wavelength in the visible range, for several values of the electron velocity β. The beam flows above the x-axis at the distance h = 5 nm

In the absorption (Fig. 3.10(b)), the LSP peak appears at a slightly blue-shifted position between 330 nm and 335 nm, depending on the velocity β and shift value h. As

already mentioned, there is no “invisibility” effect in the absorption as the silver is sizably lossy in the deep ultra-violet. Note that the partial TCSs of such thin nanowires are practically the same for any beam velocity β. The plots of ACS demonstrate a similar independence of β for relativistic beams, however, if β becomes smaller, the difference in favour of the nearer wire becomes visible.

Colour maps in Fig. 3.11 demonstrate in-resonance patterns of the near magnetic field for such deeply sub-wavelength wires. Panel (a) corresponds to the peak in the scattering. One can conclude that the near field is dominated by the contribution of two nearly degenerate supermodes, P_1^{EO} and P_1^{OO}. The field on the panel (b) corresponds to the “scattering invisibility” wavelength. It shows, indeed, that in this case the beam of particles does not see the silver nanowires, and its field is very close to the field (1.2) in the free space.

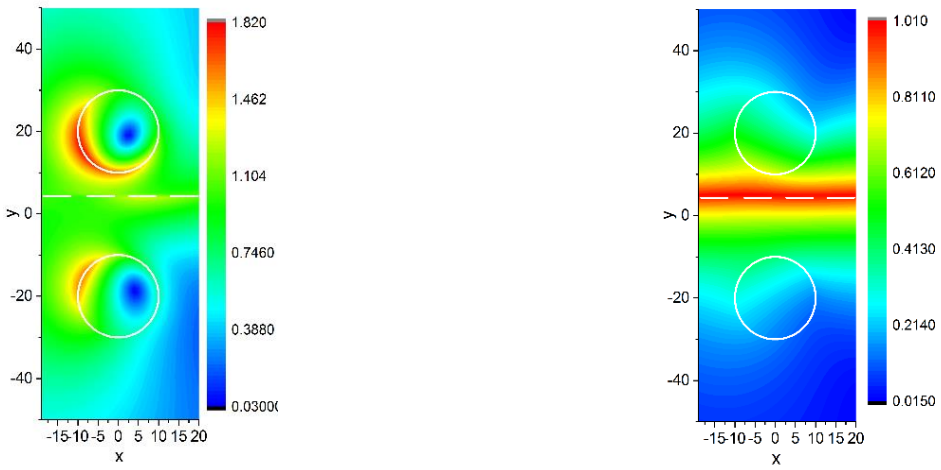

(a) (b)

Fig. 3.11 Normalized near magnetic field patterns of the 10-nm in radius twin silver nanowires excited with the electron beam having the velocity β= 0.3, in the plasmon resonance at λ = 337 nm (a) and in the “quasi-invisibility” case (minimum scattering) at λ = 330 nm (b). The beam flows above the x-axis: h = 5 nm

For the better insight into the physics of DR, the plots in Figs. 3.12 present the

spectra of the partial SCS and ACS for the beam-excited twin silver nanowires of larger radius, 200 nm.

Unlike the thinner wires, these configurations show, besides of the main peak, several smaller ones at the longer wavelengths. They are well resolved on the SCS plots and correspond to the *EO* supermodes built on the higher-order LSP modes P_m of each circular wire (see [133]).

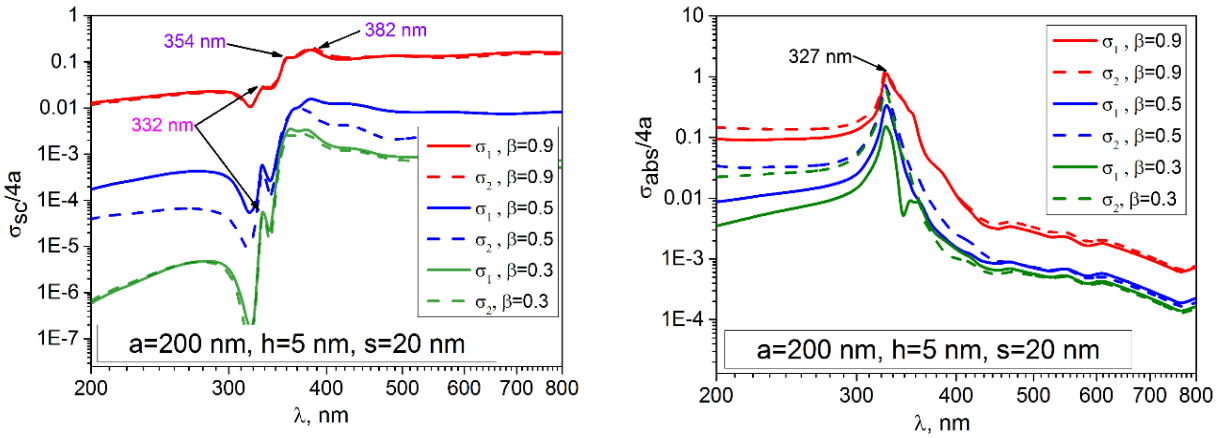

(a) (b)

Fig. 3.12 The same as on Fig. 3.10 however for the wire radius 200 nm

The patterns in Fig. 3.13 correspond to the most "violet" peak of SCS that is collective resonance on higher-order LSP modes. In contrast Fig. 3.14 shows the near fields, dominated by the LSP supermode modes P_m^{EO} with m = 5 (a) and m = 4 (b), respectively. This interpretation is also supported by the far-field angular scattering patterns, presented in Fig. 3.9. The plots of partial cross-sections show that, unlike thinner wires, the thicker ones demonstrate that the nearer to the beam wire is both a stronger scatterer and a stronger absorber unless the beam is relativistic (that is if $\beta \to 1$) although for the 200-nm wire the near field patterns are almost symmetric.

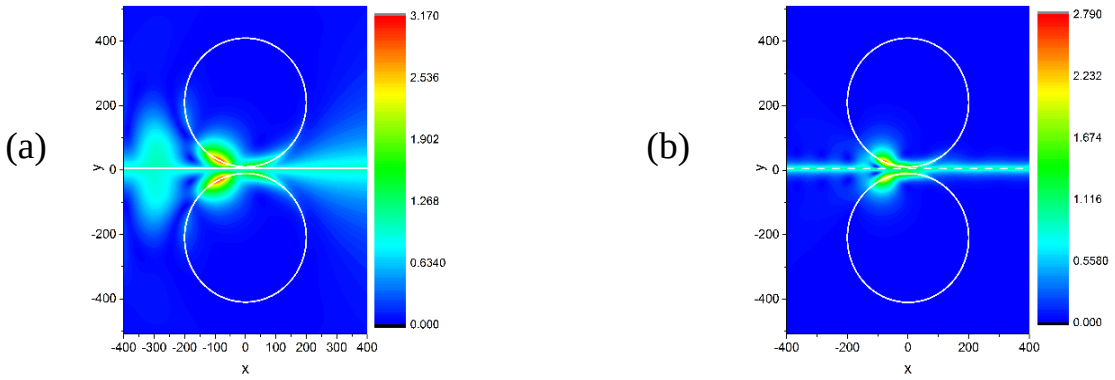

Fig. 3.13 Near magnetic field patterns of the 200-nm in radius twin silver nanowires at λ = 332 nm (the most "violet" peak), for the electron beam velocity β= 0.9 (a) and β= 0.3 (b); the beam flows above the x-axis (h = 5 nm)

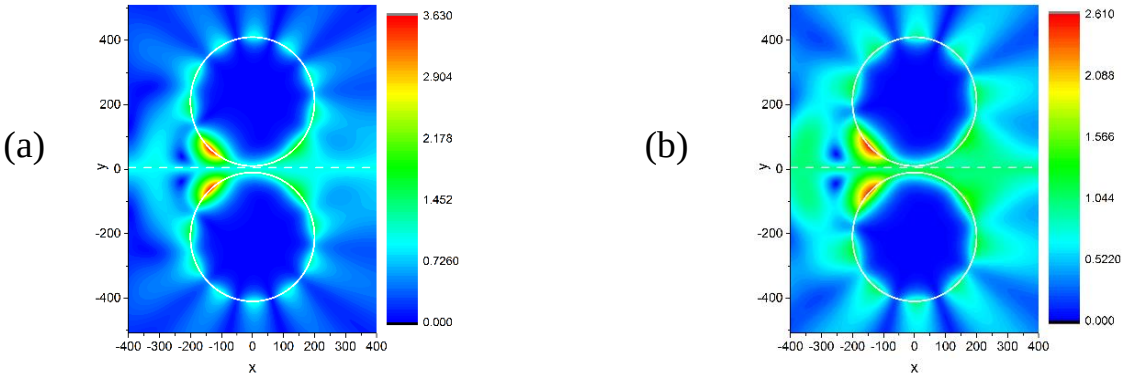

Fig. 3.14 The same as in Fig. 3.13 however in the smaller peaks of TSCS in Fig. 3.12, that is at λ = 354 nm (a) and λ = 382 nm (b). The electron beam is relativistic, β= 0.9, and flows above the x-axis, h = 5 nm

Thus, the spectra of DR-caused SCS and ACS for solid circular silver wire dimer show that such a configuration "does not feel" the shift of the beam trajectory from the central position. This happens because (i) the LSP modes of single wire and LSP supermodes of dimer are nearby degenerate and cluster at the "textbook" wavelength, where $\mathrm{Re}\,\varepsilon(\lambda)=1$, and (ii) they have low Q-factors, between 5 and 20.

3.3 Twin silver nanotubes as a model of beam position monitor

The results of the previous section suggest that, to be sensitive to the beam shift, the nanoscale noble-metal dimer elements should have LSP modes, which are (i) well-separated in wavelengths for different azimuthal orders, *m*, and (ii) have larger Q-factors. Such modified elements can be still circular, in cross-section, however, shaped as thin hollow silver nanotubes, as follows from [138, 95].

3.3.1 Formulation and basic equations

Considered BPM configuration is shown in Fig. 3.15. Two circular silver nanotubes (#1 and #2) have the same outer radius *a*, inner radius *b*, and refractive index $\alpha(\lambda) = \sqrt{\varepsilon}$. They are separated by the air-gap *s*, with *L* being the distance between their axes. We assume that beam of particles (1.1) passes between the tubes in parallel to the *x* direction at the distance *h* from its surface. The Cartesian and the local and global polar coordinates are chosen as depicted.

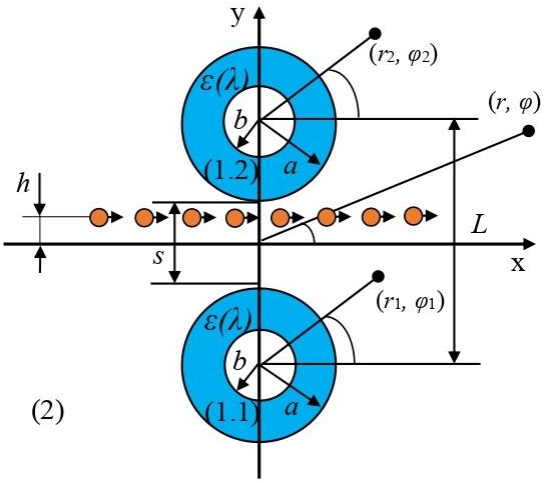

Fig. 3.15 Cross-sectional geometry of electron beam moving between two identical circular silver nanotubes

The formulation of the 2-D wave-scattering problem for the DR field, i.e. the scattered field function, involves the Helmholtz equation, the penetrable-boundary conditions at tube contours, the Sommerfeld radiation condition at infinity, and the condition of local power finiteness. The solution uniqueness is guaranteed by these conditions.

As the nanotube dimer partial domains are different from solid wire case, below we present complete derivation of the resulting matrix equations.

Inside each void and tube (domains I and II), we expand the magnetic field in the azimuthal Fourier series, respectively,

$$H^{\mathrm{int}(p),I}(r_p,\varphi_p)=\sum_{m=-\infty}^{\infty} y_m^{(p)} J_m(kr_p)e^{im\varphi_p},\ r_p<b, p=1,2\ , \tag{3.1}$$

$$H^{\mathrm{int}(p),II}(r_p,\varphi_p)=\sum_{m=-\infty}^{\infty}\left[c_m^{(p)}J_m(k\alpha r_p)+d_m^{(p)}H_m(k\alpha r_p)\right]e^{im\varphi_p}, b<r_p<a\,, \tag{3.2}$$

and seek the scattered field (DR field) as follows:

$$H^{sc}(r,\varphi)=\sum_{p=1,2}\sum_{m=-\infty}^{+\infty} z_m^{(p)}H_m(kr_p)e^{im\varphi_p},\ r_p>a,\vec{r}\in(2), \tag{3.3}$$

At the inner wall of each tube, at $r_p=b,\ p=1,2,$ the boundary conditions demand that both H_z and E_{φ_p} are continuous,

$$H_z^{\mathrm{int}(p),I}=H_z^{\mathrm{int}(p),II},\quad E_{\varphi_p}^{\mathrm{int}(p),I}=E_{\varphi_p}^{\mathrm{int}(p),II}, \tag{3.4}$$

As these conditions are valid for all $0\le\varphi_p<2\pi$, they allow us to exclude some of the unknown coefficients. The boundary conditions at the other walls, at $r_p=a$ and

$0 \le \varphi_p < 2\pi$, are

$$H_z^{\text{int}(p),II} = H_z^0 + H_z^{sc}, \quad E_{\varphi_p}^{\text{int}(p),II} = E_{\varphi_p}^0 + E_{\varphi_p}^{sc} \tag{3.5}$$

Substituting into (3.5) the series expressions (3.2), (3.4) and a similar expansion of the beam field (1.2), and introducing new unknowns, $x_n^{(p)} = z_n^{(p)} w_n$, and $w_{n<0} = (-1)^n w_{n>0}$, $w_{n>0} = n!(2/ka)^n$, we derive two coupled infinite-matrix equations, similar to one found in section 2.4 for p = 1,2.

$$x_m^{(1,2)} + \frac{V_m}{w_m D_m} \sum_{n=-\infty}^{+\infty} x_n^{(2,1)} w_n (\mp i)^{n-m} H_{m-n}(kL) = \beta \frac{f_m^{(1,2)} F_m' - f_m'^{(1,2)} F_m}{w_m D_m}, \quad m = 0, \pm 1, \pm 2, ..., \tag{3.6}$$

where the prime denotes the differentiation in argument and

$$V_m = J_m(ka) F_m' - J_m'(ka) F_m, \tag{3.7}$$

$$D_m = H_m(ka) F_m' - H_m'(ka) F_m, \tag{3.8}$$

$$F_m = J_m(k\alpha a) + H_m(k\alpha a) S_m(kb, \alpha), \tag{3.9}$$

$$F_m' = \alpha J_m'(k\alpha a) + \alpha H_m'(k\alpha a) S_m(kb, \alpha), \tag{3.10}$$

$$S_m(kb, \alpha) = \frac{\alpha J_m'(kb) J_m(k\alpha b) - J_m(kb) J_m'(k\alpha b)}{J_m(kb) H_m'(k\alpha b) - \alpha J_m'(kb) H_m(k\alpha b)}, \tag{3.11}$$

$$f_m^{(1,2)} = \mp A e^{-q(L/2 \pm h)} i^m J_m(ka) (1 \mp \gamma)^m \beta^{-m+1}, \tag{3.12}$$

Note that (3.6) reduces to the twin solid wire case of the previous section if $b \to 0$ that entails $S_m = y_m^{(p)} = d_m^{(p)} = 0$.

Similar to the twin solid-wire case of section 3.2, the set (3.6) is the Fredholm

second kind matrix equation of block (2x2) type (see also [122, 128, 137]). Then the Fredholm theorems guarantee that its numerical solution (after truncation of each block to finite order N_{tr}) converges to the exact solution for $N_{tr} \to \infty$.

On using the large-argument asymptotic expressions for the Hankel functions, far from the scatterer $(r \to \infty)$ the DR field takes the form of outgoing cylindrical wave, similar to

$$H^{sc}(r,\varphi) = (2/i\pi kr)^{1/2} \exp(ikr)\Phi(\varphi), \tag{3.13}$$

where the angular pattern is a function of the global polar coordinate, φ. On the truncation of the matrix equation (3.6), this function depends on the coefficients $z_m^{(1,2)}$ as follows:

$$\begin{aligned} \Phi(\varphi,N) &= \Phi_1(\varphi,N) + \Phi_2(\varphi,N), \\ \Phi_{1,2}(\varphi,N) &= e^{\mp\frac{1}{2}ikL\sin\varphi} \sum_{m=-N}^{N} (-i)^m w_m^{-1} z_m^{(1,2)} e^{im\varphi} \end{aligned} \tag{3.14}$$

Then, the partial SCS, associated with the DR power radiated into the lower and the upper half-spaces, are found as

$$\sigma_{sc}^{(1,2)}(N) = 2\left(\pi k\right)^{-1} \int_0^{\mp\pi} \left|\Phi(\varphi,N)\right|^2 d\varphi, \tag{3.15}$$

The partial absorption cross-sections (ACS) can be found from the Optical Theorem, adapted to the DR analysis as in the previous sections, or, equivalently, through the integration of the Poynting vector flux over the outer contour of each nanotube,

$$\sigma_{abs}^{(1,2)}(N) = \frac{2\pi a}{|\alpha|^2 A^2 \beta^2} \sum_{m=-N}^{N} |g_m^{(1,2)}|^2 \operatorname{Im}\left(\alpha F_m F_m'^*\right), \tag{3.16}$$

where $F_m(\cdot)$ and $F'_m(\cdot)$ are defined in (3.9) and (3.10), and

$$g_m^{(1,2)} = \tfrac{\pi}{2} kb\alpha y_m^{(1,2)} \left[\alpha J_m(kb) H'_m(k\alpha b) - J'_m(kb) H_m(k\alpha b)\right] \tag{3.17}$$

In computations, we use experimental data of [93] for the dielectric function of silver. To check the code convergence for a varying matrix-block truncation order N and visualize its rate, we have computed the relative error, in the far-field SCS, with respect to the data computed at $N_{tr} = 30$,

$$er_{1,2}(N_{tr}) = \left|\sigma_{sc}^{(1,2)}(N_{tr}) - \sigma_{sc}^{(1,2)}(30)\right| / \left|\sigma_{sc}^{(1,2)}(30)\right|$$

The typical plots of such errors are presented in Fig. 3.16 (a).

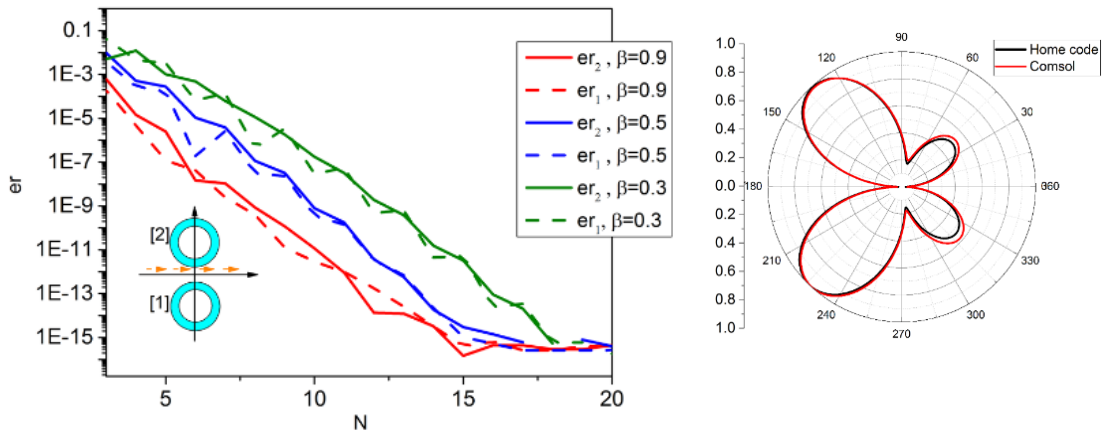

(a) (b)

Fig. 3.16 Far-field computation error versus the matrix block truncation number N_{tr}, for several beam velocities (a) and comparison of the far field patterns calculated by COMSOL and in-house code (b). BPM model consists of two silver tubes with radii a = 50 nm and b = 45 nm, separated by the air gap of s = 20 nm; beam shift is h = 5 nm and wavelength is λ = 332 nm

As visible, 5-6-digit accuracy in the far field is achieved if the truncation order is $N_{tr} \geq \max\left[kL,(k\alpha a/\beta)\right]+5$. Thus, the slower the beam, the larger the matrix size N_{tr} needed for the same accuracy. This is a result of the slower decay of the elements of the right-hand part vector (3.12) at $|m|\to\infty$, controlled by the factor $\beta^{-|m|}$. Equivalently, as $\beta<1$, it means that electric size of the scatterer illuminated with the incident field (1.2) must be increased by the "beam factor," $1/\beta$, in comparison to the plane-wave scattering.

The far-field error is by an order smaller than the near-field error that is explained by the presence of the factor $1/w_m$ in (3.14). Note that the effect of β is the same both in the far and near zone: slower beams request larger matrices to be inverted, for the same accuracy. Besides of β, the electric size of the whole dimer is to be accounted for when selecting N_{tr}. Still besides, the rate of convergence degrades for very small values of the air gap width, *s*.

It should be noted that, to satisfy the Fredholm theorem conditions, the tubes must not touch each other or the beam trajectory.

To support our results, we present, in Fig. 3.16 (b), a comparison of two normalized far-field patterns, computed with our code based on (3.6), where $N = 30$, and with COMSOL commercial software. The agreement is quite good, while the computation time needed by COMSOL is approximately 30 times larger. Still, from the mathematical point of view, this comparison serves as a validation of COMSOL rather than our code because COMSOL's accuracy is not controlled.

3.3.2 Diffraction radiation from small and large radius nanotubes

Keeping in mind BPM applications, we look for the features of DR that can serve as indicators of the beam shift from the central-symmetric position between the twin silver nanotubes. Therefore, we compute the spectra, in the visible-light range, of the partial SCS of the studied configuration, excited by symmetric and shifted beams. The

plots in Fig. 3.17 correspond to the nanotubes of the 55-nm outer radius and 5-nm wall thickness, with the air gap width s = 20 nm. Two trajectories of particles are considered: shifted by h = 5 nm (solid and dashed curves) and not shifted (h = 0, dotted curves), and three beam velocities, $\beta = 0.9, 0.5$ and 0.3. In each case, we can see sharp resonances. This is because LSP modes of single silver tube are well separated, in frequency, for different azimuthal orders, m [95,138]. Moreover, the silver nanotube modes are hybrid, i.e. formed as sums and differences of the plasmon modes of the inner and outer tube surfaces. Their wavelengths, respectively, satisfy the quasi-static equations [138],

$$\varepsilon(\lambda_m^{\pm}) = -1 \pm 2\left[\left(1+\frac{a-b}{a}\right)^m \pm 1\right]^{-1}, \qquad (3.18)$$

More accurately, in a twin-circular-nanotube plasmonic PM, these modes hybridize further and form quartets of closely spaced "supermodes," with mode fields belonging to four classes of symmetry with respect to the x and y-axes [122]. The beam field (1.2) is anti-symmetric with respect to the beam trajectory. Therefore, two of four "supermodes" of each type cannot be excited by the symmetrically flowing beam (they remain "dark") however they can shine if the beam is shifted ($h \neq 0$). Indeed, this is actually what we observe at λ = 803 nm in Fig. 3.17, provided that the beam is non-relativistic, $\beta = 0.3$.

Such interpretation is fully supported by the near-field patterns in the resonances, shown in Fig. 3.18. Panels (a) and (b) and (c) demonstrate the field portraits where the "dipole" LSP mode $P_1^{(-)}$ dominates on each tube; however, the field symmetry on (a), (b) is orthogonal to that on (c).

The plots in Fig. 3.19 show the visible-light spectra of partial SCS for the pair of nanotubes with much larger radii of a = 200 nm and b = 195 nm, so that the wall thickness is again 5 nm, with the air-gap of s = 20 nm. The electron-beam velocities are the same as in the previous case.

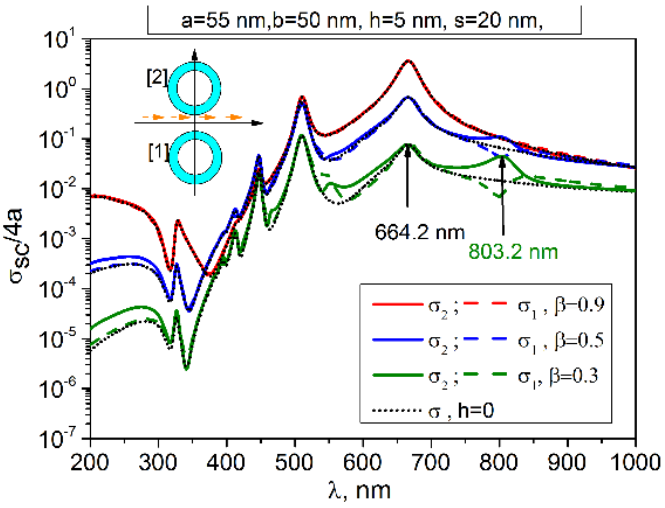

Fig. 3.17 Normalized partial SCS versus the wavelength for twin silver tubes with radii a = 55 nm, b = 50 nm, beam shift h = 0 and 5 nm, and air gap width s = 20 nm

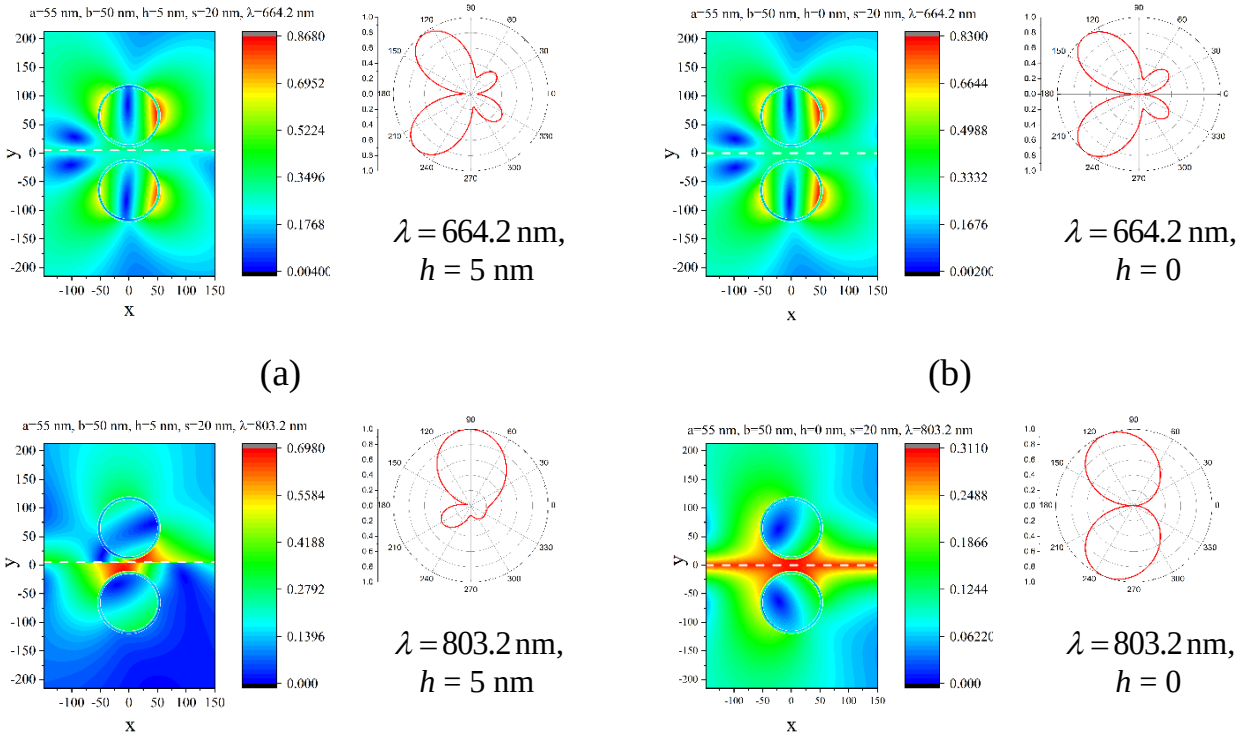

Fig. 3.18 In-resonance near magnetic field and far field scattering patterns of twin nanotube with radii a = 55 nm, b = 50 nm, air gap width s = 20 nm and beam shift h = 5 nm (a), (c) and h = 0 (b), (d)

The trajectory shift is h = 5 nm and the data for zero shift are also shown as dotted curves.

As before, one can see the sharp resonance peaks of the DR power on the wavelengths of the hybrid LSP supermodes of the silver tubes. They form a nearly periodic sequence where each peak corresponds to different azimuth index, m = 1,2, …. Note that they are much sharper than the collective LSP peaks in the DR power for electron-beam excited solid silver nanowire or a pair of them.

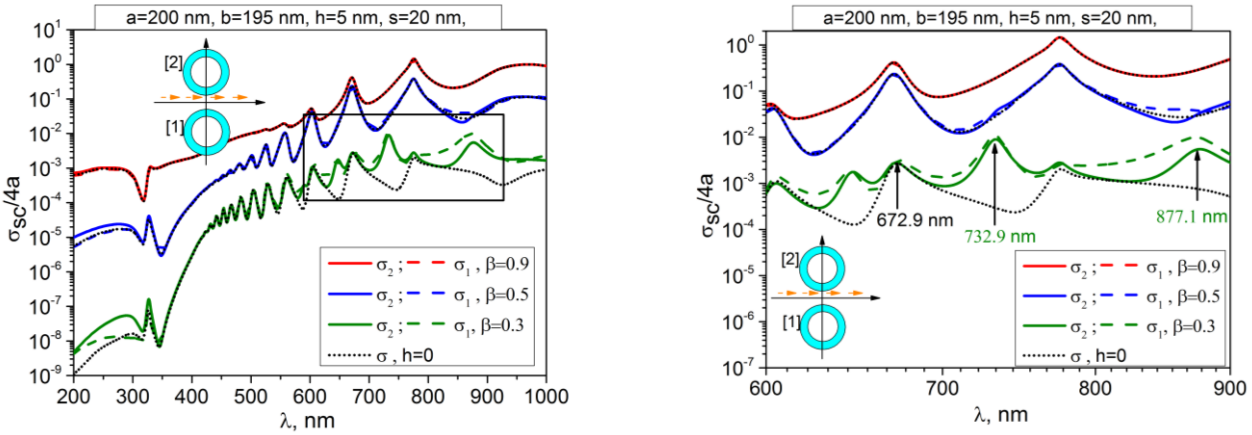

(a) (b)

Fig. 3.19 The same as in Fig. 3.17 for twin silver tubes with radii a = 200 nm and b = 195 nm (a) and its zoom between the wavelengths of 600 nm and 900 nm (b)

Similar to the previous case, some of the peaks appear only if the beam is shifted from the center of the air-gap. For instance, this takes place at λ = 733 nm and 877 nm.

The corresponding to them hybrid LSP supermodes of twin nanotubes remain "dark" under the excitation by the centrally flowing beam, the field (1.2) of which is orthogonal to their eigenfields in symmetry. These modes, however, start resonating (i.e. become "bright") if the beam is shifted, because this leads to appearance of the part of the incident field that matches the mode symmetry.

The in-resonance near-field patterns in Fig. 3.20 correspond to the frequencies marked with arrows in Fig. 3.19. They reveal that the higher-order LSP modes $P_3^{(-)}$

dominate on each tube on panels (a), (b) and (c), however, with different “supermode” symmetries. On panel (e), the field of the LSP mode $P_2^{(-)}$ can be identified. The peaks at the shorter wavelengths correspond to the larger LSP indices *m*.

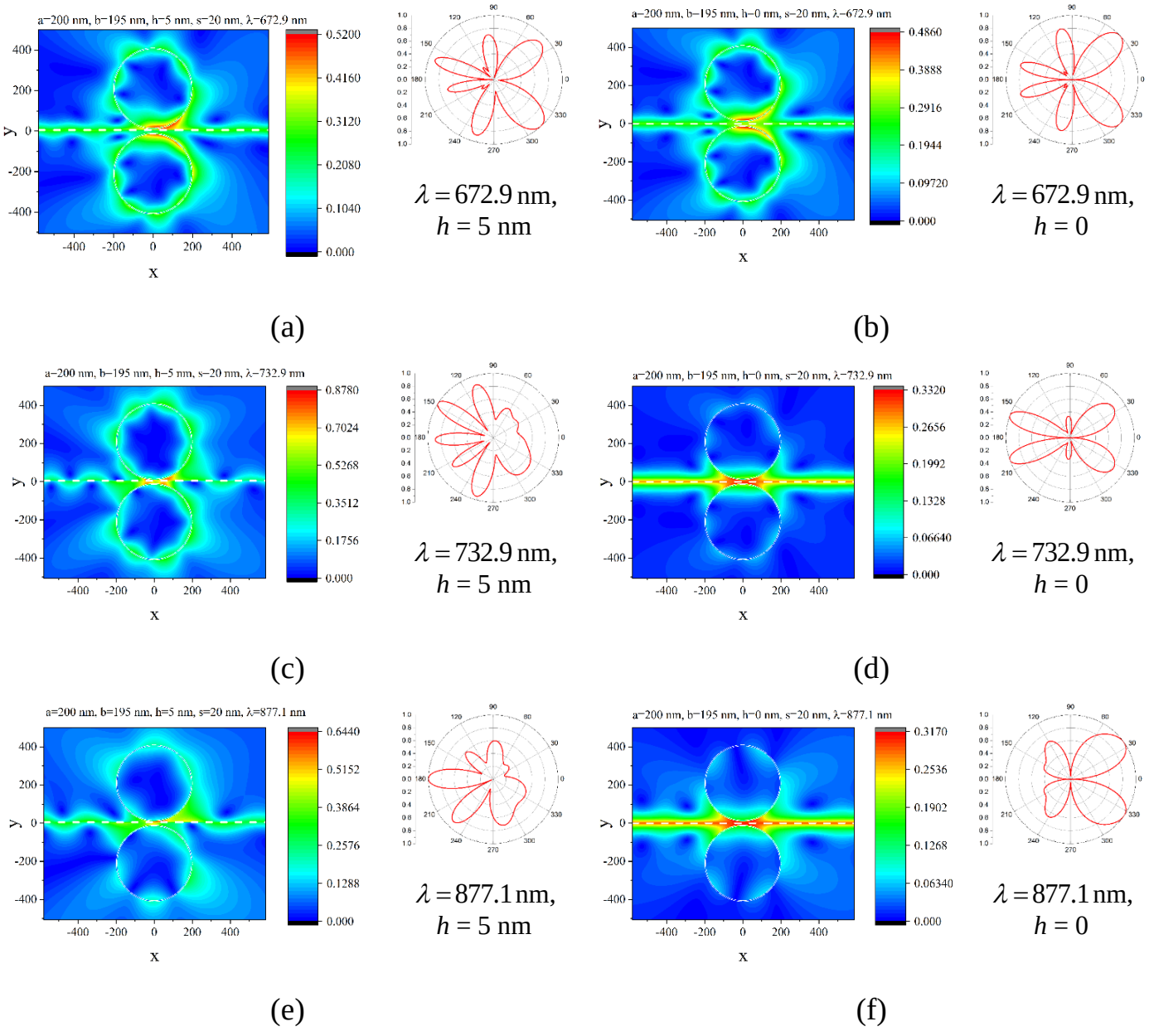

Fig. 3.20 In-resonance near magnetic field and far field scattering patterns of twin nanotube BPM with tube radii *a* = 200 nm, *b* = 195 nm, air gap *s* = 20 nm and beam shift *h* = 5 nm (a), (c), (e) and *h* = 0 (b), (d), (f). marked with arrows in Fig. 2.19

3.3.3 Absorption of light by twin nanotubes

As the silver is sizably lossy in the visible-light range, the absorbed in the nanotubes power is not expected to be small. We characterize this power with the aid of two partial ACS, given by (3.15). In Fig. 3.21, we present the spectra of ACS for the same two configurations of twin-nanotube BPM, however only for the case of the trajectory, shifted by 5 nm from the central-symmetrical position. They show the resonances on the hybrid LSP supermodes of twin silver nanotubes. As discussed above, some of these supermodes are not excited by a non-shifted beam.

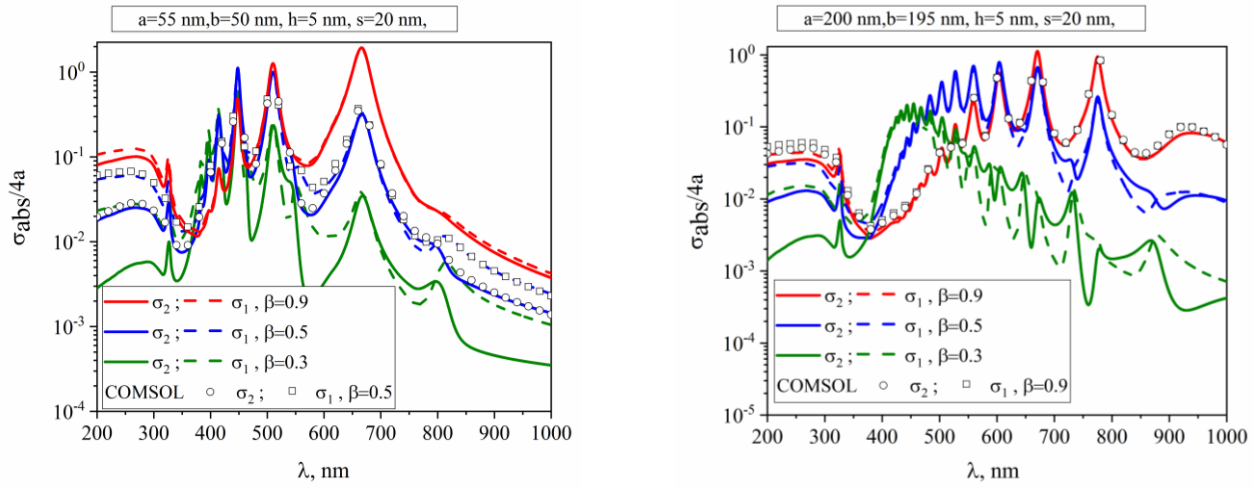

(a) (b)

Fig. 3.21 Normalized partial ACS versus the wavelength for twin silver tubes with radii a = 55 nm, b = 50 nm (a), and a = 200 nm, b = 195 nm (b) beam shift h = 5 nm, and air gap width s = 20 nm

In general, one can see that the absorption in nanotubes is roughly by an order of magnitude larger than the scattering. This is in full agreement with similar relationship between the plane-wave scattering and absorption by metal nanoparticles in the visible range [19,20].

To provide a better vision of the dependence of total SCS and ACS on the wavelength and the tube wall thickness, we present the color maps of these quantities

for the not-shifted and shifted beam in Fig. 3.22 and Fig. 3.23, respectively. White dashed curves are predicted by the quasi-static analysis of hybrid LSP modes $P_m^{(-)}$ of stand-alone nanotube, see [138]. These maps visualize the resonance on the supermode $P_1^{(-)}$ of the *y*-even family, marked with arrow, which is present if h = 5 nm, however remains "dark" if the beam is not shifted.

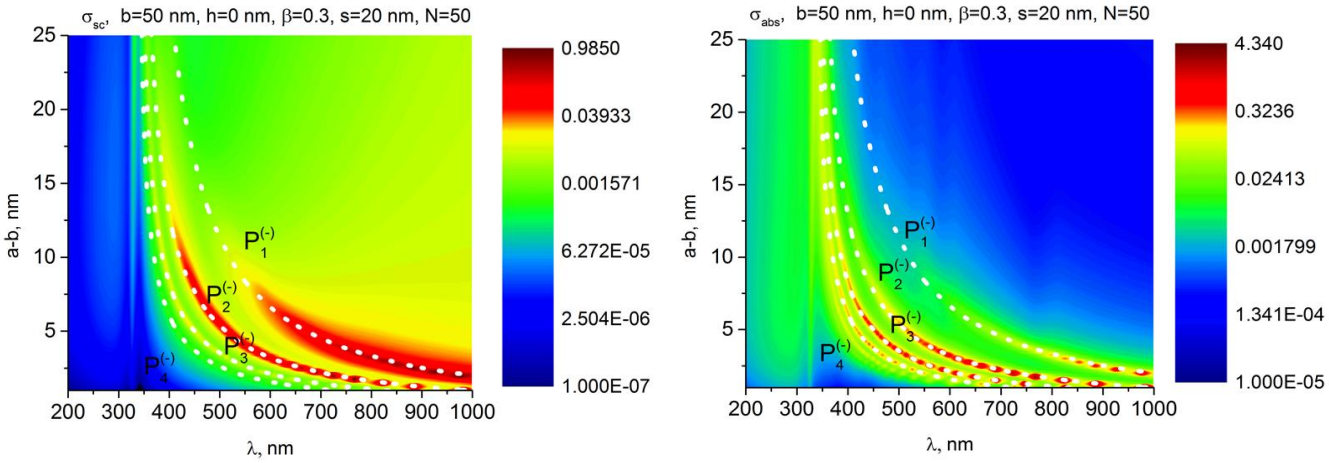

(a) (b)

Fig. 3.22 Color maps of total SCS (a) and ACS (b) versus the wavelength and the tube thickness for twin silver tubes with inner radius b = 50 nm, air gap width s = 20 nm, beam velocity β = 0.3, and no beam shift (h = 0)

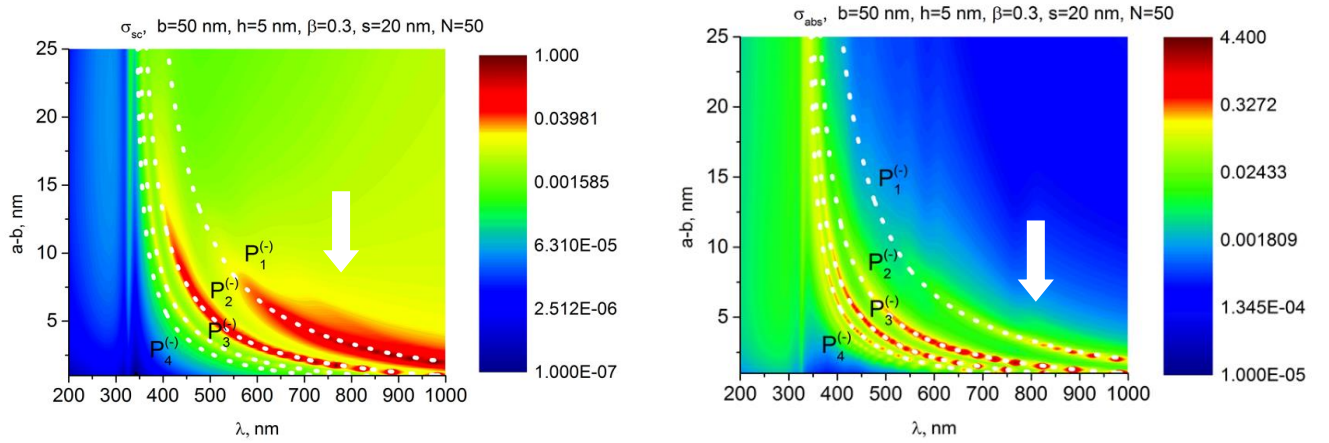

(a) (b)

Fig. 3.23 The same as in Fig. 3.22 however for the beam shift h = 5 nm

3.3.4 Estimation of electron-beam power loss

Presented above are the data for partial and total SCS and ACS, which are traditional quantities in the analysis of optical scattering. Together, they yield the extinction cross-section, which characterizes the total power taken from the incident field in the presence of scatterers. Still, unlike the traditional plane-wave scattering, the power carried by the beam field (1.2) through the plane, normal to its trajectory, is finite. This power is given by the equation

$$P_0 = A^2 Z_0 \beta^2 (k\gamma)^{-1} \tag{3.19}$$

Therefore, it is useful to compare (3.19) with the scattered and the absorbed powers, given by $P_{sc/abs} = \frac{1}{2}\beta\sigma_{sc/abs}$. In Fig. 3.24 and 3.25, we show the spectra of the normalized quantities, P_{sc} / P_0 and P_{abs} / P_0, computed via the data of Fig. 3.17 and 3.19, respectively. As one can see, if the beam velocity does not exceed β = 0.5, the radiated power remains below 5% of the beam power even in the resonances, both for small (a = 55 nm) and large (a = 200 nm) nanotube dimers. This validates the DR model based on the assumption that the beam velocity is fixed.

The power, absorbed in the silver nanotubes, is several dozen times larger than the DR power, and in the LSP-mode resonances it can exceed 50% if β = 0.5 for a small-tube dimer and even 70% for a large-tube dimer. Therefore, the absorption plays more important part than the scattering, in the total reduction of the beam power. This reminds us that even the most sophisticated particle accelerators sometimes suffer of unwanted heating incidents [139].

Additionally, this tells that the fundamental assumption of the DR modelling, that the beam is not influenced by the presence of imperfect scatterers, holds true only provided that the scatterers are not tuned to high-Q resonances and, generally speaking, if the beam is not relativistic. For the twin nanotubes studied here, the safe limit, in

terms of velocity, is around β= 0.2: then the total power loss of the beam is within 10%, some 1% of which goes to DR and the rest – to the heating. To widen the area of applicability of the DR model, one should consider the configurations, where the scatterers are placed at the larger distances from the beam trajectory.

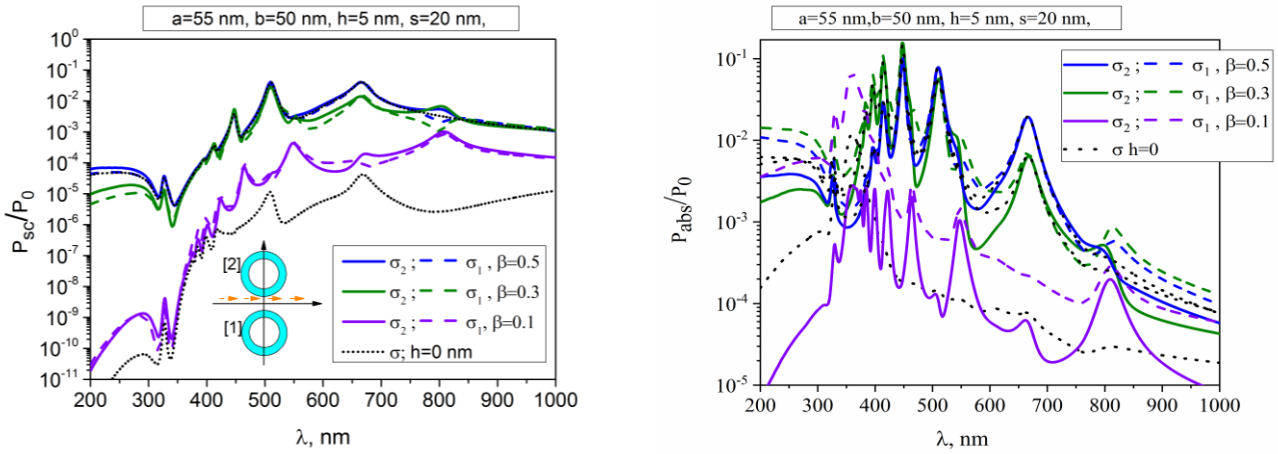

(a) (b)

Fig. 3.24 Partial SCS (a) and ACS (b) versus the wavelength for twin silver tubes with radii a = 55 nm, b = 50 nm, beam shift h = 5, and air gap width s = 20 nm

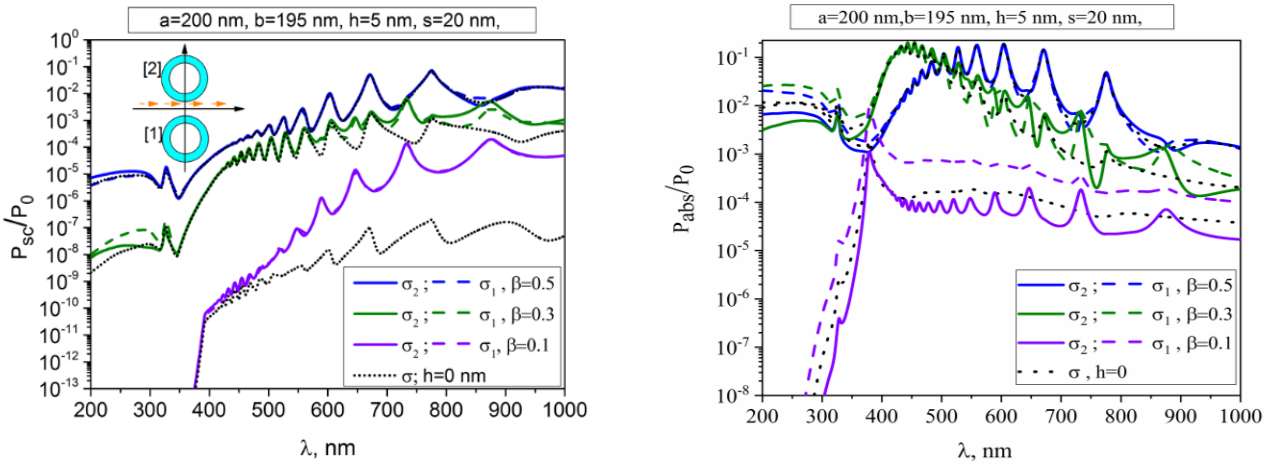

(a) (b)

Fig. 3.25 The same as in Fig. 3.30 for tubes with radii a = 200 nm, b = 195 nm

Conclusions to Chapter 3

- We have studied the optical-range DR that accompanies the motion of the charged-particle beam near a stand-alone plasmonic silver nanowire that has never been considered earlier. As we have shown, both the radiated and the absorbed powers are enhanced near the natural mode wavelengths of the plasmonic nanowire as open resonator. In this case, in-resonance fields are shaped as rotating cylindrical waves made of two degenerate LSP modes with nearly $\pi/2$ phase shift. Unlike DR in the presence of a dielectric nanowire, a metal nanowire placed in vacuum also displays the effect of "invisibility" at the wavelength close to the optical transparency of metal.

- Besides, we have investigated, for the first time to the best of our knowledge, how the visible-light DR is emitted if a beam moves between a pair of identical circular silver nanowires. As we have found, they behave as optically coupled plasmonic open resonators. Because of the losses in silver, their LSP supermodes (that is, hybrid modes) have rather low Q-factors however are still able to enhance the DR at the corresponding wavelengths. If the beam trajectory shifts away from the central (symmetrical) position between the silver wires, then the near field pattern also loses symmetry. This is better visible if the wire radius is truly sub-wavelength and the beam is non-relativistic. Still, unlike a pair of high refractive index dielectric nanowires, the low values of LSP mode Q-factors and their clustering near to the same wavelength show that the solid circular metal wires are not the optimum shape for the applications related to the optical beam-position monitors.

- Trying to overcome the above mentioned circumstances, we have shown, using a trusted and efficient in-house computational instrument, that the modulated beam of charged particles can be monitored noninvasively by measuring the power of the DR, if the beam passes between two identical thin silver *nanotubes*. This power, as a function of the modulation wavelength, displays sharp peaks on the hybrid LSP supermodes of twin nanotubes, now well separated for the different azimuthal orders. Some of these modes are excited only if the beam trajectory is shifted away from the central-

symmetrical position, due to the symmetry properties of the corresponding supermode field. This effect can be used in the design of optical-range BPMs. We have also shown, for the first time in our opinion, that the area of good adequacy of the DR model is limited, in the presence of nanoscale resonant scatterers, to the non-relativistic beam velocities.

CHAPTER 4 DIFFRACTION RADIATION OF A BEAM OF PARTICLES MOVING NEAR GRAPHENE-COVERED DIELECTRIC NANOWIRES

In this chapter, the DR-caused scattering and absorption characteristics in the visible range are numerically investigated for a stand-alone circular dielectric nanowire covered with graphene, twin graphene-coated nanowires configuration and finite array of circular graphene-covered dielectric nanowires. As in previous chapters, we assume that the beam velocity is fixed and use the separation of variables in local coordinates and the addition theorems for cylindrical functions to cast the DR problem to a Fredholm second-kind matrix equation. For the zero-thickness graphene covers, the two-side resistive boundary conditions are requested. Here the electron conductivity and hence the surface impedance of graphene are determined from the Kubo formalism. The materials of Chapter 4 are published in works [A2, A7-9, A11, A13].

4.1 Single circular graphene-coated nanowire: resonances on the plasmon and whispering-gallery modes

The DR problem for the modulated electron beam moving near stand-alone graphene-coated nanowire (see Fig. 4.1) is similar to the DR problem of the beam exciting a dielectric circular nanowire, as presented in sections 2.3. However, the difference is in the graphene material of the dielectric ($\alpha = \sqrt{\varepsilon}$, $k_1 = \alpha\omega / c = \alpha k$) wire cover. Graphene properties were explained in section 1.4 and its surface impedance was discussed there.

4.1.1 Basic equations

As in preceding chapters, the incident field in the DR problem is the free-space electron-beam field given by (1.2), and the scattered field can be presented as (2.22).

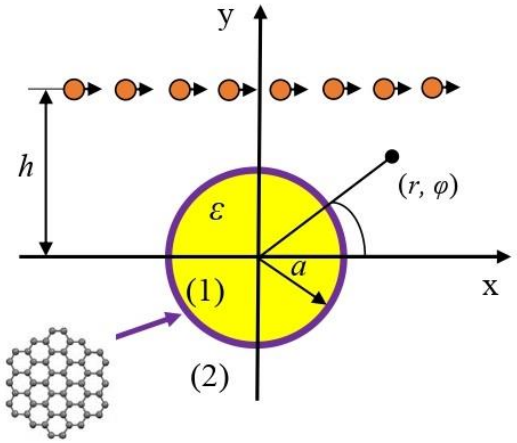

Fig. 4.1 Cross-sectional geometry of electron beam moving over a dielectric circular nanowire coated with graphene

The only difference in the problem formulation is in the boundary conditions, which account for the surface impedance (or resistivity) of graphene, *Z*, and is given by (1.5). These boundary conditions are two: one tells that the tangential electric field should be continuous across the coated wire contour,

$$E_{\varphi}^{0}(a,\varphi)+E_{\varphi}^{ext}(a,\varphi)=E_{\varphi}^{\mathrm{int}(p)}(a,\varphi), \tag{4.1}$$

and the other tells that the tangential magnetic field has a jump proportional to the surface conductivity of graphene,

$$E_{\varphi}^{\mathrm{int}(p)}(a,\varphi)+E_{\varphi}^{0}(a,\varphi)+E_{\varphi}^{ext}(a,\varphi)=2ZZ_0\left[H_z^{\mathrm{int}(p)}(a,\varphi)-H_z^{0}(a,\varphi)-H_z^{ext}(a,\varphi)\right], \tag{4.2}$$

Then, substituting the field expansions (2.22) into (4.2), we obtain

$$\frac{Z_0 f'_m}{ik}+\frac{Z_0 b_m k H'_m(ka)}{ik}=\frac{Z_0 a_m k\alpha J'_m(k\alpha a)}{ik\varepsilon}, \tag{4.3}$$

$$\frac{Z_0 f'_m}{ik} + \frac{Z_0 b_m k H'_m(ka)}{ik} + \frac{Z_0 a_m k\alpha J'_m(k\alpha a)}{ik\varepsilon} = 2ZZ_0\left[a_m J_m(k\alpha a) - f_m - b_m H_m(ka)\right], \quad (4.4)$$

After transformations, we get the following equations:

$$b_m H'_m(ka) - \alpha^{-1} a_m J'_m(k\alpha a) = -f'_m, \quad (4.5\text{-a})$$

$$iZb_m H_m(ka) + \alpha^{-1} a_m J'_m(k\alpha a) - iZa_m J_m(k\alpha a) = -i^{m+1} Z f_m, \quad (4.5\text{-b})$$

Here, the functions f_m and f'_m are the same as (2.26). Then, the field expansion coefficients are found as the following analytical expressions:

$$a_m = [-i^{m+1} Z f_m H'_m(ka) + iZ f'_m H_m(ka)](D_m)^{-1}, \quad (4.6\text{-a})$$

$$b_m = \{-f'_m\left[J'_m(k\alpha a)\alpha^{-1} - iZJ_m(k\alpha a)\right] - f'_m J'_m(k\alpha a)\alpha^{-1}\}(D_m)^{-1}, \quad (4.6\text{-b})$$

where

$$D_m = H'_m(ka)J'_m(k\alpha a)\alpha^{-1} - iZ\left[H'_m(ka)J_m(k\alpha a) - H_m(ka)J'_m(k\alpha a)\alpha^{-1}\right], \quad (4.7)$$

The DR characteristics - SCS and ECS - are the same as for the single dielectric wire and expressed as (1.13) and (1.15). Meanwhile, if the dielectric is assumed lossless, then the absorption cross section (ACS) is given by (1.10).

Considering that $w(\varphi) = H^{ext} + H^0 - H^{\text{int}}$, then

$$\sigma_{abs} = \frac{\pi a}{A^2\beta^2}\,\mathrm{Re}\,Z\left|\sum_{m=-\infty}^{+\infty} a_m J_m(k_1 a) - b_m H_m(ka) - f_m\right|^2, \quad (4.8)$$

Additionally, as we have shown in section 1.5, ACS can be also found with the aid of SCS and ECS from the Optic Theorem - see (1.12).

4.1.2 Natural modes of single graphene-covered dielectric wire

A stand-alone circular dielectric wire covered with graphene is a composite open resonator, which supports the natural modes of two families: dielectric-rod modes, which obtain the features of the whispering-gallery (WG) modes if the radius *a* and/or refractive index $\alpha = \sqrt{\varepsilon}$ is getting larger, and the plasmon modes of the graphene cover.

On the circular graphene-coated wire, complex frequencies of all natural modes satisfy independent equations $D_m = 0$ $(m = 0,1,...)$, where D_m is given by (4.7). The plasmon modes appear in every non-zero azimuthal order, *m* = 1,2, ... [141]. In [99], they have been found approximately, after using small-argument asymptotics in (4.7). However, by analogy to a silver wire [95], they can be also viewed as the natural modes of the traveling-wave resonator formed by the closed contour of graphene cover. Then, neglecting the curvature of the graphene layer, the following empiric characteristic equation can be established:

$$\exp\left(ig_{plasm} 2\pi a\right) = 1, \tag{4.9}$$

where g_{plasm} is the complex wavenumber of the plasmon wave propagating along a flat infinite graphene monolayer located at the interface between air and dielectric. The roots of this equation are, obviously, $g_{plasm} a = m, \quad m = 1,2,...$ and correspond to the plasmon modes, P_m. The value of g_{plasm} can be found analytically – see equation (31) in [142], where we take into account that $|Z|^2 \gg 1$ in THz and IR ranges,

$$g_{plasm}^2 \approx -k^2(1+\varepsilon)\left[Z^2(1+\varepsilon) - \tfrac{1}{2} + O(|Z|^{-2})\right] \tag{4.10}$$

Taking into account that graphene's normalized surface impedance *Z* depends on the frequency as (1.5) and neglecting intraband conductivity (1.3), we conclude that

$$g_{plasm} \approx k^2(\varepsilon+1)\frac{c}{\Omega}\left(1+\frac{i\tau^{-1}}{kc}\right), \tag{4.11}$$

where Ω is a value that follows from (1.3), namely,

$$\Omega = \frac{q_e^2 Z_0 k_B T}{\pi\hbar^2}\left\{\frac{\mu_c}{k_B T}+2\ln\left[1+\exp\left(-\frac{\mu_c}{k_B T}\right)\right]\right\} \tag{4.12}$$

Then, the plasmon mode P_m resonance frequencies (i.e. real parts of the complex natural frequencies) are found approximately as

$$f_m^P \approx \frac{1}{2\pi}\left[\frac{mc\Omega}{a(\varepsilon+1)}\right]^{1/2} \tag{4.13}$$

Note that expression (4.13) agrees with equation (12) of [99] (here, one has to account for the different systems of units, CGS in [99] and SI in our work). Besides, the Q-factors of the plasmon modes, in the same approximation (i.e. the absorption Q-factors), are found to be proportional to the electron relaxation time,

$$Q_m^P \approx \frac{4\varepsilon\tau}{(1+\varepsilon)^{3/2}}\left(\frac{mc\Omega}{a}\right)^{1/2} \tag{4.14}$$

As one can see, both resonance frequencies and Q-factors of the plasmon modes of a graphene-covered circular dielectric wire grow as a square-root of the mode index. Besides, in view of (4.12) they grow approximately as a square-root of the chemical potential, which, in its turn, is known to be proportional to DC bias. Therefore, higher-order plasmon modes have certain advantage, in the higher Q-factors, before the lower-index modes including the principal “dipole” mode, P_1. The growth with m is limited,

however, by the radiation losses, which were neglected when deriving (4.13) and (4.14). The spectral distance between the adjacent plasmon modes gets smaller with *m*.

The dielectric-wire modes, perturbed by the presence of graphene cover, also correspond to the (other) roots of equations $D_m = 0$; if $|Z| >> 1$ and $m >> ka >> m/\alpha$, they obtain the features of the WG modes, such as periodically spaced frequencies and high Q-factors. However, due to the losses in graphene, the exponential growth of the Q-factors with *m* and α is now limited at the level, determined by the graphene parameters, τ, μ_c and *T*. That limit value has the order of $O(\mathrm{ImZ}/\mathrm{ReZ})$.

Note also that, in a stand-alone circular resonator, all modes with $m > 1$ are doubly degenerate, because $\sin m\varphi$ and $\cos m\varphi$ field dependences are orthogonal however lead to the identical characteristic equations.

4.2 Twin graphene-coated nanowires as a model of beam position monitor

Here, we consider a flat modulated beam of electrons flowing along the straight trajectory at the distance *h* from the *x*-axis, with a fixed velocity $v = \beta c$ as described in section 1.2. Two identical circular dielectric wires with graphene covers have the radius *a* and refractive index $\alpha = \sqrt{\varepsilon}$ - see Fig. 4.2. They are placed in the free space with the air-gap *s* and *L* is the distance between their axes. We assume that the beam of particles (1.2) flies in parallel to the *x* direction between the wires at the distance *h* from the center of the air-gap. We introduce the Cartesian and the local $(r_{1,2}, \varphi_{1,2})$ and global (r, φ) polar coordinates as shown in Fig. 4.2.

4.2.1 Basic equations

In the case of the H-polarization, one can derive all the field components from the *z*-component of the magnetic field vector.

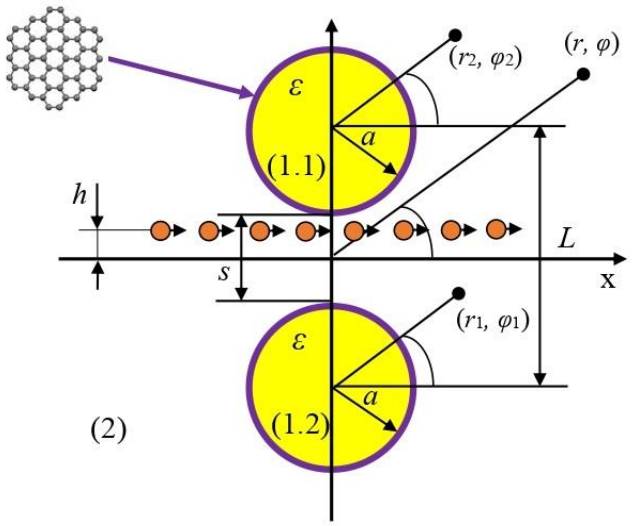

Fig. 4.2 Cross-sectional geometry of electron beam moving between a pair of identical dielectric circular nanowires with graphene covers

Omitting the index *z*, we look for the total field as (2.5). Inside each wire and off them (domains (1.1), (1.2) and (2)), we expand the field in the azimuthal Fourier series in the local polar coordinates as in (2.6) and (2.7), respectively

The boundary conditions at the wire contours, $r_p = a,\ 0 \le \varphi_p < 2\pi\ \ (p = 1,2)$, are the conditions for a zero-thickness resistive sheet placed at the interface between the free space and dielectric; they are expressed as (4.1), (4.2).

Here, the graphene complex-valued surface impedance in the THz range (where the interband conductivity can be safely neglected [21-23,107]) is

$$Z_0 Z\left(\omega, \mu_c, \tau, T\right) = 1/\sigma_{\text{intra}}, \tag{4.15}$$

and was also explained in detail in section 1.4.

On expanding the beam field (1.2) in terms of the Fourier series in the local coordinates similar to section 2.1, we obtain

$$H_z^0(r_{1,2},\varphi_{1,2}) = \mp A\beta e^{-q(L/2\pm h)} \sum_{m=-\infty}^{+\infty} i^m J_m(kr_{1,2}) \left(\frac{1\mp\gamma}{\beta}\right)^m e^{im\varphi_{1,2}}, \quad (4.16)$$

Then, we substitute the series (2.6), (2.7) and (4.16) into the conditions (4.1) and (4.2) and use the Graf addition theorem (2.9) for the cylindrical functions to transfer the expansions from one local coordinate system to the other. Finally, on introducing new unknowns, $z_n^{(p)} = x_n^{(p)} w_n$, $w_{n>0} = n!(2/ka)^{2n}$, $w_{n<0} = (-1)^n w_{n>0}$ we derive two coupled infinite-matrix equations, similar to (2.33), however, containing new terms dependent on *Z*,

$$x_m^{(1,2)} + w_m \frac{V_m}{D_m} \sum_{n=-\infty}^{+\infty} (\pm i)^{n-m} w_n H_{m-n}(kL) x_n^{(j)} = w_m \frac{F_m^{(1,2)}}{D_m}, \quad m = 0, \pm 1, \pm 2, ..., \quad (4.17)$$

where

$$V_m = iZ^{-1} J'_m(ka) J'_m(k\alpha a) + \alpha J'_m(ka) J_m(k\alpha a) - J_m(ka) J'_m(k\alpha a), \quad (4.18)$$

$$D_m = iZ^{-1} H'_m(ka) J'_m(k\alpha a) + \alpha H'_m(ka) J_m(k\alpha a) - H_m(ka) J'_m(k\alpha a), \quad (4.19)$$

$$F_m^{(1,2)} = -iZ^{-1} f_m'^{(1,2)} J'_m(k\alpha a) - f_m'^{(1,2)} \alpha J_m(k\alpha a) - f_m^{(1,2)} J'_m(k\alpha a), \quad (4.20)$$

$$f_m^{(1,2)} = \mp A e^{-q(L/2\pm h)} i^m J_m(ka)(1\mp\gamma)^m \beta^{-m+1}, \quad (4.21)$$

$$f_m'^{(1,2)} = \partial f_m^{(1,2)} / \partial(ka) \quad (4.22)$$

What is important, thanks to the re-scaling of the unknowns with the aid of the factors w_n, the matrix equation (4.17) is the Fredholm second-kind operator equation provided that $L > 2a$ (see the explanations in [24-26]; note that here the presence of the terms with Z^{-1} does not spoil this property). This guarantees the convergence of the numerical solution of (4.17), in mathematical sense: if each block of (4.17) is truncated to finite order N_{tr}, then, by taking progressively larger values of N_{tr}, one can minimize

the error in finding the coefficients $\left\{x_m^{(1,2)}\right\}_{m=-N_{tr}}^{+N_{tr}}$, in principle, to machine precision. Note that without the mentioned re-scaling, the matrix equation of this kind can provide, at best, the accurate values of the first 2-3 digits and hence remains impractical in the case of sharp resonances. This crucial circumstance is frequently overlooked or neglected even in the tutorials - see, for instance, [82, 85, 99, 129, 140].

As we are interested in the modeling of BPM, we have to compute some DR characteristics, which can be observable in practical situations. As usual, such characteristics are related to the field far from the scatterers. The partial SCS corresponding to the DR power, radiated to the lower and the upper half-spaces, are given by (1.8).

Still, the scattering is accompanied with the absorption because graphene is a lossy material, see (4.15). Therefore, we introduce the partial ACS, found as

$$\sigma_{abs}^{(1,2)} = \pi a \frac{\mathrm{Re}\, Z}{A^2 \beta^2} \sum_{n=-\infty}^{\infty} \left| -y_n^{(1,2)} J_n(k\alpha a) + f_n^{(1,2)}(ka) + z_n^{(1,2)} H_n^{(1)}(ka) + \right. \tag{4.23}$$

$$\left. J_n(ka) \sum_{m=-\infty}^{\infty} (\pm i)^{m-n} z_m^{(2,1)} H_{n-m}^{(1)}(kL) \right|^2$$

Note that the sum of the partial SCS and ACS is the extinction cross-section, $\sigma_{ext} = \sigma_{sc}^{(1)} + \sigma_{sc}^{(2)} + \sigma_{abs}^{(1)} + \sigma_{abs}^{(2)}$. This value is linked to the DR far-field amplitude,

$$\Phi(\varphi) = \sum_{m=-\infty}^{+\infty} (-i)^m w_m \left[e^{-\frac{1}{2} ikL \sin\varphi} z_m^{(1)} + e^{\frac{1}{2} ikL \sin\varphi} z_m^{(2)} \right] e^{im\varphi}, \tag{4.24}$$

computed in the directions of the so-called complex angles of incidence (see section 1.5 and [25] for details),

$$\sigma_{ext} = -\frac{4}{kA\beta} e^{-qL/2} \,\mathrm{Re} \sum_{m=-\infty}^{+\infty} (-i)^m \beta^m w_m \left[\frac{e^{-qh} z_m^{(1)}}{(1+\gamma)^m} + \frac{e^{qh} z_m^{(2)}}{(1-\gamma)^m} \right] \tag{4.25}$$

This is the Optical Theorem for the DR, which accompanies the motion of the modulated beam of charged particles between scattering obstacles. It can be used for a partial validation of the computed results. In our analysis, this expression has been satisfied at the level of machine precision.

4.2.2 Natural modes of graphene-covered dimer

Configuration of twin circular dielectric wires, shown in Fig. 4.2 and known as dimer, is even more complicated open resonator than a stand-alone graphene-covered wire, because the modes of individual wires are now optically coupled. Mathematically, this is visible from the fact that now the mode equations do not split into the azimuthal orders and their natural frequencies are the roots of the determinantal equation, generated by the whole matrix (4.18). Physically, the optical coupling forces the modes to hybridize; to emphasize the coupling, the hybrid modes of the dimer are called "supermodes" [122]. Due to the presence of two lines of symmetry, in the cross-section (which are the *x* and the *y* axes), all supermodes of a circular-wire dimer split into four orthogonal classes according to the field symmetry (even dependence) or anti-symmetry (odd dependence) along these axes. They are usually denoted as *EE*, *EO*, *OE* and *OO* classes and can be studied separately after the separation of corresponding determinantal equations [122].

Therefore, for a dimer of twin circular open resonators, instead of a single doubly degenerate LSP mode of each wire, a quartet of closely spaced LSP supermodes appears. A numerical study of the supermodes of twin dielectric disks has shown (see [122]) that each quartet of supermodes forms two even closer spaced doublets, of the *EE* and *OE* modes and the *EO* and *OO* modes, respectively. Recently, the same has been demonstrated for the LSP supermodes of a dimer of graphene-covered dielectric wires [99]. Numerical analysis of the supermodes of graphene-covered dimer will be presented in Chapter 5 in the LEP formulation.

4.2.3 Numerical results: resonances on the plasmon supermodes

In the case of 2-D modelling, a design of DR-based BPM sensor involves not a single scatterer but two identical ones, for instance, the edges of a slot [16], so that the beam moves between them. Then a difference in the DR intensity or in the angular radiation patterns from the opposite sides of the beam trajectory can serve as indicator of a shift in the beam position. This explains the interest in the twin solid dielectric nanowire and twin noble-metal solid-wire and nanotube BPM configurations, studied in previous chapters. Note that DR from a dimer of spherical dielectric particles has been studied in [143] in approximate manner, using the concept of the averaged polarizability.

In the full-wave analysis, our goal is to investigate how the position of the beam trajectory influences the power of DR and the excitation of high-Q plasmon resonances. Figs. 4.3 to 4.5 present the results of the calculation of normalized partial SCS and ACS versus the frequency for twin graphene-covered dielectric nanowires with radius a = 500 nm and 100 nm, separated by the air gap of the width s = 100 nm. The relative dielectric constant of the wire material is assumed to be 2.4. Graphene parameters are T = 300ºK, τ = 0.5 ps, and several values of the chemical potential are tried. Two beams with the same relative velocity β = 0.5 are considered: not shifted from the central-symmetric position, h = 0, and shifted by h = 40 nm.

The truncation order of the blocks of the matrix equation (4.19) is selected according to the rule, explained in [41]: $N_{tr} = \max\{k\alpha a, ka/\beta\} + 5$ that guarantees 5 correct digits in the found coefficients. This rule is especially important for the non-relativistic beams, $\beta << 1$, because the right-hand part coefficients in (4.18) behave as $O[(ka/2\beta)^{|n|}]$ if $|n| > ka$, i.e. drop slowly.

For the selected geometrical and material parameters, single wire plasmon-mode resonance frequencies are well predicted by equation (4.13) and get to the IR frequency range. Small shifts from (4.13), for the dimer supermodes, can be also estimated [99].

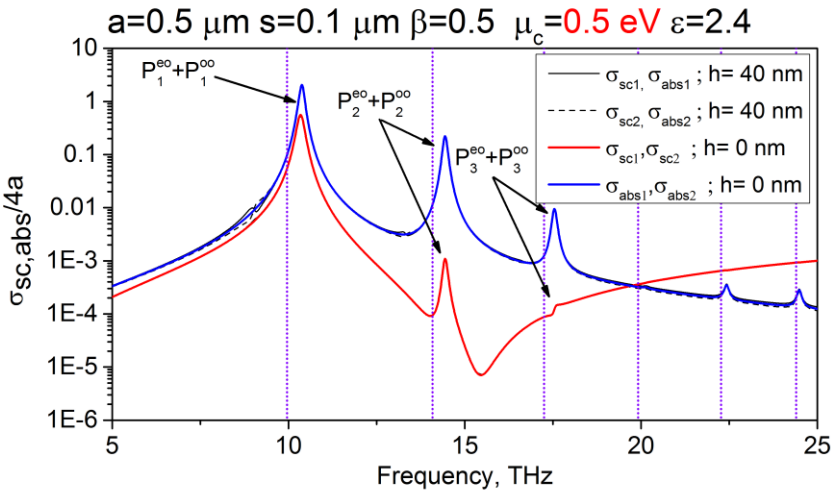

Fig. 4.3 Normalized partial SCS and ACS versus the frequency for twin dielectric nanowires covered with graphene with parameters as indicated and beam shifts h = 0 and 40 nm. Dotted vertical lines are the single-wire plasmon-mode frequencies, predicted by eq. (4.13)

As can be seen in Fig. 4.3, if the wire radius is a = 500 nm and graphene's chemical potential is μ_c = 0.5 eV, there are a few lower-frequency plasmon-mode resonances both in the scattering and in the absorption. However, they are almost the same both with and without the shift of the beam trajectory from the central-symmetric position, where it passes through the air-gap center. This means that the supermodes of twin-wire dimer that belong to the classes *EE* and *OE* ("dark" if the shift is absent) remain very weakly excited (see small bumps on the red side of (4.14), unlike their sister-modes of the *EO* and *OO* classes. The latter supermodes shine as one peak (i.e. are still unresolved) in both cases on the blue side of each frequency, predicted by (4.14). This unfavorable for the BPM design situation can be overcome if the Q-factors of the plasmon supermodes are made larger. Equations (4.15) and (4.13) tell that this can be achieved by either making the wire radius smaller or increasing the chemical potential of graphene, i.e. using a larger DC bias. This effect is accompanied with a frequency up-shift, see (4.14); this holds for the supermodes of each symmetry class.

While the fabrication of thinner wires seems to be realistic, the largest reported so

far value of graphene's chemical potential is only 1 eV (still, larger values can become realistic in future). Indeed, the computations made for a = 100 nm with μ_c = 0.5 eV and 1 eV (see the plots in Fig. 4.4 and Fig. 4.5, respectively), reveal the same but sharper resonances on the still unresolved mode doublets *EO-OO*, both in TSCS and ACS. However, now a shift of the beam trajectory triggers the excitation of new resonances on the unresolved mode doublets *EE-OE*, which remained "dark" if the beam was not shifted. Such resonances are associated with the "supermodes" of twin wires, whose symmetry is orthogonal to the beam field (1.2).

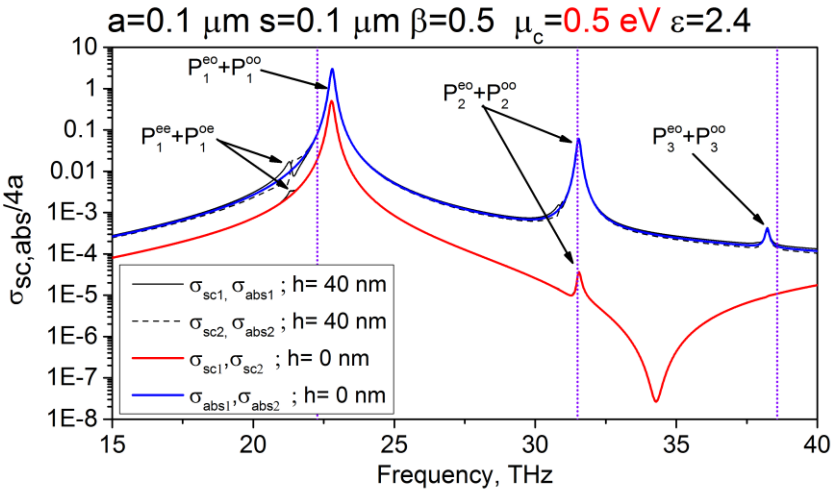

Fig. 4.4 The same as in Fig. 4.3 for the radius a = 0.1 μm.

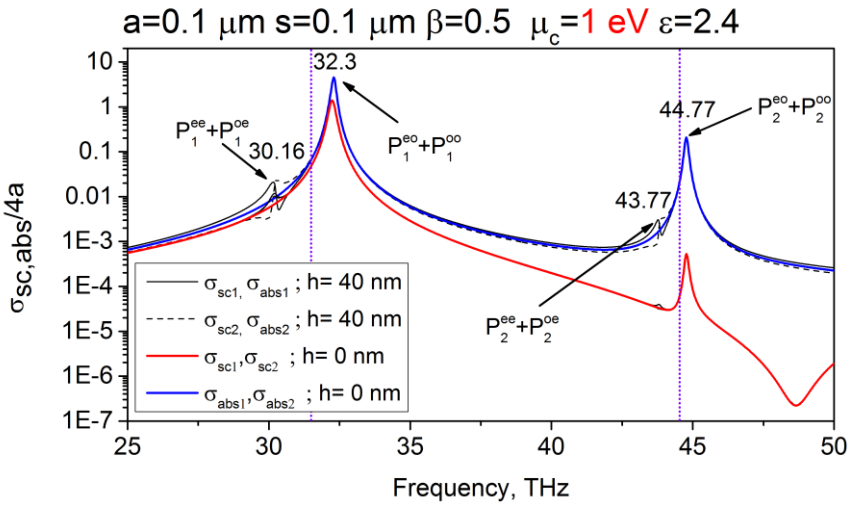

Fig. 4.5 The same as in Fig. 4.4 for the chemical potential μ_c=1 eV

This is exactly the same effect, which we are looking for, to be used in BPM design. Note that if a larger, say, 10 eV, chemical potential could be realized, then the mentioned new peaks become impressively larger and sharper (not shown here).

Earlier similar effect was found in the nanosize models of BPMs built on twin high-refractive-index dielectric wires in section 2.4 and twin silver nanotubes in section 3.3. Note that in those sections, the range corresponded to the visible-light frequencies while what we discuss here takes place at one order lower IR frequencies. Of course, in the covered circular dielectric wires, a modulated beam of particles can excite the resonances on the WG modes as well (slightly perturbed by the presence of graphene cover), however, for the wire radius taken here they become visible at the frequencies well above 100 THz.

For the BPM applications, it is interesting to know how the intensity of new resonances depends on the beam shift value. As seen in Fig. 4.6, the it is approximately proportional to the trajectory displacement.

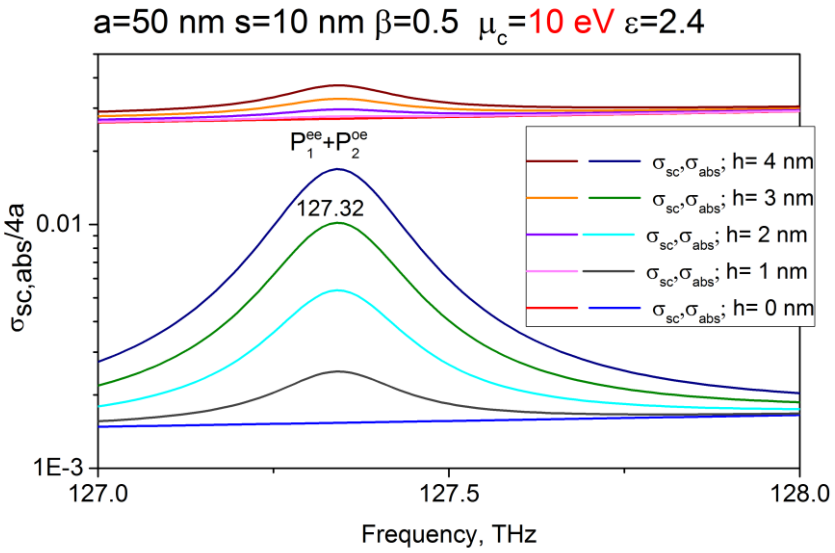

Fig. 4.6 Variation of the magnitude of new resonance on the beam displacement *h*

The near fields, computed in the peaks of TSCS in Fig. 4.5 for the case of the shifted beam trajectory, are shown in Fig. 4.7.

(a)
30.16 THz

(b)
32.3 THz

(c)
43.77 THz

(d)
44.77 THz

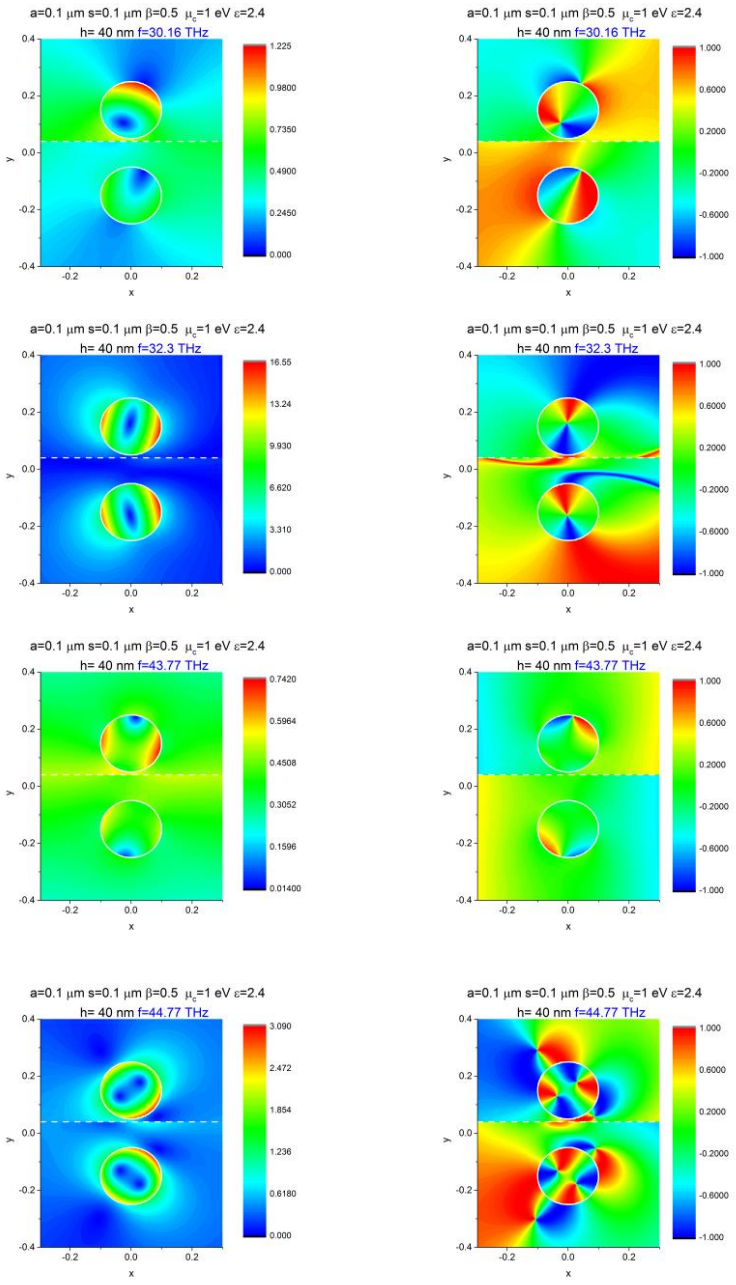

Fig. 4.7 In-resonance near magnetic field magnitude (left) and phase (right) patterns of twin dielectric nanowires covered with graphene with radius a = 0.1 μm, the chemical potential μ_c = 1 eV, beam shift h = 40 nm and air gap width s = 0.1 μm

Here, the left panel in each row corresponds to the field magnitude pattern while the right one corresponds to the field phase pattern. These patterns demonstrate the expected number of the field variations around the wires and support our interpretation of the plasmon-mode resonances as those associated with still unresolved supermode pairs of the *y*-even (*EE* and *OE*) and *y*-odd (*EO* and *OO*) classes of symmetry.

4.3 Finite array of graphene-coated nanowires: resonances on the lattice modes

4.3.1 DR effect for two in-line graphene-covered nanowires

This subsection is devoted to the analysis of the resonance effects in the DR from the same dimer PM made of circular dielectric nanowires coated with graphene, however, with a modulated electron beam moving above the wires.

This configuration is not promising for BPM, however, it is attractive as element of the other devices, where electron beams are exploited. Today, after almost a century of conventional particle accelerators, which have been important in fundamental physics and other applications, large attention is attracted to the co-called dielectric laser accelerators (DLA) [144, 145]. DLAs are micrometer-scale dielectric structures excited by external laser light sources. Due to modern nanofabrication techniques, they can be compact, inexpensive and still provide efficient acceleration due to high electric-field gradients [146]. These devices provide acceleration by using the intensive near fields of laser-driven periodic dielectric structures, i.e. gratings. Additionally, they can incorporate Bragg reflectors to eliminate the incident wave transmission through the grating. A promising material for the DLA is silicon, which has high dielectric permittivity ($\varepsilon \approx 12$) and good thermal conductivity. Besides, its nanofabrication infrastructure is well advanced as examined in [147].

Most popular DLA designs are based on various gratings of several hundred circular silicon nanorods [147,148]. They are less expensive and simpler than others and can be mass-produced using available nanofabrication methods. Consequently, electromagnetic analysis of such gratings is interesting and important.

For the DLA designing, it is crucial to have a high electric field gradient near the grating in the beam motion direction. On nanoscale, this can be achieved in the natural-mode resonances using the high-index materials like silicon. Still, there is an alternative: plasmon modes supported by the graphene-covered low-index scatterers. Therefore, we

chose the research configuration of two dielectric rods covered with graphene shown in Fig. 4.8, as a two-section element of a larger grating of DLA.

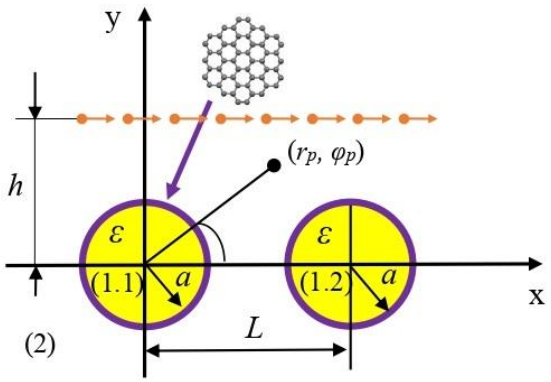

Fig. 4.8 Cross-sectional geometry of a dimer of in line graphene-covered circular dielectric nanowires, excited by a modulated electron beam moving above them

Fig. 4.8 presents the considered geometry of the DR problem. Identical dielectric nanowires hare relative permittivity ε, radius a, and the distance between their axes is L. The harmonically modulated, in density, beam of electrons flows at the distance h from the nanorod axes with the relative velocity $v = \beta c$ ($\beta < 1$). In Fig. 4.8, we explain the Cartesian and the local (r,φ) polar coordinates used in the derivations. The charge density of the beam as a sheet current flowing along the straight trajectory and the field of the electron beam are as in (1.1) and (1.2).

If we consider that the beam velocity is constant, then the DR analysis is reduced to the classical 2-D wave-scattering boundary-value problem, with (1.2) as the incident field. It includes the Helmholtz equation with the corresponding wavenumbers in partial domains, the graphene boundary conditions at the rod contours, the Sommerfeld radiation condition at infinity, and the condition of the local power finiteness. This set provides uniqueness of the DR problem solution. Then the basic equations are similar to the “BPM-like” graphene covered dielectric nanowires, however, with different right-hand part terms because of the different excitation,

$$x_m^{(p)} \pm \frac{V_m}{w_m D_m} \sum_{n=-\infty}^{+\infty} w_n H_{m-n}(kL) x_n^{(j)} = \frac{F_m^{(p)}}{w_m D_m}, m = 0, \pm 1, \pm 2, \ldots, \quad (4.26)$$

where

$$V_m = iZ^{-1} J_m' + J_m' \frac{\alpha J_m(k\alpha a)}{J_m'(k\alpha a)} - J_m, \quad (4.28)$$

$$D_m = iZ^{-1} H_m' + H_m' \frac{\alpha J_m(k\alpha a)}{J_m'(k\alpha a)} - H_m, \quad (4.29)$$

$$F_m^{(p)} = -iZ^{-1} g'^{(p)}_m - g'^{(p)}_m \frac{\alpha J_m(k\alpha a)}{J_m'(k\alpha a)} + g_m^{(p)}, \quad (4.30)$$

$$g_m^{(1,2)} = -Ae^{ikL(1\mp 1)/2\beta} e^{-qh} i^m J_m (1-\gamma)^m \beta^{-m+1}, \quad (4.31)$$

The scattering and absorption cross sections spectra in the infrared range for two distances between the nanorods are pictured in Fig. 4.9.

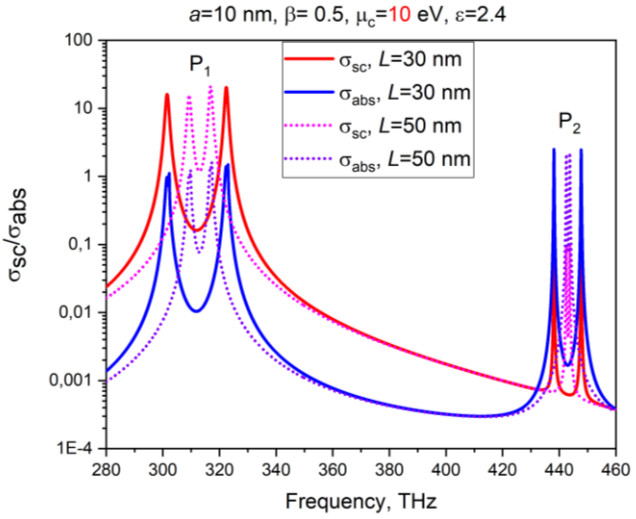

Fig. 4.9 The spectra of t TSCS and TACS for configuration in Fig 4.8. The wire radius is 10 nm, the beam velocity β is 0.5, the impact parameter is 5 nm, the chemical potential is 10 eV, the electron relaxation time is 1 ps, T = 300 K, the dielectric permittivity is 2.4, and the distance L is 30 nm and 50 nm

They show a number of the natural-mode resonances. We remind that the dimer

modes are conveniently called ‘supermodes’ as they are built on the modes of each circular graphene-covered rod, coupled in one of the four possible ways in the sense of symmetry or anti-symmetry. These quartets form two doublets of closely spaced supermodes – see also Chapter 5.

The presence of supermode quartets is revealed in Fig 4.10a, where the resonances decompose to four peaks, well visible on the zooms of ACS plots around the frequencies of the dipole supermodes P_1. In contrast, in Fig. 4.10b, where similar zooms around the frequencies of the quadrupole supermodes P_2 are shown, a split of the resonance peaks inside the doublets is not visible. This is caused by the smaller frequency separation of the P_2 supermodes in each doublet. As one can see, the change of the distance between the wires shifts the resonance frequencies. The larger the L, the closer the frequencies of all peaks to the frequency of the plasmon mode of the single circular wire covered with graphene.

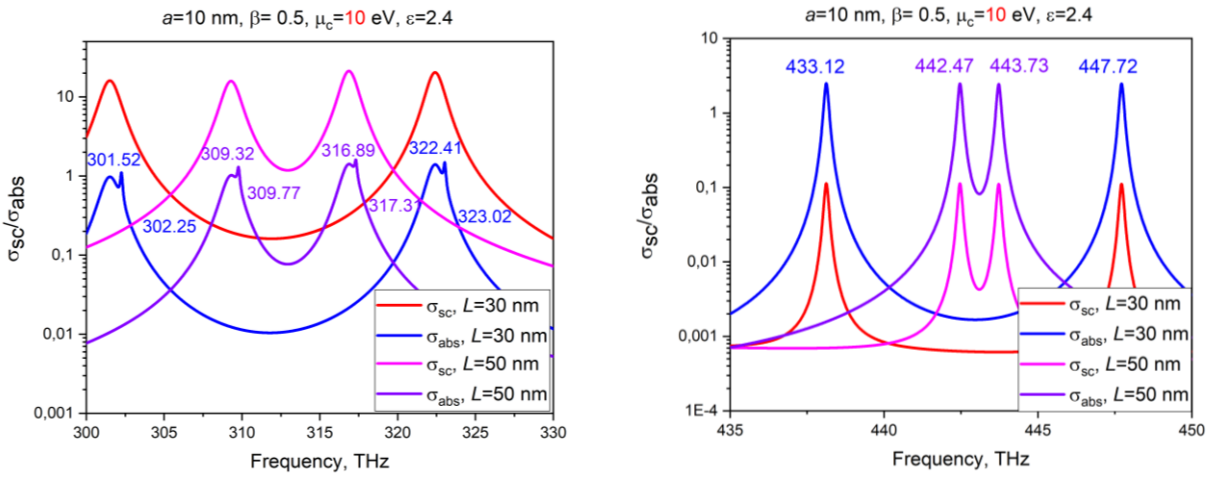

(a) (b)

Fig. 4.10 Zooms of the spectra of TSCS and ACS in Fig 4.8 around the P_1 (a) and P_2 (b) supermodes

In order to visualize the symmetry classes of the resonating supermodes, we present the near magnetic field patterns and the far field angular patterns of the

supermodes P_2, see Fig. 4.11.

One can see different orientation of the field maxima (red spots) that corresponds to different supermode symmetry classes. Each wire displays four bright spots of the field maxima. Here, only two of the possible four symmetry orientations appear due to unresolved resonances of the P_2 peaks.

Their Q-factors are not large enough to distinguish all symmetry classes. For the panel (a), the resonance is on the *x*-even/*y*-even P_2 supermode at the frequency of 433.12 THz. For the panel (b), the resonance is on the *x*-odd/*y*-odd P_2 supermode at 447.72 THz. Note that in-resonance field magnitude maxima are around 25 times larger than the magnetic-field maximum for the same beam in the free space. This enhancement can be exploited in DLA design. However, the field high values decay quickly off the rod boundaries as typical for the plasmon modes. The rate of decay is close to exponential near the boundary, however, transforms to $r^{-1/2}$ in the far zone.

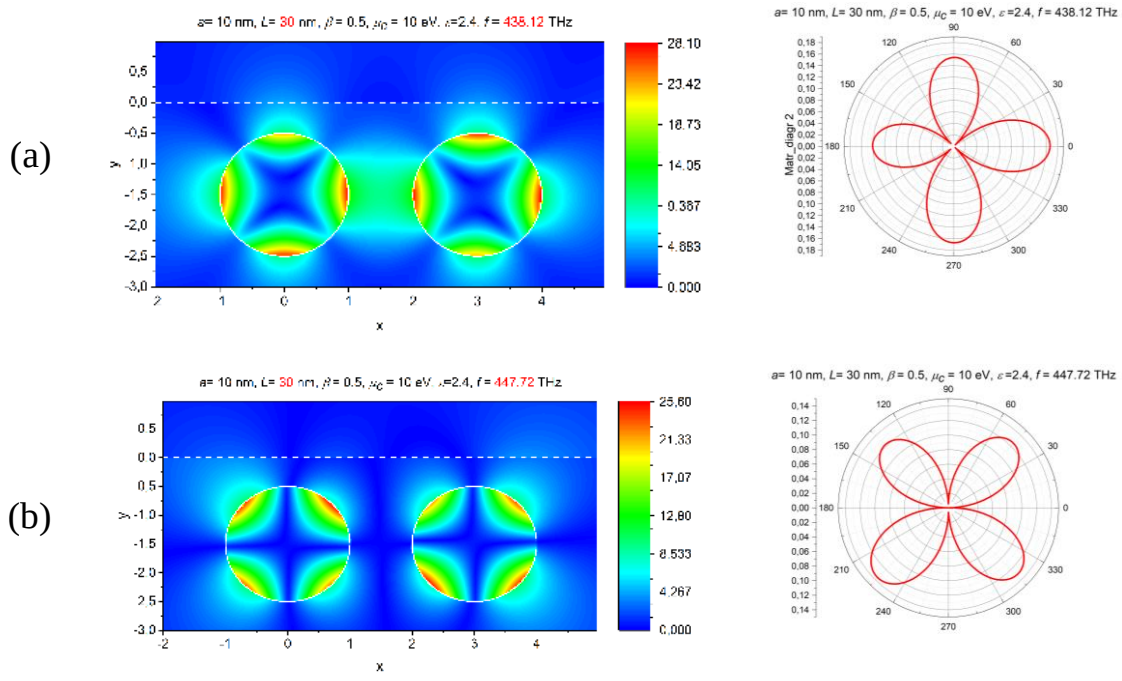

Fig. 4.11 Quadrupole supermode in-resonance near magnetic fields and far field patterns of graphene-covered wire dimer. The wire and beam parameters are the same as in Fig. 4.8, and the distance between the wires is 30 nm

4.3.2 DR effect for finite graphene-covered nanowire grating

The studied DR configuration is shown in Fig. 4.12. This is a finite-periodic array made of M identical circular dielectric wires covered with graphene. It is excited by the modulated electron beam field (1.2).

The DR problem formulation is similar to two-wire case studied in subsection 4.3.1. The final matrix equation has M x M block form and can be derived from the general case of Chapter 2. It belongs to the Fredholm second kind type.

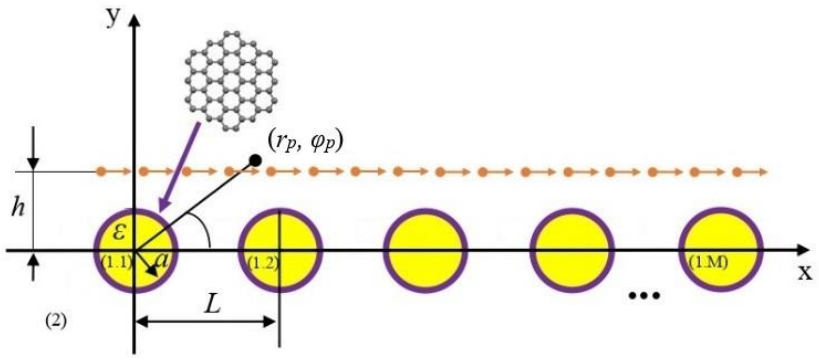

Fig. 4.12 Cross-sectional geometry of a grating of M circular dielectric nanowires coated with graphene and excited by a modulated electron beam

The IR-range spectra of TSCS associated with DR of the modulated electron beam with β = 0.5 and impact parameter h = 5 nm exciting the gratings made of 10, 50 and 100 graphene-covered nanowires are shown in Fig. 4.13. All the graphene and array parameters are indicated above the figure.

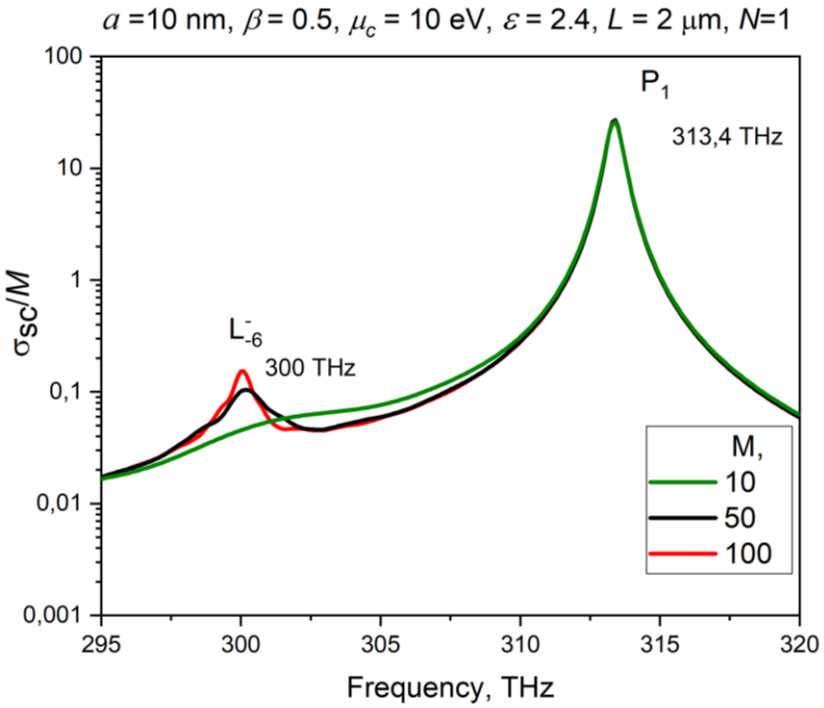

Fig. 4.13 The spectra of DR TSCS for the grating of M graphene-covered nanowire gratings excited by the modulated electron beam

Note that in this numerical example the grating period is L = 2 μm while the radius of wires is a = 10 nm, and the wavelength varies from 1.03 to 0.94 μm so that $a \ll L, \lambda$. From the comparison of the curves, computed with the block truncations numbers N_{tr} = 1 and 5 (not shown), it follows that 3 correct digits in TSCS of the 200-wavelength scatterer are obtained with account of only three multipoles, m = 0 and ±1.

The spectra demonstrate two natural-mode resonances. The most impressive resonance peak of TSCS is seen at 313.4 THz and easily identified as associated to the transversal "dipole-type" (of the azimuthal index m =1) plasmon mode of the circular graphene cover of each individual nanowire. Indeed, the plasmon-mode P_1 frequencies are given by (4.14), that yields 315 THz. In the considered case of nanowire grating, where we have M optically coupled wires, the plasmon supermodes form 2M-multiplets. However, as $a \ll L, \lambda$, the separation between the supermodes, in frequency, is extremely small. This is the reason that only one such peak is visible in Fig. 4.13. Note

that the magnitude of this peak, if normalized by *M*, does not depend on the number of wires (all the curves overlap completely).

The other resonance peak is found at 300 THz and shows opposite dynamics – both its magnitude and sharpness strongly depend on *M*. The nature of this resonance is revealed after plotting the far-field angular DR pattern – see Fig. 4.14(a).

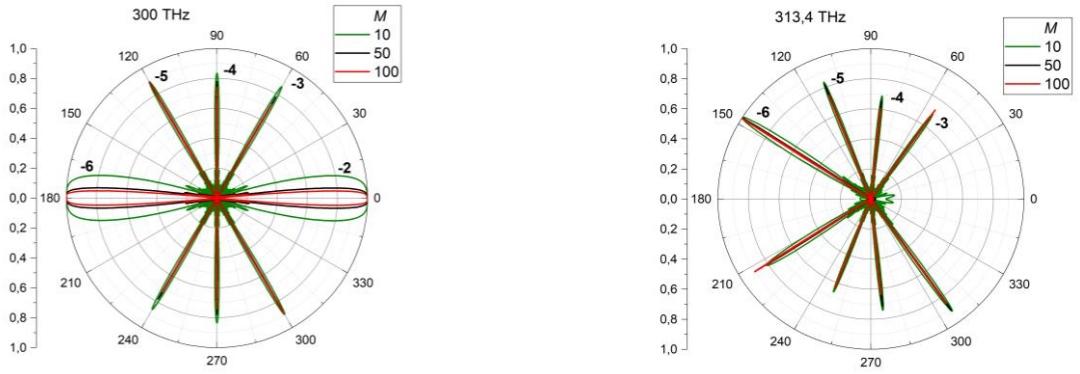

(a) (b)

Fig. 4.14 The far-field patterns of DR for the gratings of *M* graphene-covered nanowires excited by the modulated electron beam at the resonance frequencies of 300 THz (a) and 313.4 THz (b)

They demonstrate two narrow lobes in the grazing directions, 0 and 180° and three even narrower lobes of DR in each half-space. These DR lobes are easily identified as corresponding to the directions of the radiation of the Floquet field harmonics of the corresponding infinite grating of the same period. Indeed, those directions are given by the equations [2-4],

$$\cos\alpha_n = n\lambda / L + 1/\beta,\ \ n = 0, \pm 1, \pm 2, \ldots \qquad (4.24)$$

that yields $\alpha_{-2}=1^o, \alpha_{-3}=61^o, \alpha_{-4}=90^o, \alpha_{-5}=118^o$. As could be expected, all lobes get sharper with larger *M*. Additionally, $\cos\alpha_{-6}=1.031>1$ that means that in the infinite grating -6-th harmonic is just below cut-off. Indeed, if *M* gets larger, then this lobe gets narrower and disappears. Now, note that the -2-nd harmonic is just above the cut-off. This means that the frequency of the *M*-dependent resonance is very close to the *Rayleigh Anomalies* (RA) of the -2-nd and -6-th order. Recalling that according to [131, 136, 137] there exist a lattice-mode pole just below each RA frequency, we can conclude that the first resonance in Fig. 4.13 is associated with the lattice mode. On finite gratings, these resonances also exist and their Q-factors raise if the number *M* gets larger – see, e.g. [136, 137]. The DR patterns in Fig. 4.14(b) correspond to the plasmon mode resonance, the frequency of which is far from any RA frequency.

Then we investigate the influence of the wire radius by choosing *a* =10, 50 ,100 nm for the *M* =100 grating. Figs. 4.15 and 4.16 present the per-wire TSCS in the broad frequency range where we can identify plasmon modes denoted as P_m and lattice modes denoted as L_m (close to the RA frequencies).

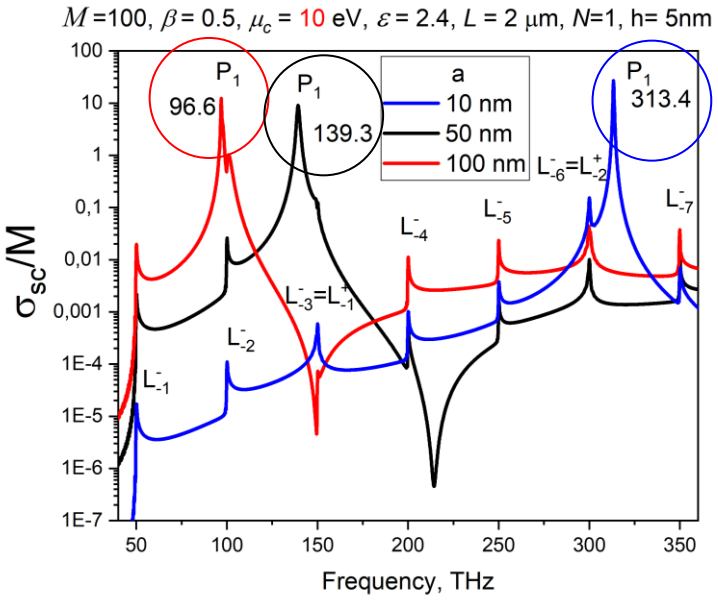

Fig. 4.15 The spectra of DR TSCS for the grating of *M*=100 graphene-covered dielectric nanowire gratings excited by the modulated electron beam for three radii *a*=10 nm, 50 nm and 100 nm and the chemical potential μ_c = 10 eV

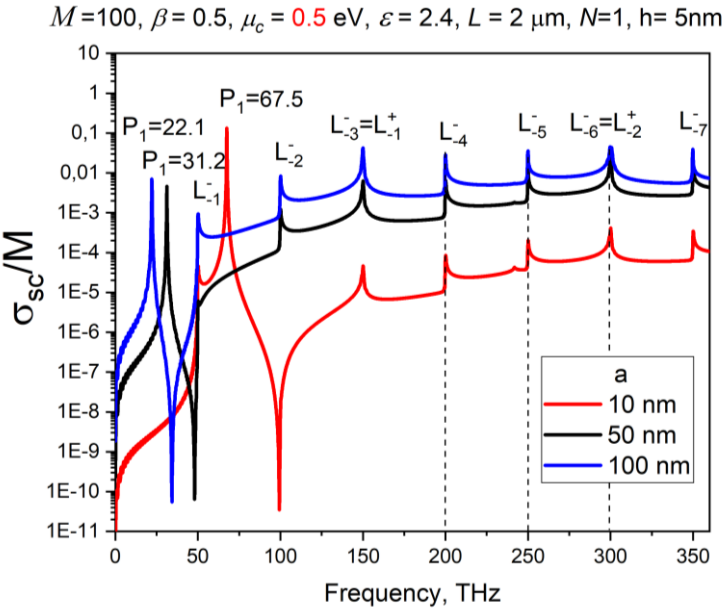

Fig. 4.16 The same as Fig. 4.15 for the chemical potential $\mu_c = 0.5$ eV

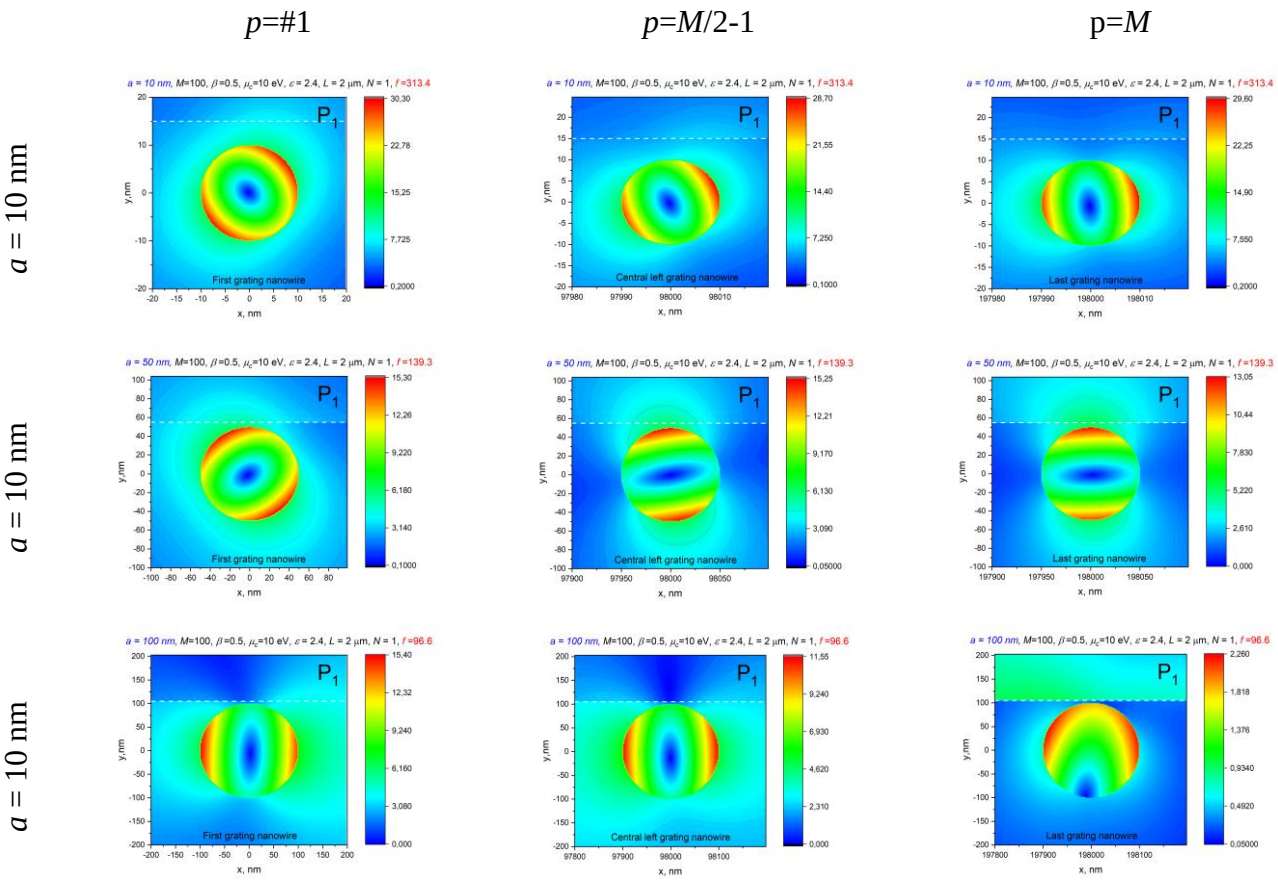

Fig. 4.17 The near magnetic field patterns in the P_1 plasmon-mode resonances marked in for Fig. 4.15, near the first, the central-left and the last wires

In Fig. 4.17, we present the near magnetic field patterns for the grating of Fig. 4.12, in the resonance on the P_1 mode, near the first, the central-left and the last nanowire. The P_1 pattern is better visible in the case of the smallest wire radius, because here the Q-factor of P_1 is the largest.

Conclusions to Chapter 4

- We have analyzed, using a dedicated numerical code based on the reduction of the DR problem to the matrix equation having guaranteed convergence, the 2-D model of BPM designed of twin graphene-coated circular dielectric nanowires. This analysis has demonstrated that such a dimer can serve as an infrared-range sensor of the beam shift from the prescribed trajectory. If such a shift appears, then new resonances on the formerly “dark” supermodes start shining in the spectral dependence of the diffraction radiation. To have these new peaks well resolved, the graphene chemical potential should be rather high, around or above 0.5 eV. Such high values that can be achieved with appropriate DC biasing.

- Besides, we have presented basic equations and sample numerical results for the DR from two in-line dielectric circular nanowires with graphene covers exited by the modulated electron beam. The resonances on the plasmon supermodes of different symmetries have been discussed. This analysis can be useful in the design of DLA sections made of low-index dielectrics, however, covered with graphene.

- Moreover, we have demonstrated two types of resonance effects in the DR of a modulated electron beam flowing over a sparse finite grating of $M >> 1$ circular dielectric nanowires with graphene covers. Namely, the resonances on the plasmon modes of each wire and on the lattice modes of the whole grating have been discussed. This investigation can be helpful in the design of DLA sections based on dielectric elements covered with graphene.

CHAPTER 5 THRESHOLD CONDITIONS FOR SINGLE AND TWIN GRAPHENE-COVERED QUANTUM NANOWIRE LASERS

This chapter is dedicated to the implementation of the Lasing Eigenvalue Problem (LEP) approach for study of the electromagnetic field in the presence of a circular *quantum wire* (QW) made of a gain material and wrapped in graphene cover and a dimer of two identical graphene-covered QWs, at the threshold of stationary emission. As explained in section 1.6, LEP delivers the mode-specific eigenvalue pairs, namely the frequencies and the threshold values of the QW gain index for the plasmon and the wire modes of such nanolasers. In our analysis, we use quantum Kubo formalism for the graphene conductivity and classical Maxwell boundary-value problem for the field functions. The materials of Chapter 5 have been published in works [A1, A10, A12, A14].

The goal of this chapter to study the plasmon and non-plasmon mode threshold conditions of the nanolasers made of a circular QW covered with graphene and a pair of such QWs (see Fig. 5.1).

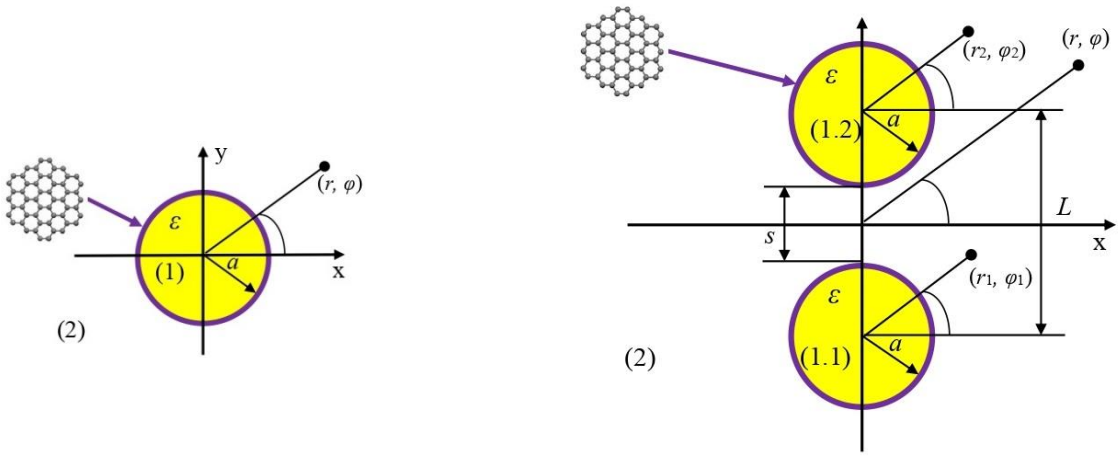

(a) (b)

Fig. 5.1 Cross-sectional geometry of a single (a) and a dimer (b) of identical gain-material circular nanowires with graphene covers and the notations used

Besides, we plan to investigate their dependences on the QW and graphene parameters. Our instrument is the LEP approach [149] (see also section 1.6), which has been already applied to several types of microlasers in [111, 150, 151] and silver nanostrip and nanotube plasmonic lasers in [152,153]. LEP is a full-wave semi-classical electromagnetics eigenvalue problem, tailored to extract the mode-specific wavelengths, together with the associated threshold material gain values, of not attenuating in time emission. Complete mathematical grounding of LEP can be found in [154].

Note that the laser configuration in Fig. 5.1 (a) was considered recently in [155] using essentially a LEP-like approach, namely, looking for the conditions that turn the imaginary part of the natural frequency of the plasmon mode P_1 to zero.

5.1 Modes of single graphene-coated quantum nanowire laser

5.1.1 Lasing Eigenvalue Problem statement

Consider a single-wire laser, the active region of which is a graphene-covered circular QW, as shown in Fig. 5.1a, in the free space. We denote the radius of QW as a and assign the indices 1 and 2 to the inner ($r < a$) and outer ($r > a$) domains of QW, respectively.

We assume that the wire is infinite along the z-axis and that the electromagnetic field does not depend on z, with time dependence $e^{-i\omega t}$, where the frequency is real, $\omega = \mathrm{Re}\,\omega$. Thanks to this, we consider a 2-D problem in the plane of the wire cross section, where we introduce the polar coordinates, (r,φ). As graphene is known to support the H-polarized plasmon modes, we consider only this case. Here, the electric and magnetic fields have components $\mathbf{E} = (E_r, E_\varphi, 0)$ and $\mathbf{H} = (0,0,H_z)$, respectively. Our goal is to study the conditions, under which non-zero time-harmonic EM field can exist in such configuration, in the absence of the incident field.

The function $H_z(r,\varphi)$ must satisfy the Helmholtz equation, $\left(\Delta + k_{1,2}^2\right) H_z(r,\varphi) = 0$

outside the QW boundary $(r \neq a)$, with the wavenumbers $k_1 = k\nu$ and $k_2 = k$, where $k = \omega / c$ and the QW material as nonmagnetic, so that its dielectric constant is connected to the refractive index ν as $\varepsilon = \nu^2$. At the graphene-covered QW boundary, the field function must satisfy the same "resistive" boundary conditions as in section 4.1,

$$E_\varphi^{int} = E_\varphi^{ext}, \quad E_\varphi^{int} + E_\varphi^{ext} = 2ZZ_0(H_z^{int} - H_z^{ext}), \quad r = a, \tag{5.1}$$

where Z is the surface impedance of graphene, normalized by the free-space impedance Z_0; it has the following form: $Z = (\sigma Z_0)^{-1}$, with σ being the complex surface conductivity. Besides, thanks to real k, the field function must satisfy the Sommerfeld radiation condition at infinity, and, additionally, the condition of the local field power finiteness. Note also that $E_\varphi^{int,ext} = \left(Z_0 / ik\varepsilon_{1,2}\right)\partial H_z^{int,ext} / \partial r$, from the Maxwell equations.

We consider the complex refractive index of the QW gain material to be $\nu = \alpha - i\gamma$, where α is known refractive index and $\gamma > 0$ is unknown threshold gain index. For simplicity, we will also assume that the material gain is uniformly distributed throughout the QW and does not depend on the frequency. In real life, such a QW can be a glass-like material doped with erbium ions, to provide the gain in the infrared range. In the sub-THz range, similar properties are known for the andalusite crystalline material doped with iron.

Mathematically, within the LEP we look for such pairs of real numbers (k_s, γ_s) that generate non-zero functions $\{\mathbf{E}_s, \mathbf{H}_s\}$ (s = 1,2, …), which solve the formulated above boundary-value problem for the Maxwell equations. That is, we look for the frequencies and gain-index thresholds of laser modes as eigenvalue pairs. It is worth to note that the other LEP-like formulations exist, see [113-117], where the threshold gain is characterized with $\mathrm{Im}\,\varepsilon < 0$ instead of γ or with the product, $g = k\gamma$. The graphene's conductivity has been discussed in section 1.4 and will be used in the further analysi.

5.1.2 Characteristic equations for the single-wire modes

The magnetic field inside and outside the wire can be expanded as Fourier series in the angular exponents, taking into account the radiation condition at infinity and condition of local field power finiteness near the center of wire,

$$H_z^{int,ext}(r,\varphi)=\sum_{m=0(1)}^{\infty}\begin{Bmatrix} x_m J_m(\nu kr),\ r<a \\ y_m H_m(kr),\ r>a \end{Bmatrix}\cos(m\varphi)\ or\ \sin(m\varphi), \tag{5.2}$$

where x_m and y_m are unknown coefficients, while $J_m(.)$ and $H_m(.)$ are the Bessel and the Hankel 1-st kind cylindrical functions, respectively. The orthogonality and completeness of the set of functions $\cos/\sin(m\varphi),\ m=(0),1,2,...$ on the circle allow us to apply the conditions (5.1) in term-by-term manner.

Thus, the separation of variables leads to splitting of the modes into independent orthogonal families by the azimuthal index *m*, and all modes with $m > 0$ are double degenerate.

After some algebra, independent full-wave transcendental equations for the modes of each index, $m = 0,1,2...$, can be written as

$$D_m(k,\gamma;a,\alpha,Z)=J_m'(k\nu a)H_m'(ka)+iZ\left[J_m'(k\nu a)H_m(ka)-\nu J_m(k\nu a)H_m'(ka)\right]=0, \tag{5.3}$$

Note that if $Z=0$ or $|Z|\to\infty$, then, respectively, (5.3) turns to the characteristic equation for the modes of the circular cavity with PEC wall or the circular dielectric rod in the free space.

We emphasize that the complex calculus theorems guarantee that the roots of (5.3) are discrete on the plane (k,γ). Besides, each of them is a continuous function of *a*, α and *Z* and cannot appear or disappear on that plane except at $k = 0$ and infinity.

It is interesting that those roots of (5.3) that correspond to the plasmon modes can be determined analytically, at least in the frequency domain where the intraband conductivity, σ_{intra}, dominates over the interband conductivity, σ_{inter} (see section 1.4).

In this domain, σ_{inter} can be neglected, and the normalized surface impedance (or resistivity) of graphene takes the form,

$$Z(\omega) \approx \left(Z_0 \sigma_{\text{intra}}\right)^{-1} = \left(1/\tau - i\omega\right)\Omega^{-1}, \tag{5.4}$$

where Ω is given by equation (4.13).

Now, we can consider the circular graphene shell as a traveling wave resonator, which supports the transversal plasmon modes (similarly to silver nanotube plasmon modes [95]). Then, neglecting the curvature of the shell, and hence the radiation losses, approximate characteristic equation for these modes is

$$g_{plas} a = m, \;\; m = 1, 2, \ldots \tag{5.5}$$

where g_{plas} is the propagation constant (eigen-wavenumber) of the plasmon guided wave on the infinite flat graphene monolayer placed between two dielectrics, known in the analytical form from [156]. Namely, if $|Z| >> 1$, then

$$g_{plas} \approx ik(\varepsilon + 1)Z + O(1) \tag{5.6}$$

On substituting (5.6) and (5.4) into (5.5), a complex-valued equation is obtained,

$$ika(\varepsilon + 1)Z(k, \gamma) + O(1) = m, \;\; m = 1, 2, \ldots \tag{5.7}$$

which can be solved analytically in the same approximation. Interestingly, equation

(5.7) also follows from (5.3) if $ka << 1$ and $|k\nu a| << 1$ [159]. The real part of this equation allows to find approximate expression for the emission frequencies of the transversal plasmon modes of the closed graphene shell, which covers circular QW,

$$k_m^P \approx \left[\frac{m\Omega}{a(\alpha^2+1)c} \right]^{1/2} \tag{5.8}$$

Note that this value is the same as the real part of the complex eigenfrequency in the analysis of natural modes of the passive graphene-covered circular dielectric wire (section 4.1).

One can see that in the considered approximation, the emission frequencies do not depend of the electron relaxation time and are proportional to the square-roots of the chemical potential of graphene (if $\mu_c >> k_B T$) and inverse QW radius. This opens up the possibility of developing a laser that is continuously tuned in a fairly wide range of frequencies.

Furthermore, the imaginary part of the same equation delivers the threshold values of the gain index,

$$\gamma_m^P \approx \frac{\left(\alpha^2+1\right)^{3/2}}{2\alpha} \left(\frac{a}{m\Omega c} \right)^{1/2} \frac{1}{\tau} \tag{5.9}$$

Thus, the lasing thresholds of the plasmon modes are inversely proportional to the electron relaxation time and the square roots of the mode azimuth index and the chemical potential (if $\mu_c >> k_B T$). Besides, they scale down as the square root of the wire radius, although one should keep in mind that (5.8) is derived neglecting the radiation losses of the plasmons.

Interestingly, frequently used in the laser physics quantity of the product of (5.8) and (5.9), which is the gain per wavelength, does not depend, in the considered

approximation, on the QW radius, graphene chemical potential and mode index,

$$k_m^P \cdot \gamma_m^P \approx \frac{\alpha^2+1}{2\alpha c\tau} \quad \text{or} \quad k_m^P \cdot (\mathrm{Im}\,\varepsilon)_m^P \approx \frac{\mathrm{Re}\,\varepsilon+1}{c\tau} \tag{5.10}$$

Therefore, within this approximation, all plasmon modes under any variations of the mentioned parameters stay at the same hyperbolic trajectory, $k = C(\alpha,\tau)\cdot\gamma^{-1}$, which is controlled only by the electron relaxation time, τ, and wire refractive index, α. This feature is, obviously, the consequence of the fact that the simplified Kubo expression for graphene's surface impedance (5.4) suggests that both its real and imaginary parts are proportional to $\Omega(\mu_c,T)$, hence their ratio scales as $\omega\tau$.

5.1.3 Full-wave analysis of single-wire laser mode properties

In this subsection, we present the results of numerical study of the LEP eigenpairs for the single-QW graphene-coated laser using the full-wave equations (5.3) and full Kubo conductivity (1.3) - (1.5). In Fig. 5.2, the lasing frequencies and thresholds are shown versus the wire radius, which varies from 50 nm to 100 μm, at μ_c = 0.25 eV, τ = 0.5 ps and α = 1.55. One can see that the plasmon modes have lower frequencies and thresholds than the first QW modes H_{01} and H_{11} provided that the QW radius is smaller than 10 μm, while in thicker wires they become comparable.

The based on the Drude term approximations (5.7) and (5.8) for k_m^P and γ_m^P are also shown by the dotted curves in Fig. 1.3. Note that they are in very good agreement with full-wave computations of the roots of (5.3), performed by the iterative root-search method, where (5.7) and (5.8) are the initial-guess values. As expected, the agreement worsens at low frequencies where $|Z|$ gets so small that the radiation losses become comparable to the ohmic losses and at very high frequencies where the contribution of the interband conductivity cannot be neglected.

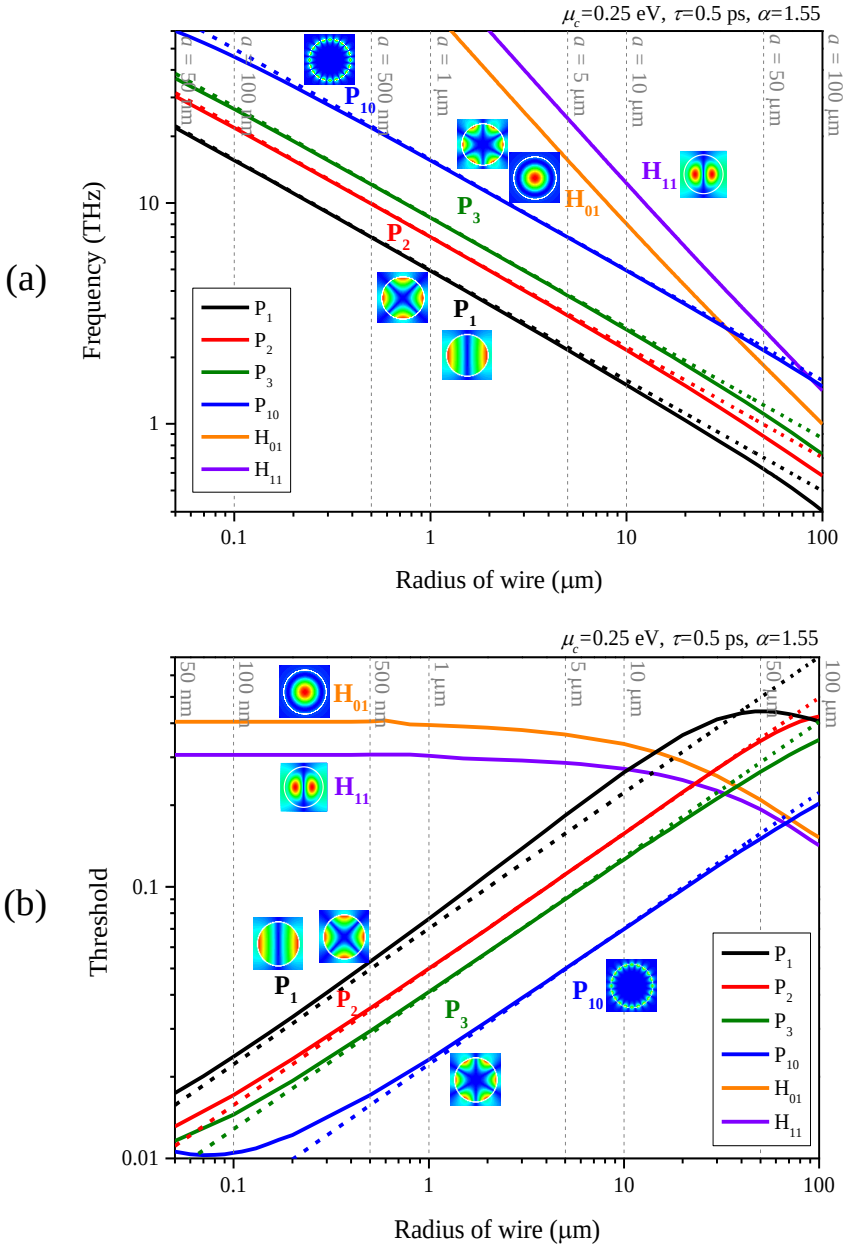

Fig. 5.2 Frequencies and thresholds versus the wire radius a for the plasmon modes P_1, P_2, P_3 and P_{10} and the perturbed dielectric wire modes H_{01} and H_{11} for the single-wire laser with parameters of graphene μ_c = 0.25 eV, τ = 0.5 ps and α = 1.55

Further, to make clearer the comparison of the lasing conditions, we plot the trajectories of the modes, considered in Fig. 5.2, on the plane (f, γ), where $f = kc/2\gamma$, under the variation of the chemical potential of graphene (Fig. 5.3), electron relaxation time (Fig. 5.4), and QW refractive index (Fig. 5.5).

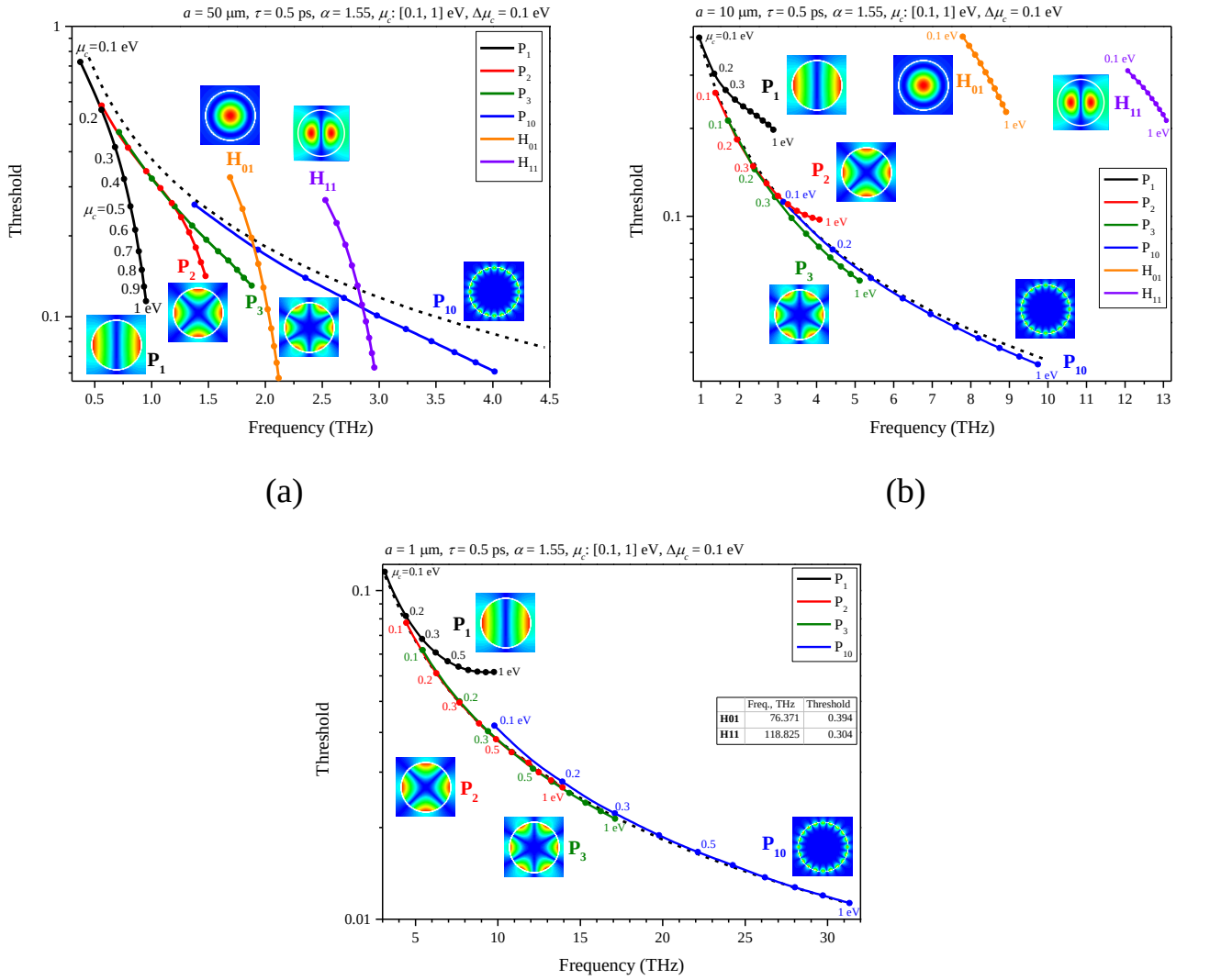

Fig. 5.3 Trajectories of the plasmon modes P_m and perturbed dielectric wire modes H_{nm} of the single-wire laser with parameters a = 50 μm (a), 10 μm (b) and 1 μm (c), under the variation of the chemical potential of graphene. Other parameters are as marked

Here, we choose the wire radius to be 50 μm, 10 μm and 1 μm and assume that the QW gain material refractive index and the graphene parameters are as indicated in figures. We emphasize that these trajectories have been computed from the full-wave transcendental equations (5.3) and full Kubo expressions (1.3)-(1.5) for several values of the azimuth index m. For comparison, the trajectories based on approximations (5.8) and (5.9) are also presented as dashed lines.

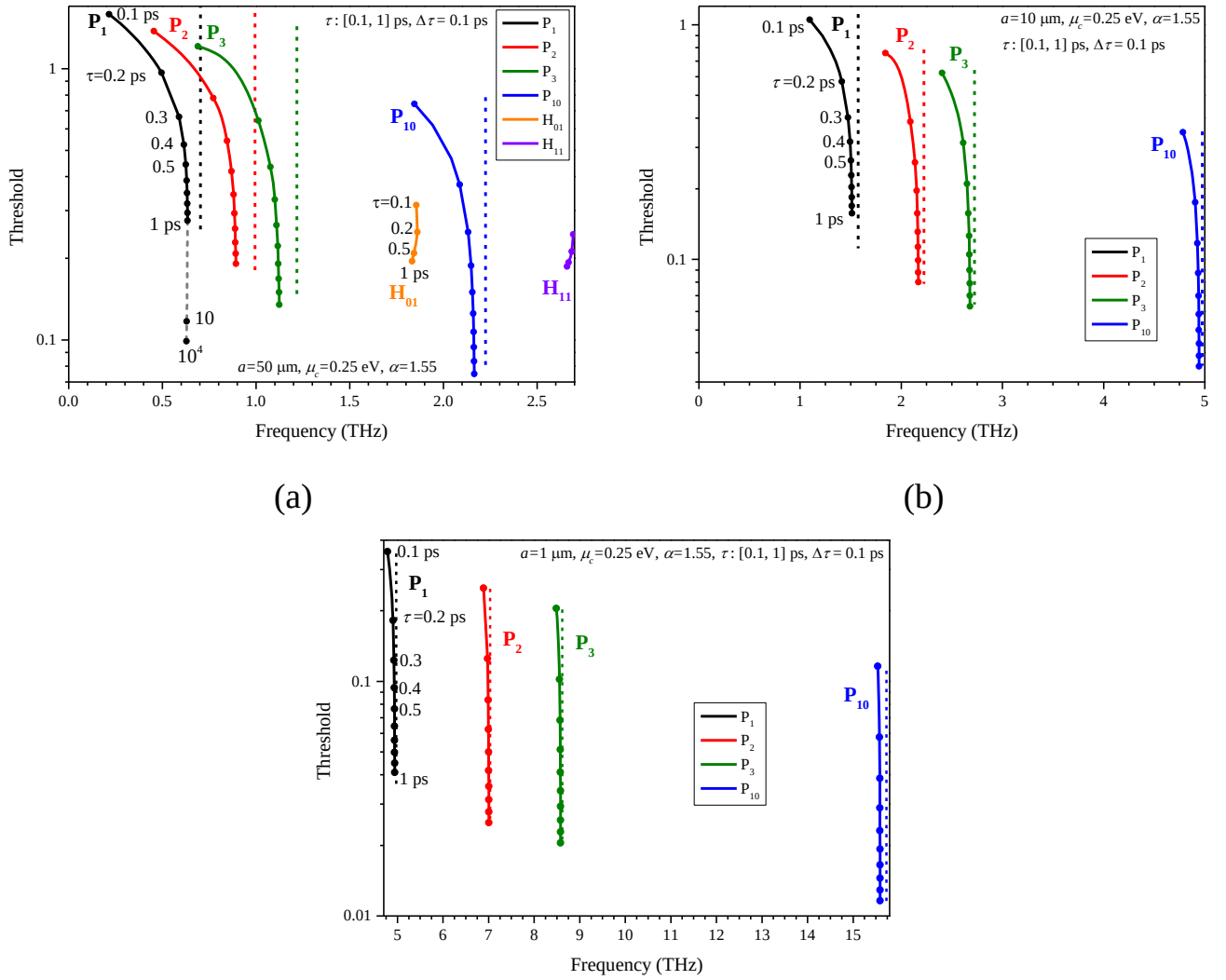

Fig. 5.4 Trajectories of the plasmon modes P_m and wire modes H_{nm} of the single-wire laser with parameters a = 50 μm (a), 10 μm (b) and 1 μm (c), under the variation of the electron relaxation time. Other parameters are as marked

As one can see, only the plasmon-mode frequencies are well tunable using the graphene chemical potential. Making the wire thinner than 10 μm shifts QW modes far to the blue side of spectrum. The larger the τ, the lower the thresholds of all modes; note that if τ varies from realistic 1 ps to fantastic 10 μs (marked by arrow), then the P_1 threshold is almost stable that points out to the possible radiation loss level. Again, the approximations of (5.8) and (5.9), given by the dashed curves, are amazingly accurate except of the low-terahertz and higher than 35 THz frequencies.

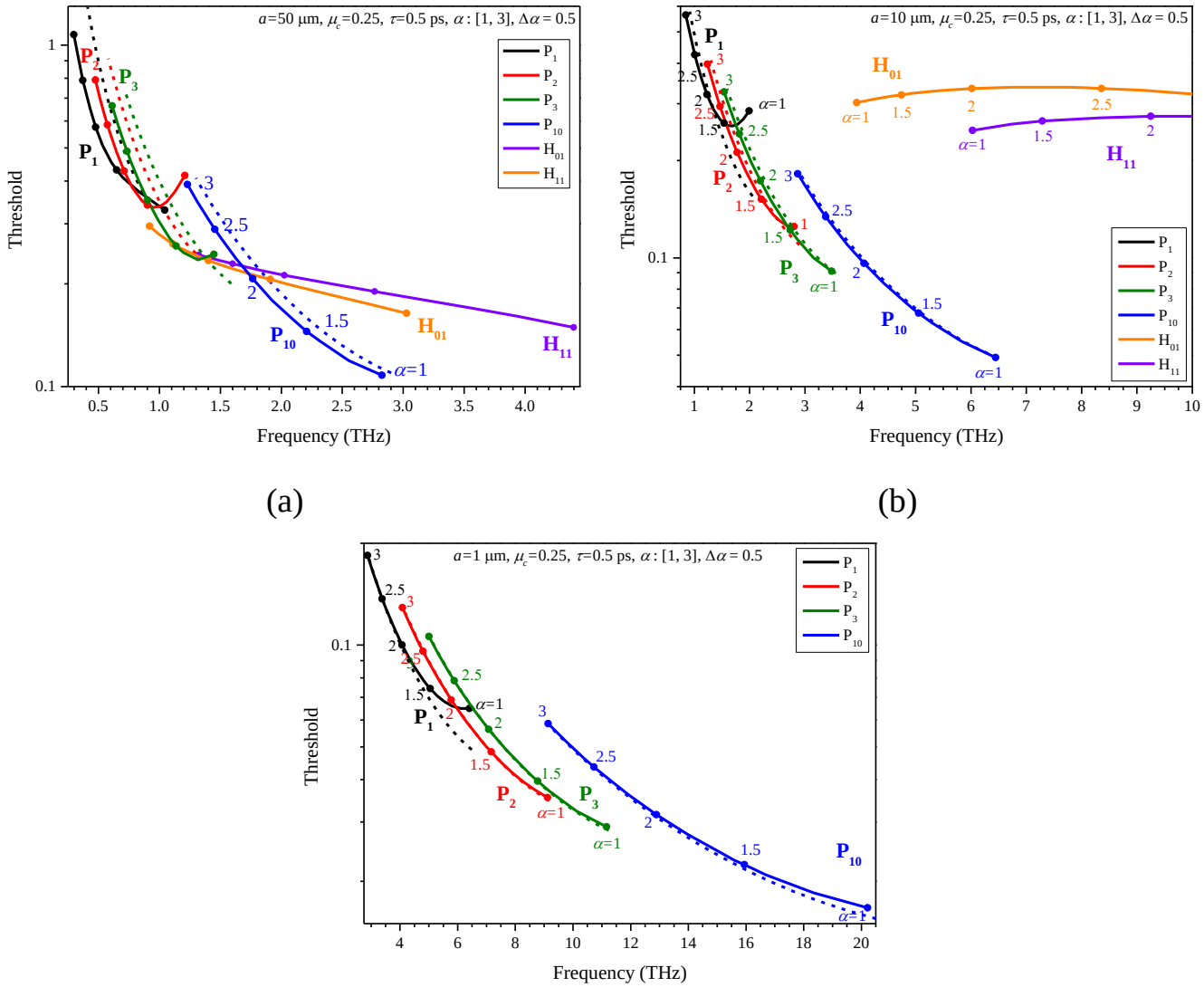

Fig. 5.5 Trajectories of plasmon modes P_m and wire modes H_{nm} of the single-wire laser with radii a = 50 μm (a), 10 μm (b) and 1 μm (c), under the variation of the refractive index of QW. Other parameters are as marked

5.2 Supermodes of twin graphene-coated quantum nanowire laser

In this section, we present the results of full-wave numerical analysis of the lasing frequencies and thresholds of the dimer laser supermodes.

In the case of dimer as it is shown in Fig. 5.1 (b), we introduce the global Cartesian and polar coordinates, with the origins at the midpoint between QW axes so

that $\vec{r} = (x, y) = (r, \varphi)$, where $x = r\cos\varphi$, $y = r\sin\varphi$, and two local CS with the origins at the wire axes. Then, the associated LEP formulation is similar to single-wire case, with the conditions (5.1) imposed at each wire's boundary, $r_j = a$ (j = 1,2). Important circumstance is that the dimer-wire configuration has two lines of symmetry, that is the x and y axes.

5.2.1 Full-wave determinantal equations of four symmetry classes of dimer supermodes

As if has been discussed in Chapter 4, in the dimer case all eigenmodes are in fact "supermodes," built on the modes of each individual circular wire and optically connected in four possible ways dictated by the two-fold symmetry. Hence, supermodes make quartets instead of pairs because each mode of a stand-alone circular wire is doubly degenerate; this degeneracy is lifted when another circular wire appears. Only the supermodes built of axially symmetric modes of each wire make doublets. Each family of supermodes has either the symmetry or the anti-symmetry of its field with respect to each line of symmetry; they can be conveniently denoted as "x-even, y-even" (EE), "x-even, y-odd" (EO), "x-odd, y-odd" (OO), and "x-odd, y-even" (OE). The "even/odd" conditions, respectively, can be expressed as

$$\frac{\partial H_z}{\partial x} = 0 \text{ at } y = 0 \text{ or } \frac{\partial H_z}{\partial y} = 0 \text{ at } x = 0; H_z = 0 \text{ at } y = 0 \text{ or } x = 0 \qquad (5.11)$$

To reduce the dimer LEP to determinantal characteristic equations, we follow the same approach as in section 4.3 and use the Fourier expansions of the field function in the local polar coordinates, the addition theorems for the cylindrical functions, and the conditions (5.11). Here, we look for the magnetic field function as

$$H_z = \begin{cases} H_z^{int(j)}, & r_j \in (1.j), \quad j = 1,2, \\ H_z^{ext}, & r_j \in (2), \end{cases} \tag{5.12}$$

It is convenient to introduce new variables $\psi_j = \phi_j + \pi/2$. Then the internal and external fields, which have the *y*-even and *y*-odd symmetry can be expanded as follows:

$$H^{\text{int}(j)}(r,\psi) = \sum_{n=0}^{\infty} y_n^{(j)} J_n(k\alpha r_j) S_n^{+}(\psi_j), \quad j = 1,2, \tag{5.13}$$

$$H^{ext}(r,\psi) = \sum_{j=1,2} \sum_{n=0}^{\infty} z_n^{(j)} H_n(kr_j) S_n^{\pm}(\psi_j), \tag{5.14}$$

where we use the following notations: $S_m^{+}(\psi) = \cos m\psi$ and $S_m^{-}(\psi) = \sin m\psi$, $J_n(\cdot)$ and $H_n(\cdot)$ are the Bessel and Hankel (first kind) functions, and $y_n^{(1,2)}$ and $z_n^{(1,2)}$ are unknown coefficients to be found. This representation of the function *H* satisfies the Helmholtz equation, the Sommerfeld radiation condition, the local power finiteness condition, and the *y*-even/*y*-odd symmetry conditions that is (5.11) at $x = 0$.

On substituting (5.13) and (5.14) into the graphene boundary conditions (5.1), using the Graph addition theorem for the Hankel functions, and introducing the notations,

$$I = \left\{\delta_{mn}\right\}_{m,n=0(1)}^{\infty}, \quad A^{E/O,E(O)} = \left\{A_{mn}^{E/O,E(O)}\right\}_{m,n=0(1)}^{\infty}, \tag{5.15}$$

$$X_{1,2}^{E/0,E(O)} = \left\{x_n^{(1,2)}\right\}_{n=0(1)}^{\infty}, \tag{5.16}$$

$$x_n^{(1,2)} = z_n^{(1,2)} w_n^{-1}, \quad w_n = n!(2/ka)^n \tag{5.17}$$

where δ_{mn} is the Kroenecker symbol, we exclude the unknowns $X_2^{(pq)}$ because from (5.11) it follows that

$$X_1^{E/O,E} = \pm X_2^{E/O,E},\ X_1^{E/O,O} = \mp X_2^{E/O,O} \tag{5.18}$$

and obtain the following four matrix equations for $X_1^{(pq)}$:

x-even/y-even (EE) and x-odd/y-even (OE) mode classes,

$$\left(I + A^{E/O,E}\right) X_1^{E/O,E} = 0, \tag{5.19}$$

$$A_{mn}^{E/O,E} = \pm \mu_n V_m w_m^{-1} D_m^{-1} \left[H_{n-m}(kL) i^{m-n} + H_{n+m}(kL) i^{-m+n} \right] \tag{5.20}$$

and x-even/y-odd (EO) and x-odd/y-odd (OO) mode classes,

$$\left(I + A^{E/O,O}\right) X_1^{E/O,O} = 0, \tag{5.21}$$

$$A_{mn}^{E/O,O} = \mp V_m w_m^{-1} D_m^{-1} \left[H_{n-m}(kL) i^{m-n} - (-1)^m H_{n+m}(kL) i^{m+n} \right] \tag{5.22}$$

where D_m is given by (5.2), $\mu_0 = 1/2,\ \mu_{n>0} = 1$ and

$$V_m = J'_m(ka) J'_m(k\nu a) - iZ \left[\nu J'_m(ka) J_m(k\nu a) - J_m(ka) J'_m(k\nu a) \right], \tag{5.23}$$

The large-index asymptotics of the cylindrical functions allow to establish that each of equations (5.19) and (5.21) is a Fredholm second kind matrix equation in the space of sequences $l_2 \otimes l_2$. Thanks to this, their infinite-dimension determinants exist as functions of all parameters of the problem. Besides, thanks to the Fredholm theorems generalized for the operators [157], the characteristic numbers of (5.19) and (5.21) are discrete on the plane (k, γ) and depend continuously on the geometrical and material parameters of the problem. Moreover, this guarantees that the approximate characteristic numbers, found from the truncated determinantal equations,

$$\mathrm{Det}\left\{\delta_{mn} - A_{mn}^{(p,q)}(k,\gamma)\right\}_{m,n=0(1)}^{N_{tr}} = 0, \quad p,q,= E,O\,, \tag{5.24}$$

converge to the exact values for progressively larger truncation numbers N_{tr} [158].

To illustrate the splitting of the dimer plasmon modes into quartets, we present in Fig. 5.6 the near magnetic field patterns of four supermodes P_1 of the EE, OE, EO and OO symmetry classes. Note that the symmetry (anti-symmetry) of the H-field entails anti-symmetry (symmetry) of the E-field pattern.

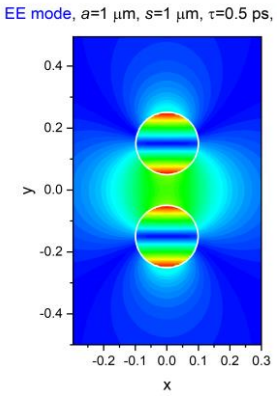

f= 4.56 THz, γ=0.072

(a)

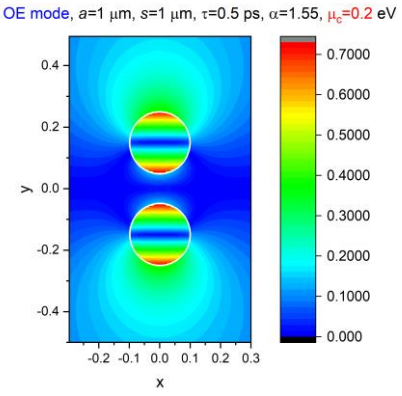

f= 4.55 THz, γ=0.08

(b)

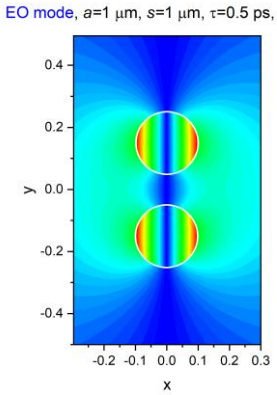

f= 4.25 THz, γ=0.1

(c)

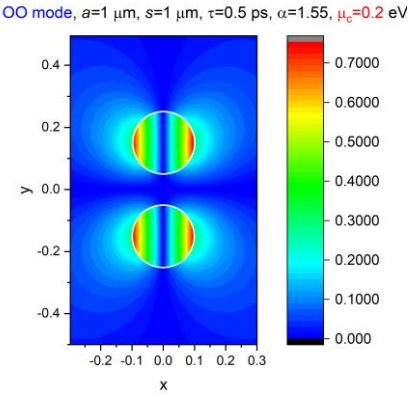

f= 4.26 THz, γ=0.089

(d)

Fig. 5.6 The near magnetic field patterns of four supermodes P_1 of the EE (a), OE (b), EO (c), and OO (d) symmetry classes. The threshold values of the frequency of emission and the gain index are given below each picture

Note that the matrix elements in (5.24) need no numerical integrations, and hence can be easily computed with machine precision.

It should be emphasized that the scaling of the unknowns with the aid of the weight w_n (5.17) is crucially important. Without this scaling, the matrix elements would decay with $n \to \infty$ however grow up exponentially with $m \to \infty$ that prohibits, mathematically, the truncation of the matrix.

5.2.2 Dimer-wire laser mode properties

In Fig. 5.7, we show the trajectories of the dimer plasmon supermode quartets on the plane (f, γ), under the variation of the chemical potential of graphene. Here, two supermode quartets are present, built on the plasmon modes P_1 and P_2 in each wire, for two values of the inter-wire separation, 100 nm for panel (a) and 1 μm for panel (b). Although being split here, supermode trajectories, in general, are still close to the hyperbola defined by equation (5.9). Only the "dipole" supermodes $P_1^{(p,q)}$ display deviations, which become smaller if the separation gets larger.

Finally, in Fig. 5.8 we present the mode trajectories of three supermode quartets, $P_{1,2,3}^{(p,q)}$, under the variation of the inter-wire separation distance from 10 nm to 1 μm, for two values of the chemical potential, 0.2 eV for panel (a) and 0.5 eV for panel (b).

As expected, if the wires move away from each other, then all four modes of a quartet migrate to the same "destination point," which is the single-wire mode frequency and threshold (marked with stars).

The largest splits and the slowest pace of reaching the limit are again associated with the "dipole" supermodes, $P_1^{(p,q)}$. This can be explained by the fact that the compression of the plasmon-mode fields to the graphene shell increases with the mode index, m, therefore the distance needed for efficient coupling gets smaller. Note that, in all examples, the supermodes built on the wire modes, H_{01} and H_{11}, are off the studied

range of frequencies, from the blue side. Note that one or two supermodes of a quartet can have lower thresholds than the similar plasmon mode of the single nanowire.

(a)

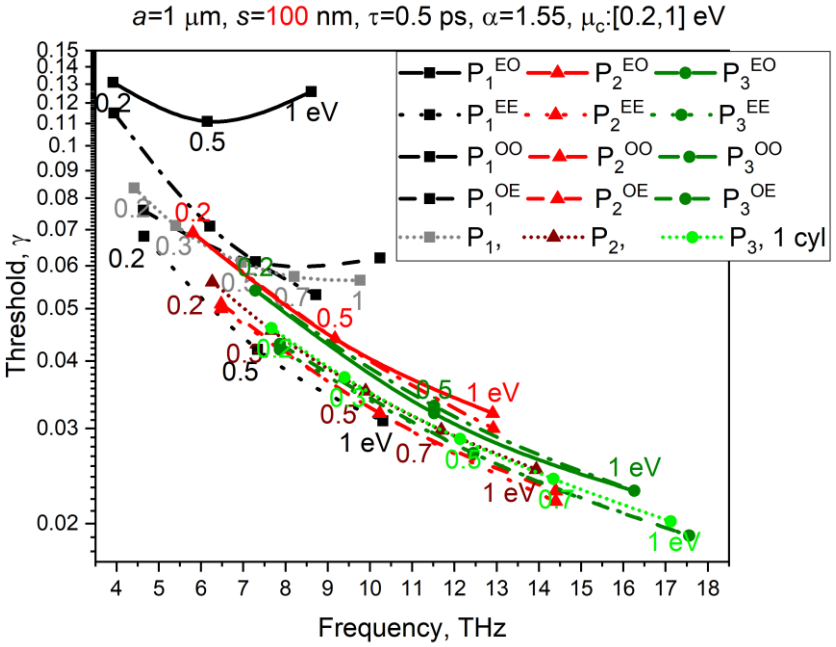

(b)

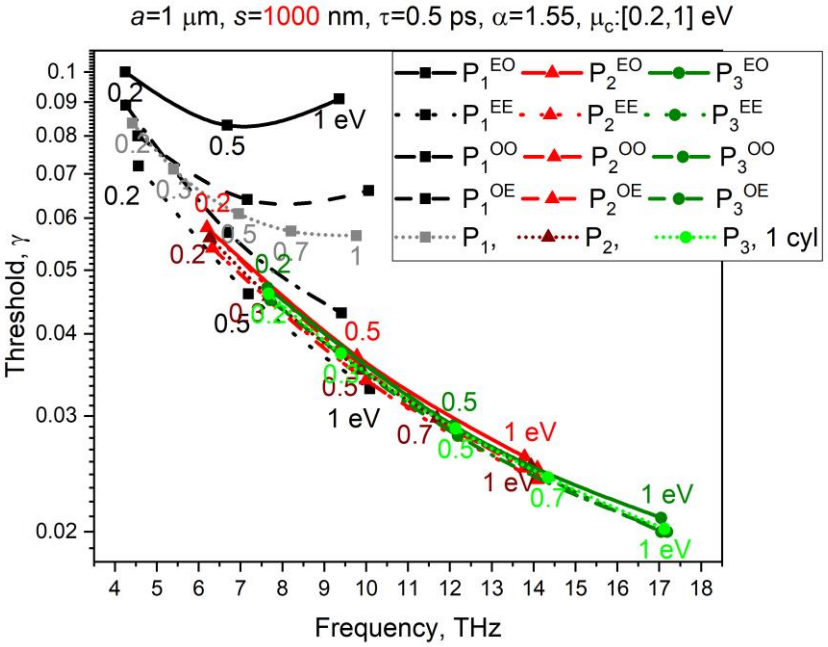

Fig. 5.7 Trajectories of the plasmon supermodes P_m of the dimer-wire laser with parameters a = 1 μm and separation distances s = 100 nm (a) and 1 μm (b), under the variation of the chemical potential of graphene. Other parameters are as marked

(a)

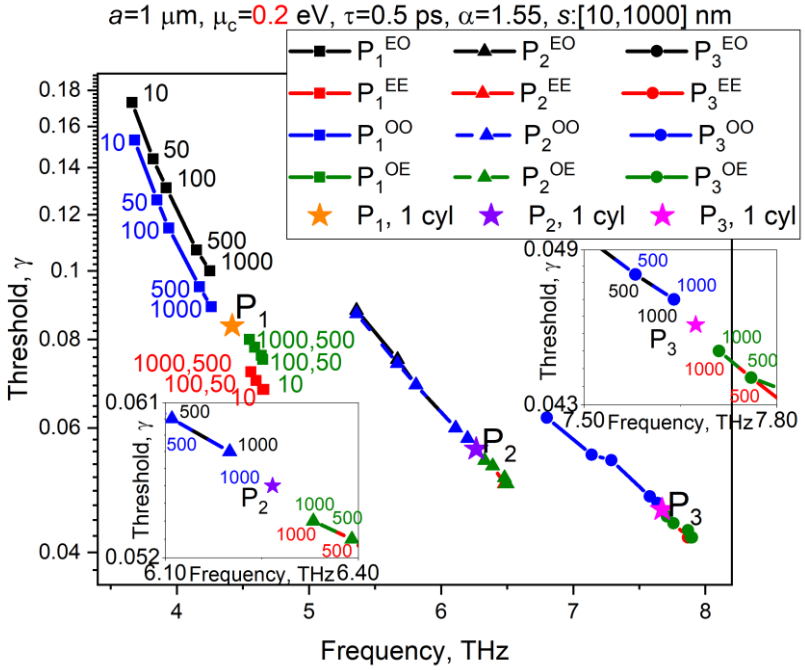

(b)

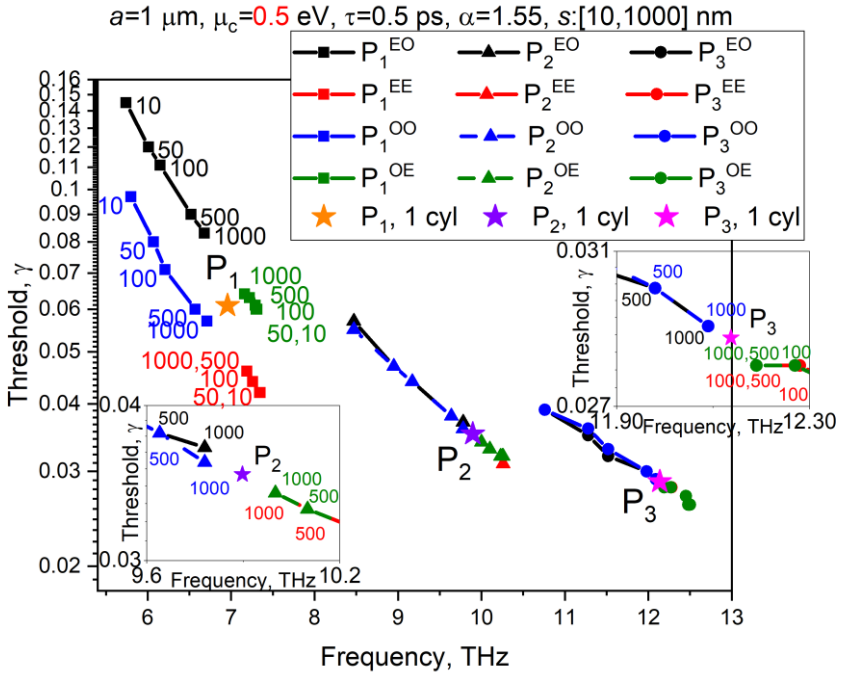

Fig. 5.8 Trajectories of the plasmon supermodes P_m of the dimer-wire laser with parameters a = 1 μm and the chemical potential of graphene μ_c = 0.2 eV (a) and 0.5 eV (b), under the variation of the inter-wire separation, s

Conclusions to Chapter 5

- We have presented the computational electromagnetic analysis of the threshold conditions for the modes of the plasmonic graphene nanolasers based on the circular QW wrapped in graphene and a dimer of such wires. Using the Kubo formalism and separation of variables, adapted to the LEP approach, we have derived full-wave transcendental and determinantal equations for the transversal mode emission frequencies and the material gain thresholds in the single wire and dimer cases, respectively. These equations are easily coded in straightforward manner and computed with machine precision, making the use of commercial codes unnecessary.

- Besides, for a single-wire laser we have derived approximate analytical expressions for the plasmon-mode frequencies and thresholds, neglecting the radiation losses and only using the Drude term (i.e. the intraband component) in the description of graphene's surface conductivity. These expressions are in excellent agreement with full-wave computations in very wide range of the wire radii and frequencies. As new result, we have found that the product of any plasmon-mode frequency and threshold is close to a constant, defined by the QW refractive index and electron relaxation time, only.

- If the QW radius is smaller than 10 μm, then the plasmon modes or supermodes have lower frequencies and thresholds than the 'parasitic" QW modes, however, in thicker wires they can be comparable. As expected, only the plasmon-mode characteristics can be well controlled with the aid of the graphene chemical potential. In the dimer, the plasmon supermodes form tight quartets, approaching the single-wire mode characteristics if the inter-wire separation becomes comparable to the radius. Whatever the separation, the EE supermode, featuring the *x*-even and *y*-even H-field, shows the threshold, lower than of the same mode in a single graphene-covered QW. This can be explained by the fact that this supermode has zero E field at the *x* and *y* axes. We believe that these results bring a clearer vision of how to build single-mode graphene-covered plasmonic nanolasers and their arrays.

CONCLUSIONS

In the dissertation, a mathematically grounded numerical algorithm with guaranteed convergence has been developed for the study of the DR effect for various configurations of circular nanowires and nanotubes made of dielectric, silver, and graphene excited by the modulated beam of charged particles. The considered DR problems have been either solved analytically - for single wires, or reduced to the a Fredholm second-kind matrix equation of the block type, which can be solved numerically with controlled accuracy up to machine precision – for multiple wires. This has allowed us to investigate the spectral characteristics of the DR-caused EM field scattering and absorption by finite configurations of circular nanowires and nanotubes, excited by the modulated beams of charged particles, as well as the eigenmodes of such nanowire configurations.

The main conclusions of the work can be formulated as follows:

- if the particle beam trajectory is shifted from the central (symmetric) position between the twin nanowires, then the DR scattering and absorption spectra display appearance of previously absent resonances, associated with the dimer supermodes whose fields are orthogonal, in symmetry, to the beam field; the intensities of new peaks are proportional of the beam displacement or its angular shift;
- the above-mentioned effect has been found for the high-Q supermodes of the dimers of high refractive-index dielectric wires, thin noble-metal nanotubes, and graphene-covered wires at the high enough values of graphene’s chemical potential;
- to observe the mentioned effect, the frequencies of the modes of different azimuthal orders in single circular resonator, used in the dimer, have to be well separated from each other; therefore, it is not observed for the plasmon modes of the dimers of solid circular noble-metal nanowires;
- in the analysis of DR from sparse finite periodic arrays of many graphene-covered nanowires, the dominant feature in the frequency spectra of DR power are the resonances on the plasmon modes of each wire and the lattice modes of the whole array;

the latter resonance peak intensities strongly depend on the number of wires;

- the Optical Theorem (OT), known previously in the plane-wave scattering, has been adapted to the DR effect: that entails introduction of the complex-valued angles of incidence; the derived expression can be used for partial validation of numerical codes; in the thesis, OT has been satisfied with machine precision;
- in the analysis of the lasing threshold conditions of the modes of single circular graphene-covered active wire, we have found that if the wire radius is smaller than 10 μm, then the "working" plasmon modes are much lower, both in the frequencies and in the threshold values of the gain in active region, than the "parasitic" dielectric wire modes; otherwise, they become comparable;
- if the separation between the wires in graphene-covered active circular nanowire dimer becomes larger than their radius, then all four plasmon supermodes of the lowest types form very tight quartets both in frequencies and in thresholds;
- the obtained results of numerical analysis of the DR-caused scattering and absorption characteristics, far and near field patterns of the wave emission from charged particle beam moving near various nanowire scatterers and gratings of them have fundamental significance and wide range of applications. The latter includes BPM and DLA designs. The analysis of thresholds conditions for the plasmon modes of the considered in the thesis nanolasers can help in the creation of new, more efficient nanolasers;
- the developed computational codes of the DR-caused scattering and absorption characteristics permit using them as a core of the software for numerical optimization of optical configurations, key elements of which are circular nanowires.

The author is sincerely grateful to her supervisor Dr. Sergii V. Dukhopelnykov and the team of the Laboratory of Micro and Nano Optics of the IRE NASU for their assistance in preparing the dissertation, and personally to the head of the laboratory Prof. Alexander I. Nosich for the inspiration and his wise guidance. Special thanks to Prof. R. Sauleau from IETR, Universite de Rennes 1, especially during the full-scale invasion of Ukraine. Many thanks also to her husband Serhii and her family for their constant support and encouragement.

REFERENCES

1. Smith S. J., Purcell E. M. "Visible light from localized surface charges moving across a grating," Phys. Rev., vol. 92, art. 1069, 1953.
2. Sologub V. G. et al. "Excitation of an electromagnetic field by an electron beam traveling close to a diffraction grating," Radiophys. Quant. Electron., vol. 11, no 4, pp. 327-333, 1968.
3. P. M. van den Berg, "Smith-Purcell radiation from a line charge moving parallel to a reflection grating," J. Opt. Soc. Am., vol. 63, no 6, pp. 689-698, 1973.
4. Veliev E. I., Nosich A. I., Shestopalov V. P., "Radiation of an electron flux moving over a grating consisting of cylinders with longitudinal slits," Radiophysics Quant. Electron., vol. 20, no 3, pp. 306-313, 1977.
5. Nosich A. I. "Diffraction radiation which accompanies the motion of charged particles near an open resonator," Radiophys. Quant. Electron., vol. 24, no 8, pp. 696-701, 1981.
6. Pazynin L. A., Sologub V. G. "Diffraction radiation of a point charge moving along the axis of a segment of a circular waveguide," Radiophys. Quantum Electron. vol. 27, no 10, pp. 816-822, 1984.
7. Boltonosov A. I., Sologub V. G. "Excitation of an open strip-type resonator by a modulated beam of charged particles," Sov. J. Communic. Technol. Electron., vol. 33, no 6, pp. 133-140, 1988.
8. Steshenko S.A., Tsvyk A.I., Khutoryan E.M. “Radiation patterns of "plasma" electron beam on structures of metal grooves,” Proc. Int. Kharkov Symp. Physics Eng. Microwaves, Millimeter, Submillimeter Waves (MSMW-2004), vol. 2, pp. 521-524, 2004.
9. Sautbekov S.S., Sirenko K.Y., Sirenko Y.K., Poyedinchuk A.Y., Yashina N.P., Yevdokymov A.P. “The Smith-Purcell effect. Anomalously high level of outgoing wave excitation,” Telecommunic. Radio Eng., vol. 77, no 6, pp. 469–487, 2018.

10. Castellano M. "A new non-intercepting beam size diagnostics using diffraction radiation from a slit, " Nuclear Instrum. Meth. A, vol. 394, pp. 275-280, 1997.
11. Potylitsyn A. P. “Resonant diffraction radiation and Smith-Purcell effect,” Phys. Lett. A, vol. 238, pp. 112-116, 1998.
12. Castellano M. et al. "Measurements of coherent diffraction radiation and its application for bunch length diagnostics in particle accelerators," Phys. Rev. E, vol. 63, art. no 056501, 2001.
13. Karataev P. et al. "Beam-size measurement with optical diffraction radiation at KEK accelerator test facility," Phys. Rev. Lett., vol. 93, art. no 244802, 2004.
14. Goponov Y. A., Shatokhin R. A., and Sumitani K. “Diffracted diffraction radiation and its application to beam diagnostics,” Nuclear Instrum. Meth. A, vol. 885, pp. 134–138, 2018.
15. Bobb L., Kieffer R., et al. "Feasibility of diffraction radiation for noninvasive beam diagnostics as characterized in a storage ring," Phys. Rev. Accel. Beams, vol. 21, art. no 03801, 2018.
16. Muto T., Araki S., et al. “Observation of incoherent diffraction radiation from a single-edge target in the visible-light region,” Phys. Rev. Lett., vol. 90, no 10, pp. 104801-104804, 2003.
17. Talebi N., "Interaction of electron beams with optical nanostructures and metamaterials: from coherent photon sources towards shaping the wave function," J. Opt., vol. 19, art. no 103001, 2017.
18. Leedle K. J., et al. "Dielectric laser acceleration of sub-100 keV electrons with silicon dual-pillar grating structures," Opt. Lett., vol. 40, no, 18. pp. 4344-4347, 2015.
19. Bohren C. F., Huffman D. R. "Absorption and Scattering of Light by Small Particles," Wiley-VCN Publ, Weinheim, 2004.
20. Novotny L., Hecht B., "Principles of Nano-Optics," Cambridge Univer. Press, 2012.
21. Low T., Avouris P. "Graphene plasmonics for terahertz to mid-infrared applications," ACS Nano 8, pp. 1086–1101, 2014.

22. Ullah Z., et al. "A review on the development of tunable graphene nanoantennas for terahertz optoelectronic and plasmonic applications," Sensors, vol. 20(5), art. 1401, 2020.
23. Zhao J., et al. "Surface-plasmon-polariton whispering-gallery mode analysis of the graphene monolayer coated InGaAs nanowire cavity," Opt. Exp., vol. 22, pp. 5754-5761, 2014.
24. Liu J. P., et al. "Analysis of mid-infrared surface plasmon modes in a graphene-based cylindrical hybrid waveguide," Plasmonics, vol. 11, pp. 703–711, 2016.
25. Dai C., et al. "Hybridized radial and edge coupled 3D plasmon modes in self-assembled graphene nanocylinders," Small, vol. 17, art. no 2100079, 2021.
26. Zhu B., et al. "Field enhancement and gradient force in the graphene-coated nanowire pairs," Plasmonics, vol. 10, no 4, pp. 839-845, 2015.
27. Naserpour M., et al. "Tunable invisibility cloaking by using isolated graphene-coated nanowires and dimers," Sci. Rep., vol. 7, no 1, pp. 1-14, 2017
28. Purcell E. M., Pennypacker C. R., "Scattering and absorption of light by nonspherical dielectric grains," The Astrophysical J., vol. 186, pp. 705–714, 1973.
29. Yurkin M.A., Hoekstra A.G. "The discrete dipole approximation: An overview and recent developments," J. Quant. Spectrosc. Radiat. Transf., vol. 106, pp. 558-589, 2007.
30. Draine B. T. "The discrete-dipole approximation and its application to interstellar graphite grains," The Astrophysical J., vol. 333, p. 848, 1988.
31. Draine B. T., Flatau P. J. "Discrete-dipole approximation for scattering calculations," J. Opt. Soc. Am. A vol. 11, pp. 1491-1499, 1994.
32. Draine B.T. "The discrete dipole approximation for light scattering by irregular targets" In: Mishchenko M.I., Hovenier J.W., Travis L.D., editors. "Light Scattering by Nonspherical Particles, theory, measurements, and applications" New York: Academic Press, pp. 131–45, 2000.
33. Draine B.T., Flatau P.J. "User guide for the discrete dipole approximation code DDSCAT 6.1.," /http://xxx.arxiv.org/abs/astro-ph/0409262S, 2004.

34. Goedecke G. H., O'Brien S. G. "Scattering by irregular inhomogeneous particles via the digitized Green's function algorithm," Appl. Opt. vol. 27, pp. 2431-2438, 1988.
35. Hage J.I., Greenberg J.M., Wang R.T. "Scattering from arbitrarily shaped particles: theory and experiment," Appl. Opt., vol. 30, pp.1141-1152, 1991.
36. Peterson A.W., Ray S.L., Mittra R. "Computational Methods of Electromagnetic Scattering," IEEE Press, 1998.
37. Kim O.S., Meincke P., Breinbjerg O., Jorgensen E. "Method of moments solution of volume integral equations using higher-order hierarchical Legendre basis functions," Radio Sci., art. 39, 2004.
38. Evans K.F., Stephens G.L. "Microwave radiative-transfer through clouds composed of realistically shaped ice crystals 1. Single scattering properties," J Atmos Sci, vol. 52, pp.2041–2057, 1995.
39. Okamoto H., Macke A., Quante M., Raschke E. "Modeling of backscattering by non-spherical ice particles for the interpretation of cloud radar signals at 94 GHz. An error analysis," Contrib. Atmos. Phys., vol. 68, pp. 319–34, 1995.
40. Liu C.L., Illingworth A.J. "Error analysis of backscatter from discrete dipole approximation for different ice particle shapes," Atmos. Res., vol. 44, pp. 231–241, 1997.
41. Lemke H., Okamoto H., Quante M. "Comment on error analysis of backscatter from discrete dipole approximation for different ice particle shapes" [Liu, C.-L., Illingworth, A.J., 1997, Atmos. Res. 44, 231–241.]. Atmos. Res., vol. 49, pp. 189–97, 1998.
42. Liu C.L., Illingworth A.J. Reply to comment by Lemke, Okamoto and Quante on "Error analysis of backscatter from discrete dipole approximation for different ice particle shapes". Atmos.Res., vol. 50, pp. 1–2, 1999.
43. Wriedt T. "A review of elastic light scattering theories," Particle and Particle Systems Characterization, vol. 15, pp. 67-74, 1998.
44. Mishchenko M.I., Travis L.D., Lacis A.A. "Scattering, Absorption, and Emission of Light by Small Particles, " Cambridge: Cambridge University Press, 2002.

45. Tsang L., Kong J.A., Ding K.H., Ao C.O. "Scattering of Electromagnetic Waves: Numerical Simulations, " New York: Wiley, 2001.
46. Yang P., Liou K. N. "Finite difference time domain method for light scattering by nonspherical and inhomogeneous particles" In: Mishchenko MI, Hovenier JW, Travis LD, editors. "Light Scattering by Nonspherical Particles, Theory, Measurements, and Applications" New York: Academic Press, p. 131–45, 2000.
47. Yee K.S. "Numerical solution of initial boundary value problems involving Maxwell's equations in isotropic media," IEEE Transactions on Antennas Propagation, vol. 14, pp. 302-307, 1966.
48. Taflove A. "Application of the finite-difference time-domain method to sinusoidal steady-state electromagnetic-penetration problems, " IEEE Trans. Electromagn. Compat., vol. 22, pp. 191–202, 1980.
49. Kunz K. S., Luebbers R. J. "Finite Difference Time Domain Method for Electromagnetics." CRC Press, Boca Raton, FL, 1993.
50. Holland R., Simpson L., and Kunz K. "Finite-difference analysis of EMP coupling to lossy dielectric structures," IEEE Trans. Electromagn. Compat., vol. 22, pp. 203–209, 1980.
51. Andrew W. V., et al. "Finite-difference time-domain analysis of HF antennas on helicopter airframes," IEEE Trans. Electromagn. Compat., vol. 39, pp. 100–113, 1997.
52. Sheen D. M., Ali S. M., Abouzahra M. D., Kong J. A. "Application of the three-dimensional finite-difference time-domain method to the analysis of planar microstrip circuits," IEEE Trans. Microwave Theory Tech., vol. 38, pp. 849–857, 1990.
53. Sullivan D. M., Borup D. T., Gandhi O. P. "Use of the finite-difference time domain method in calculating EM absorption in human tissues " IEEE Trans. Biomed. Eng., vol. 34, pp. 148–157, 1987.
54. Ludiyati H., Suksmono A. B., Munir A., "FDTD method for property analysis of waveguide loaded artificial circular dielectric resonator with anisotropic

permittivity," 2016 Progress in Electromagnetic Research Symp. (PIERS-2016), Shanghai, China, pp. 315-318, 2016.

55. Nguyen B. T., Furse C., Simpson J. J., "A 3-D Stochastic FDTD model of electromagnetic wave propagation in magnetized ionosphere plasma," IEEE Transactions on Antennas and Propagation, vol. 63, no. 1, pp. 304-313, 2015.
56. Boriskin A. V., Rolland A., Sauleau R., Nosich A. I., "Assessment of FDTD accuracy in the compact hemielliptic dielectric lens antenna analysis," IEEE Transactions on Antennas and Propagation, vol. 56, no. 3, pp. 758-764, 2008.
57. M. J. M. van der Vorst, P. J. I. de Maagt "Efficient body of revolution finite-difference time-domain modeling of integrated lens antennas," IEEE Microw. Wireless Compon. Lett., vol. 12, no.7, pp. 258–260, 2002.
58. Hower G. L., Olsen R. G., Earls J. D., Schneider J. B., "Inaccuracies in numerical calculations of scattering near natural frequencies of penetrable objects," IEEE Trans. Antennas Propag., vol. 41, no.7, pp. 982–986, 1993.
59. Liu Y., Sarrisa C. D., and Eleftheriades G. V. "Triangular mesh- based FDTD analysis of 2-D plasmonic structures supporting backward waves at optical frequencies," J. Lightwave Technol., vol. 25, pp. 938–946, 2007.
60. Boriskin A. V., Boriskina S. V., Rolland A., Sauleau R., Nosich A. I., "Test of the FDTD accuracy in the analysis of the scattering resonances associated with high-Q whispering-gallery modes of a circular cylinder," J. Opt. Soc. Am. A vol. 25, pp. 1169-1173, 2008.
61. Hagness S. C., Rafizadeh D., Ho S. T., Taflove A., "FDTD microcavity simulations: design and experimental realization of waveguide-coupled single-mode ring and whispering-gallery-mode disk resonators," J. Lightwave Technol., vol. 15, pp. 2154–2165, 1997.
62. Sakai A., Baba T., "FDTD simulation of photonic devices and circuits based on circular and fan-shaped microdisks," J. Lightwave Technol., vol. 17, pp. 1493–1499, 1999.

63. Sautbekov, S.S., Sirenko, K.Y., Sirenko, Y.K., Poyedinchuk A.Y. Yashina, N.P., Yevdokymov, A.P. “The Smith-Purcell effect. Anomalously high level of outgoing wave excitation,” Telecommunic. Radio Eng., vol. 77, no 6, pp. 469–487, 2018.
64. Taflove A., Hagness S. C., "Computational Electrodynamics: The Finite-Difference Time-Domain Method," Artech House, Mass, USA, 3rd edition, 2005.
65. Lord Rayleigh, "On the electromagnetic theory of light, " The London, Edinburgh, and Dublin Philosophical Magazine and Journal of Science, vol.12, n. 73, pp. 81-101, 1881.
66. Maxwell, J. C., "A dynamical theory of the electromagnetic field," Philosophical Transactions of the Royal Society of London, vol. 155, pp. 459–512, 1865.
67. Mie G. "Beitr¨age zur Optik tr¨uber Medien, speziell kolloidaler Metall¨osungen," Annalen der Physik, vol. 330, no. 3, pp.377–445, 1908.
68. Li J., Shanker B., "Time-dependent Debye–Mie series solutions for electromagnetic scattering," IEEE Transactions on Antennas and Propagation, vol. 63, no. 8, pp. 3644-3653, 2015.
69. Lorenz L. "Lysbevaegelsen i og uden for en af plane Lysbolger belyst Kugle, "Det Kongelige Danske Videnskabernes Selskabs Skrifter, vol. 6, no 6, pp. 1–62, 1890.
70. Debye P. "Der Lichtdruck auf Kugeln von beliebigem material," Annalen der Physik, vol. 30, no. 1, pp. 57–136, 1909.
71. Logan N., "Survey of some early studies of the scattering of plane waves by a sphere, " Proceedings of the IEEE, vol. 53, pp. 773–785, 1965.
72. Lock J. A., Gouesbet G. "Generalized Lorenz-Mie theory and applications, " Journal of Quantitative Spectroscopy and Radiative Transfer, vol. 110, no. 11, pp. 800–807, 2009.
73. Xu F., Ren K., Gouesbet G., Gr´ehan G., Cai X. "Generalized lorenz-mie theory for an arbitrarily oriented, located, and shaped beam scattered by a homogeneous spheroid," J. Opt. Soc. Am. A, vol. 24, pp. 119–131, 2007.

74. Hough J., Gouesbet G. "Generalized Lorenz-Mie theories, the third decade: A perspective," Journal of Quantitative Spectroscopy and Radiative Transfer, vol. 110, no. 14, pp. 1223–1238, 2009.
75. Greengard L., Hagstrom T., Jiang Sh., "Extension of the Lorenz–Mie–Debye method for electromagnetic scattering to the time-domain," Journal of Computational Physics vol. 299, pp. 98-105, 2015.
76. Gagnon D., Dubé L.J. "Lorenz–Mie theory for 2D scattering and resonance calculations," J. Optics, vol. 17, art. no. 103501, 2015.
77. Twersky V. "On a multiple scattering theory of the finite grating and the Wood anomalies, " J. Appl. Phys., vol. 23, pp. 1099–1118, 1952.
78. Twersky V. "Multiple scattering of radiation by an arbitrary planar configuration of parallel cylinders and by two parallel cylinders," J. Appl. Phys. vol. 23, pp. 407–414, 1952.
79. Twersky V. "Remarks on the theory of grating anomalies," J. Opt. Soc. Am., vol. 42, pp. 855-856, 1952.
80. Wait J. R. "Scattering of a plane wave from a circular dielectric cylinder at oblique incidence," Canadian J. Physics. vol. 33, pp. 189-195, 1955.
81. Twersky V. "On scattering of waves by the infinite grating of circular cylinders," IRE Trans. Antennas Propagation., vol. 10, no 3. pp. 737-765, 1962.
82. Olaofe G. O. "Scattering by two cylinders," Radio Science, vol. 4, pp. 1351–1360, 1970.
83. Ragheb H. A., Hamid M. "Scattering by N parallel conducting circular cylinders," Int. J. of Electronics, vol. 59, pp. 407-421, 1985.
84. Elsherbeni A. Z., Kishk A. A. "Modeling of cylindrical objects by circular dielectric and conducting cylinders," IEEE Trans. Antennas Propagat., vol. 40, pp. 96-99, 1992.
85. Felbacq D., Tayeb G., Maystre D. "Scattering by a random set of parallel cylinders," J. Opt. Soc. Am. A., vol. 11, pp. 2526–2538, 1994.

86. Шестопалов В.П., Литвиненко Л.Н., Масалов С.А., Сологуб В.Г. "Дифракция волн на решетках" Изд-во Харьковского Университета, 1973.
87. Bogdanov F.G., Kevanishvili G.Sh., Chikhladze M.N. "Diffraction of a plane electromagnetic wave from a lattice of coaxial dielectric cylinders," Radiophysics and Quant. Electron., vol. 30, no 5, pp. 485-491, 1987.
88. Kantorovich, L.V. Akilov, G.P. "Functional Analysis," 2nd ed.; Pergamon Press: Oxford, UK, Elmsford, NY, USA, 1982.
89. Hanson G. W., Yakovlev A. B. "Operator Theory for Electromagnetics," Springer New York, 2002.
90. Nosich A.I. "Method of Analytical Regularization in wave-scattering and eigenvalue problems: foundations and review of solutions," IEEE Antennas and Propagation Magazine, vol. 42, no 3, pp. 34-49, 1999.
91. Muskhelishvili N.I. "Singular Integral Equations; Boundary Problems of Function Theory and Their Application to Mathematical Physics," Groningen: P. Noordhoff; 1953.
92. Lucido M., Kobayashi K., Medina F., Nosich A.I., Vinogradova E.D. "Guest Editorial: Method of analytical regularisation for new frontiers of applied electromagnetics," IET Microwaves, Antennas and Propagation, vol. 15, no 10, pp. 1127-1132, 2021.
93. Johnson P. B., Christy R. W. "Optical constants of the noble metals," Phys. Rev. B, vol. 6, pp. 4370-4379, 1972.
94. Babar Sh., Weaver J. H. "Optical constants of Cu, Ag, and Au revisited," Appl. Opt., vol. 54, pp. 477-481, 2015.
95. Velichko E.A., Natarov D.M., "Localized versus delocalized surface plasmons: dual nature of resonances on a silver circular wire and a silver tube of large diameter," IOP J. of Optics, vol. 20, no 7, at no 075002, 2018.
96. Geim A. K., Novoselov K. S. “The rise of graphene,” Nature Materials, vol.6, pp. 183-191, 2007.

97. Novoselov K., S. et al. " Electric field effect in atomically thin carbon films," Science, vol. 306, pp. 666–669, 2004.
98. Cao K., Tian Z., Zhang X. et al. "Green preparation of graphene oxide nanosheets as adsorbent, " Sci. Rep, vol. 13, art. no. 9314, 2023.
99. Cuevas M., Raad S. H., Zapata-Rodríguez C. J. "Coupled plasmonic graphene wires: theoretical study including comp ex frequencies and field distributions of bright and dark surface plasmons," J. Opt. Soc. Am. B, vol. 37, no 10, pp. 3084-3093, 2020.
100. Velichko E. A., "Evaluation of a dielectric microtube with a graphene cover as a refractive-index sensor in the THz range," J. Optics, vol. 18(3), no. 035008, 2016.
101. Li H.J., Wang L.L., Liu J.Q., Huang Z.R., Sun B., Zhai X., "Investigation of the graphene based planar plasmonic filters," Appl. Phys. Lett., vol. 103, no 21, art. 211104, 2013.
102. Li H.J., Wang L.L., Sun B., Huang Z.R., Zhai X., "Tunable mid-infrared plasmonic band-pass filter based on a single graphene sheet with cavities," J. Appl. Phys., vol. 116(22), art. no. 224505, 2014.
103. Li H., Ji C., Ren Y., Hu J., Qin M., Wang L., "Investigation of multiband plasmonic metamaterial perfect absorbers based on graphene ribbons by the phase-coupled method," Carbon, vol. 141, pp. 481–487, 2019.
104. Dukhopelnikov S. V., Sauleau R., Nosich A. I., "Integral equation analysis of terahertz backscattering from circular dielectric rod with partial graphene cover," IEEE J. Quant. Electron., vol. 56, art. no. 8500208, 2020.
105. Dukhopelnikov S. V., Lucido M., Nosich A. I., "Circular dielectric rod with conformal strip of graphene as tunable terahertz antenna: interplay of inverse electromagnetic jet, whispering gallery and plasmon effects," IEEE J. Sel. Top. Quant. Electron., vol. 27, art. no. 4600908, 2021.
106. Balaban M.V., Shapoval O.V., Nosich A.I., "THz wave scattering by a graphene strip and a disk in the free space: integral equation analysis and surface plasmon resonances," J. of Optics, vol. 15, no 11, art. no 114007, 2013.

107. Hanson G. W., "Dyadic Green's functions and guided surface waves for a surface conductivity model of graphene," J. Appl. Phys., vol. 103, pp. 064302, 2008.
108. Oguzer T., Altintas A., Nosich A.I., "Focusing of THz waves with a microsize cylindrical reflector made of graphene in the free space," J. European Optical Society - Rapid Publications, vol. 13, no 1, art. no 16, 2017.
109. Zinenko T.L., Matsushima A., Nosich A.I., "Surface-plasmon, grating-mode and slab-mode resonances in THz wave scattering by a graphene strip grating embedded into a dielectric slab," IEEE J. Selected Topics in Quantum Electronics, vol. 23, art. no 4601809, 2017.
110. Kim, M., Kim, SH., Kang, C. et al. "Highly efficient graphene terahertz modulator with tunable electromagnetically induced transparency-like transmission," Sci. Rep., vol. 13, art. no. 6680, 2023.
111. Smotrova E.I., Tsvirkun V., Gozhyk I., Lafargue C., Ulysse C., Lebental M., Nosich A.I. "Spectra, thresholds and modal fields of a kite-shaped microcavity laser," J. Optical Society America B, vol. 30, no 6, pp. 1732-1742, 2013.
112. Smotrova E.I., Nosich A.I. "Mathematical study of the two-dimensional lasing problem for the whispering-gallery modes in a circular dielectric microcavity," Optical and Quantum Electronics, vol. 36, no 1-3, pp. 213-221, 2004.
113. Nojima S. "Theoretical analysis of feedback mechanisms of two-dimensional finite-sized photonic-crystal lasers," J. Appl. Phys., vol. 98, no. 4, art. no 043102, 2005.
114. Mock A. "First principles derivation of microcavity semiconductor laser threshold condition and its application to FDTD active cavity modeling," J. Opt. Soc. Amer. B, vol. 27, no 11, pp. 2262–2272, 2010.
115. Chang S. W., "Confinement factors and modal volumes of micro- and nanocavities invariant to integration regions," IEEE J. Sel. Top. Quant. Electron., vol. 18, no 6, pp. 1771–1780, 2012.
116. Huang Y., Lu Y. Y., "Efficient method for lasing eigenvalue problems of periodic structures," J. Mod. Opt., vol. 61, no 5, pp. 390–396, 2014.

117. Yu H.Q., Jiang S.M., Wu D.J., "Efficient surface plasmon amplification in gain-assisted silver nanotubes and associated dimers, " J. Appl. Phys., vol. 117, art. no 153101, 2015.

118. Dettmann C.P., Morozov G.V., Sieber M., Waalkens H. "Internal and external resonances of dielectric disks, " Eur. Phys. Lett., vol. 87(3), art.no. 34003, 2009.

119. Bayer M., Gutbrod T., Reithmaier J. P., Forchel A., Reinecke T. L., Knipp P. A., Dremin A. A., Kulakovskii V. D. "Optical modes in photonic molecules," Phys. Rev. Lett., vol. 81, art.no 2582, 1998.

120. Kara Y., Mukaiyama T., Takeda K., Kuwata-Gonokami M., "Photonic molecule lasing," Opt. Lett., vol. 28, pp. 2437-2439, 2003.

121. Smotrova E.I., Nosich A.I., Benson T.M., Sewell P. "Threshold reduction in a cyclic photonic molecule laser composed of identical microdisks with whispering gallery modes," Optics Letters, vol. 31, no 7, pp. 921-923, 2006.

122. Smotrova E.I., Nosich A.I., Benson T., Sewell P., "Optical coupling of whispering gallery modes in two identical microdisks and its effect on the lasing spectra and thresholds," IEEE J. Selected Topics in Quantum Electronics, vol. 12, no 1, pp. 78-85, 2006.

123. Li Y., Abolmaali F., Allen K. W., Limberopoulos N. I., Urbas A., Rakovich Y., Maslov A. V., Astratov V. N., "Whispering gallery mode hybridization in photonic molecules," Laser & Photonics Reviews, vol.11, art. no 1600278, 2017.

124. Chen H-J., "Manipulation of fast and slow light propagation by photonic-molecule optomechanics," Journal of Applied Physics, vol. 124 (15), art. no 153102. 2018.

125. Deng Sh., Cai W. "Discontinuous spectral element method modeling of optical coupling by whispering gallery modes between microcylinders," J. Opt. Soc. Am. A, vol. 22, pp. 952-960, 2005.

126. Arslanagić S., Breinbjerg O. "Sub-wavelength resonances in metamaterial-based multi-cylinder configurations," Materials, vol. 4, pp.117-130, 2011.

127. Natarov D.M., Byelobrov V.O., Sauleau R., Benson T.M., Nosich A.I., "Periodicity-induced effects in the scattering and absorption of light by infinite and finite gratings of circular silver nanowires," Optics Express, vol. 19, no 22, pp. 22176-22190, 2011.

128. Natarov D. M., et al., "Effect of periodicity in the resonant scattering of light by finite sparse configurations of many silver nanowires," Plasmonics, vol. 9, no 2, pp. 389-407, 2014.

129. Fesenko V.I., Shcherbinin V.I., Tuz V.R. "Multiple invisibility regions induced by symmetry breaking in a trimer of subwavelength graphene-coated nanowires, " J. Opt. Soc. Am. A, vol. 35, pp.1760–1768, 2018.

130. Byelobrov V.O., Benson T.M., Nosich A.I., "Binary grating of sub-wavelength silver and quantum wires as a photonic-plasmonic lasing platform with nanoscale elements, " IEEE J. Sel. Top. Quantum Electron, vol. 18, pp. 1839–1846, 2012.

131. Byelobrov V. O., Zinenko T. L., Kobayashi K., Nosich A. I. "Periodicity matters: grating or lattice resonances in the scattering by sparse arrays of sub-wavelength strips and wires," IEEE Antennas Propagat. Mag., vol. 57, no 6, pp. 34-45, 2015.

132. Vial A., Laroche T. "Comparison of gold and silver dispersion laws suitable for FDTD simulations," Appl. Phys. B, vol. 93, pp. 139–143, 2008.

133. Lukyanchuk B. S., Ternovsky V. "Light scattering by a thin wire with a surface-plasmon resonance: Bifurcations of the Poynting vector field," Phys. Rev. B, vol. 73, art. no 235432, 2006.

134. Kottmann J. P., Martin O. J. F. "Retardation-induced plasmon resonances in coupled nanoparticles," Opt. Lett., vol. 26, no 14, pp. 1096-1098, 2001.

135. Kottmann J.P., Martin O.J.F. "Plasmon resonant coupling in metallic nanowires," Opt. Exp., vol. 8, no 12, pp. 655-663, 2001.

136. Natarov D.M., Sauleau R., Nosich A.I. "Periodicity-enhanced plasmon resonances in the scattering of light by sparse finite gratings of circular silver nanowires," IEEE Photonics Technology Letters, vol. 24, no 1, pp. 43-45, 2012.

137. Campione S., Steshenko S., Capolino, F. "Complex bound and leaky modes in chains of plasmonic nanospheres," Optics Express, vol. 19, no 19, pp. 18345–18363, 2011.

138. Velichko E.A., Nosich A.I. "Refractive-index sensitivities of hybrid surface-plasmon resonances for a core-shell circular silver nanotube sensor," Opt. Lett., vol. 38, no 23, pp. 4978-4981, 2013.

139. Salvant B., et al. "Beam induced RF heating in LHC in 2015," Proc. Int. Particle Accelerat. Conf. (IPAC 2016), Busan, 2016, pp. 602-605.

140. Frezza F., Mangini F., and Tedeschi N. "Introduction to electromagnetic scattering. Part II. Tutorial," J. Opt. Soc. Am. A, vol. 37, pp. 1300–1315, 2020.

141. Bergamaschi M., Aryshev A., Karataev P., Kieffer R., Lefevre T., Mazzoni S., Terunuma N., Yang R. "Noninvasive micrometer-scale particle-beam size measurement using optical diffraction radiation in the ultraviolet wavelength range," Phys. Rev. Appl., vol. 13, art.no 014041, 2020.

142. Dukhopelnykov S.V., Sauleau R., Nosich A.I. "Integral equation analysis of terahertz backscattering from circular dielectric rod with partial graphene cover," IEEE J. of Quantum Electronics, vol. 56, no 6, art. no 8500208, 2020.

143. Sergeeva D. Y., Tishchenko A. A. "On the polarizability of a cluster of interacting particles in polarization radiation," Phys. Atomic Nuclei, vol. 83, pp. 1489–1492, 2020.

144. England R. J., et.al. "Dielectric laser accelerators," Rev. Mod. Phys., vol. 86, no 4, pp. 1337-1389, 2014.

145. Wei Y., et al. "Dual-grating dielectric accelerators driven by a pulse-front-tilted laser," Appl. Opt., vol. 56, pp. 8201-8206, 2017.

146. Breuer J., et al. "Laser-based acceleration of nonrelativistic electrons at a dielectric structure," Phys. Rev. Lett., vol. 111, art. no 134803, 2013.

147. Leedle K. J. et.al. "Phase-dependent laser acceleration of electrons with symmetrically driven silicon dual pillar gratings, " Opt. Lett., vol. 43, pp. 2181-2184, 2018.

148. Shiloh R., Chlouba T., Yousefi P., Hommelhoff P. "Particle acceleration using top-illuminated nano-photonic dielectric structures," Opt. Exp., vol. 29, no 10, pp. 14403-14411, 2021.

149. Smotrova E.I., et al. "Optical theorem helps understand thresholds of lasing in microcavities with active regions," IEEE J. Quant. Electron., vol. 47, no 1, pp. 20-30, 2011.

150. Byelobrov V. O., et al. "Low-threshold lasing eigenmodes of an infinite periodic chain of quantum wires," Opt. Lett., vol. 35, no 21, pp. 3634-3636, 2010.

151. Spiridonov A. O., et al. "Why elliptic microcavity lasers emit light on bow-tie-like modes instead of whispering-gallery-like modes," Opt. Communic., vol. 439, pp. 112-117, 2019.

152. Shapoval O. V., et al. "Electromagnetic engineering of a single-mode nanolaser on a metal plasmonic strip placed into a circular quantum wire," IEEE J. Sel. Top. Quant. Electron., vol. 23, no. 6, 2017.

153. Natarov D. M., et al. "Electromagnetic analysis of the lasing thresholds of hybrid plasmon modes of a silver tube nanolaser with active core and active shell," Beilstein J. Nanotechnol., vol. 10, pp. 294-304, 2019.

154. Spiridonov A. O., et al. “Mathematical and numerical analysis of the generalized complex-frequency eigenvalue problem for two-dimensional optical microcavities,” SIAM J. Appl. Math., vol. 80, no 4, pp. 1977–1998, 2020.

155. Prelat L., et al. "Spaser and optical amplification conditions in graphene-coated active wires," J. Opt. Soc. Am B, vol. 38, 2021.

156. Yu H.-Q., Jiang S.-M., and Wu D.-J. "Efficient surface plasmon amplification in gain-assisted silver nanotubes and associated dimers," J. Appl. Phys., vol. 117, art. no 153101, 2015.

157. Steinberg S. "Meromorphic families of compact operators,” Arch. Rat. Mech. Analysis, vol. 31, pp. 372–379,1968.

158. Karma O. "Approximation in eigenvalue problems for holomorphic Fredholm operator function. II. Convergence rate," Numer. Func. Anal. Optim., vol. 17, no 3-4, pp. 389–408, 1996.

159. Abramowitz M., Stegun I. A. "Handbook of Mathematical Functions with Formulas, Graphs, and Mathematical Tables", Applied Mathematics Series. vol. 55, Washington D.C.; New York: United States Department of Commerce, National Bureau of Standards; Dover Publications, 1983.

APPENDIX A. LIST OF PUBLICATIONS RELATED TO THESIS

Papers in international journals

A.1. D. O. Herasymova, D.M. Natarov, S.V. Dukhopelnykov, T.L. Zinenko, M. Lucido, and A.I. Nosich, "Threshold conditions for transversal modes of tunable plasmonic nanolasers shaped as single and twin graphene-covered circular quantum wires," IOP Nanomaterials, vol. 33, no. 49, art. no 495001, 2022. **(Q-2)**

A.2. D. O. Herasymova, S. V. Dukhopelnykov and A. I. Nosich, “Infrared diffraction radiation from twin circular dielectric rods covered with graphene: plasmon resonances and beam position sensing,” Journal of the Optical Society of America B, vol. 38, no. 9, pp 183-190, 2021. **(Q-2)**

A.3. D. O. Herasymova, S. V. Dukhopelnykov, M. Lucido and A. I. Nosich, “Optical sensing of electron-beam position with twin silver nanotube antenna tuned to hybrid surface plasmon resonance,” IEEE J. of Selected Topics in Quantum Electronics, vol. 27, no 1, art. no 3024114, 2020. **(Q-1)**

A.4. D. O. Yevtushenko and S. V. Dukhopelnykov, "Visible light from modulated electron beam moving between twin circular silver nanowires forming plasmonic photonic molecule," IOP J. of Optics, vol. 22, no 2, art. no 025002, 2020. **(Q-1)**

A.5. D. O. Yevtushenko, S. V. Dukhopelnykov, and A. I. Nosich, “Electron-beam excitation of supermodes of a photonic molecule built on twin high refractive index dielectric nanowires,” J. of Applied Physics, vol. 125, no 22, art. no 223102, 2019. **(Q-2)**

A.6. D. O. Yevtushenko, S. V. Dukhopelnykov, and A. I. Nosich, "Optical diffraction radiation from a dielectric and a silver nanowire excited by a modulated electron beam," Optical and Quantum Electronics, vol. 51, no 1, art. no 29, 2019. **(Q-2)**

Papers in proceedings international conferences

A.7. D. O. Herasymova, "Diffraction Radiation Analysis of Finite Graphene-Covered Nanowire Grating Excited by Electron Beam," Proc. Europ. Microwave Conf. (EuMC-2023), Berlin, 2023, pp. 544-547.

A.8. D. O. Herasymova, "Near and Far Field Characteristics of Two in Line Graphene Coated Dielectric Nanowires Excited by Modulated Electron Beam," Proc. 2023 IEEE/MTT-S International Microwave Symposium - IMS 2023, San Diego, CA, USA, 2023, pp. 482-485.

A.9. D. O. Herasymova, " Infrared diffraction radiation from two in-line dielectric rods covered with graphene," Proc. European Conf. Antennas and Propagation (EuCAP-2023), Florence, 2023, pp. 1-4.

A.10. D. O. Herasymova and S.V. Dukhopelnykov, " Lasing threshold conditions for transversal modes of twin graphene-covered circular quantum wires," Proc. European Microwave Conf. (EuMC-2022), Milan, 2022, pp. 242-245.

A.11. D. O. Herasymova, " Infrared Diffraction Radiation from Twin Dielectric Rods with Graphene Coatings as a Tool for Beam Position Sensing," Proc. Int. Conf. on Electronics and Nanotechnologies (ELNANO-2022), Kyiv, 2022, pp. 164-67.

A.12. D. O. Herasymova, " Electromagnetic analysis of lasing eigenmodes of twin semiconductor nanorods with graphene covers," Proc. European Conf. Antennas and Propagation (EuCAP-2022), Madrid, 2022, art. no 1570770733.

A.13. D. O. Herasymova, "Sensing the Charged-Particle Beam Position Using the Terahertz Range Diffraction Radiation from Two Dielectric Rods Covered with Graphene," Proc. European Microwave Conf. (EuMC-2021), London, 2021, pp. 249-253.

A.14. D.O. Herasymova, S.V. Dukhopelnykov, T.L. Zinenko, "Electromagnetic eigenvalue problem for twin dielectric rods covered with graphene: symmetry classes of the H-polarized supermodes," Proc. IEEE Ukraine Conf. Electrical and Computer Eng. (UKRCON-2021), Lviv, 2021, pp. 771-774.

A.15. D. O. Herasymova, " Evaluation of twin silver nanotubes as a possible sensor of the charged particle beam position," Proc. Europ. Microwave Conf. (EuMC-2020), Utrecht, 2020, pp. 615-618.

A.16. D. O. Herasymova, "Near fields of twin circular silver nanotubes exited by electron beam moving between them", Proc. IEEE Ukrainian Microwave Week (UkrMW-2020), IEEE 6th Microwaves, Radar and Remote Sensing Symposium (MRRS), Kharkiv, 2020, pp. 937-941.

A.17. D. O. Herasymova and S. V. Dukhopelnykov, "Full-wave modeling of beam position monitors on silver nanowires and nanotubes: analysis of solution convergence," Proc. Int. Conf. on Electronics and Nanotechnologies (ELNANO-2020), Kyiv, 2020, pp. 77-80.

A.18. D. O. Herasymova, "Electromagnetic design of beam position monitor based on diffraction radiation from twin dielectric nanowires," Proc. European Conf. Antennas and Propagation (EuCAP-2020), Copenhagen, 2020, art. no 9135642.

A.19. D. O. Yevtushenko, "Bright and dark supermodes of twin dielectric nanowire photonic molecule excited by a modulated electron beam," Proc. Int. Conf. Microwaves, Communications, Antennas, and Electronic Systems (COMCAS-2019), Tel Aviv, 2019, art. no 8958106.

A.20. D. O. Yevtushenko, "Optical range diffraction radiation of electron beam in the presence of twin circular dielectric nanowires," Proc. European Microwave Conf. (EuMC-2019), Paris, 2019, pp. 97-100.

A.21. D. O. Yevtushenko, "Optical resonances of photonic molecule of twin high refractive index dielectric nanowires excited by modulated electron beam," Proc. IEEE Ukraine Conf. Electrical Computer Eng. (UKRCON-2019), Lviv, 2019, pp. 771-774.

A.22. D. O. Yevtushenko and S. V. Dukhopelnykov, "Total scattering cross-section of twin circular silver nanowires excited by electron beam moving between them," Proc. European Microwave Conf. in Central Europe (EuMCE-2019), Prague, 2019, pp. 386-389.

A.23. D. O. Yevtushenko and S. V. Dukhopelnykov, "Near fields of twin circular silver

nanowires excited by electron beam moving between them," Proc. Int. Conf. on Electronics and Nanotechnologies (ELNANO-2019), Kyiv, 2019, pp. 340-343.

A.24. D. O. Yevtushenko, "Optical diffraction radiation of a beam of particles flowing near a circular silver nanowire," Proc. Int. Seminar/Workshop Direct and Inverse Problems of Electromagnetic and Acoustic Wave Theory (DIPED-2018), Tbilisi, 2018, pp. 43-46.

A.25. D. O. Yevtushenko, S. V. Dukhopelnykov, E. N. Odarenko, and A. I. Nosich, “Diffraction radiation of electron beam in the presence of dielectric optical nanowire resonator,” Proc. Int. Conf. Mathem. Methods in Electromagnetic Theory (MMET-2018), Kyiv, 2018, pp. 148-151.

Note: Dariia’s maiden name is Dariia Yevtushenko, therefore, in the articles published in 2018-2020, she is marked as D. O. Yevtushenko.